Superconducting Microwave Filters

by

Sormeh Setoodeh

A thesis

presented to the University of Waterloo

in fulfillment of the

thesis requirement for the degree of

Master of Applied Science

in

Electrical and Computer Engineering

Waterloo, Ontario, Canada, 2011

© Sormeh Setoodeh 2011

AUTHOR'S DECLARATION

I hereby declare that I am the sole author of this thesis. This is a true copy of the thesis, including any required final revisions, as accepted by my examiners.

I understand that my thesis may be made electronically available to the public.

Abstract

Superconducting microelectronics (SME) technology has the potential of realizing very high speed digital receivers capable of performing direct digitization of radio frequency signals with very low power consumption. The SME receiver is implemented on a single chip using Niobium based low temperature superconductive (LTS) Josephson Junction (JJ) technology by HYPRES. Analogue RF filters are still required at the receiver front end and are key components of the overall superconductor digital receiver. SME receivers usually require two types of RF filters; a wideband bandpass filter and a bandstop filter (a notch filter). The notch filter is required to eliminate interference and unwanted signals in the passband. In this thesis, design of highly miniaturized lumped element wideband and bandstop filters is investigated and some challenges are addressed. The filters are fabricated by the HYPRES process and therefore can be integrated with the SME receiver on the same chip.

In a wideband filter, the coupling between the adjacent resonators is high. Achieving such a strong coupling is one of the challenges of designing wideband filters. The wideband filters realized with distributed elements usually suffer from very low spurious frequency. As the bandwidth of the filter becomes wider, the spurious peak of the second harmonic gets closer to the passband of the filter. In the first part of this work, the possibility of realizing lumped element superconducting bandpass filters (BPF) with a relative bandwidth of 80% is investigated.

In the second part of the thesis, design and realization of lumped element superconducting bandstop filters (BSF) is discussed. The challenge for designing a bandstop filter is providing a good match over a wide frequency range. So narrowband inverters cannot be used. Instead,

usually λ/4 matched transmission lines provide 90° phase shift between the resonators of a notch filter. The possibility of replacing the long transmission line with other means or eliminating the inverters and using both shunt and series resonators are investigated. Having both series and shunt resonators introduces some new challenges that are addressed in the thesis and discussed thoroughly.

A tunable notch resonator is presented. The tunability is provided by a superconducting MEMS varactor that is realized in our group by doing some post processing on the device fabricated by HYPRES. The tunability range of the device at cryogenic temperatures is investigated. A 3-pole tunable BSF is also designed that uses the same tunable resonators. The tunability of the filter is investigated through simulation.

Acknowledgements

I would like to take the opportunity to express my sincere appreciation to Professor Raafat R. Mansour for accepting to be my supervisor and giving me the chance to be involved in his research group. His guidance, encouragement, support and attention from the beginning to the end made this research an enjoyable journey and it is my honor to be his student.

Many thanks to my colleagues and the CIRFE group members for their invaluable support and help during these years. Special thanks to our lab manager, Bill Jolley, for taking care of the hardest assemblies I needed for my measurements.

I am deeply indebted to Paul Laforge for his valuable insights and guidance throughout my research. I am also grateful to my dear friend and colleague, Sara Sharifian, who was there for me whenever I needed help and made our joint project a pleasant experience.

Last but not least, I owe a world of thanks to my husband, Nader Safavian, for his continuous support and encouragements during these years. I would like to dedicate this work to him and my parents to show my appreciation for their unconditional love and sacrifice.

Table of Contents

AUTHOR'S DECLARATION ii
Abstract iii
Acknowledgements v
Table of Contents vi
List of Figures viii
List of Tables xii
CHAPTER 1 1
1 Introduction 1
1.1 Motivation 1
1.2 Objective 3
1.3 Thesis Outline 4
CHAPTER 2 5
2 Literature Survey 5
2.1 Superconductivity at high frequencies 5
2.2 Superconducting lumped element filter design 9
CHAPTER 3 15
3 Highly Miniaturized Lumped Element Ultra-Wideband Band-pass Filter 15
3.1 HYPRES fabrication process 17
3.2 Lumped element filter design theory 18
3.3 Realization of the lumped element wideband BPF 24
3.3.1 Ness Method 25
3.3.2 Proposed method for wideband filter design 29
3.3.3 Measurement Setup 35
3.4 Further Miniaturization 35
CHAPTER 4 41
4 Band-stop Filter Design 41
4.1 Introduction 41
4.2 Lumped element BSF with alternating series and shunt resonators 42

4.3 Proposed Design Method 45
4.4 Design of a lumped element BSF using the proposed method 52
4.5 Design and realization of a 3-pole BSF with both shunt and series resonators 56
4.5.1 Investigation of discrepancy between simulated and measured result 59
4.5.2 BSF at 1GHz with 10% bandwidth 63
4.6 BSF with lumped all shunt resonators 68
4.7 Tunability of superconducting lumped element band-stop filters 72
4.8 All-pass filters 78
CHAPTER 5 81
5 Conclusion 81
Appendix A 84
References 90

List of Figures

Figure 1.1 Block diagram of a digital-RF transceiver [21] 2
Figure 1.2 Integration of the analog filter in the receiver front-end with the SME chip 3
Figure 2.1 Circuit model for the current flow in superconductors 6
Figure 2.2 Surface resistance of superconductors and normal metal versus frequency [3] 9
Figure 2.3 Layout for the 10GHz HTS band-pass filter [6] 11
Figure 2.4 Measured results of the superconducting lumped element filter reported in [6], (a) narrowband and (b) wideband frequency range 11
Figure 2.5 Measured results of an HTS lumped element 6-pole BPF [7] 12
Figure 2.6 Layout of the resonators used for the 7-pole HTS band-pass filter [8] 12
Figure 2.7 Final layout of the 7-pole HTS band-pass filter [8] 13
Figure 2.8 Simulation and measurement results for the 7-pole BPF [8] 13
Figure 2.9 (a)The 3D model of the niobium-based lumped element 3-pole filter, (b)Measured results for the 3-pole BPF [2] 14
Figure 3.1 Cross section of the HYPRES process 17
Figure 3.2 Ladder type circuit for the normalized low-pass filter prototype 20
Figure 3.3 The lumped element circuit model for the 7-pole BPF 24
Figure 3.4 Circuit simulation for the 7-pole BPF 24
Figure 3.5 Group delays of the first n cascaded resonators of a 7-pole BPF with a 1% BW [23] 28
Figure 3.6 (a) Layout of the first tuned resonator, (b) Correct group delay curve for the first resonator 30
Figure 3.7 (a) Layout of the first two tuned resonators, (b) Correct group delay curve for the first two resonators 31
Figure 3.8 (a) Layout of the first three tuned resonators, (b) Correct group delay curve for the first three resonators 31
Figure 3.9 (a) Layout of the first four tuned resonators, (b) Correct group delay curve for the first four resonators 32
Figure 3.10 A picture of the fabricated 7-pole BPF 33
Figure 3.11 EM simulation of the 7-pole BPF filter after tuning 33

Figure 3.12 Comparison between the return loss of the 7-pole filter derived from circuit and EM simulations 33
Figure 3.13 Comparison between the insertion loss of the 7-pole filter derived from circuit and EM simulations 34
Figure 3.14 Measured results of the fabricated 7-pole filter 34
Figure 3.15 A picture of the housing used for measurement purposes 35
Figure 3.16 Layouts of different configurations for spiral inductors 37
Figure 3.17 Inductances of different spiral inductors shown in Figure 3.15 derived from EM simulation 38
Figure 3.18 The 3D model of the highly miniaturized 3-pole low-pass filter 39
Figure 3.19 EM Simulation results of the LPF 39
Figure 3.20 EM simulation results of the LPF in the wide frequency range 40
Figure 3.21 Measured results of the LPF 40
Figure 4.1 Circuit models for lumped element band-stop filters, (a) series-shunt-series and (b) shunt-series-shunt topology 43
Figure 4.2 Circuit models for conventional and proposed series band-stop resonator 45
Figure 4.3 Circuit models for conventional and proposed shunt band-stop resonator 47
Figure 4.4 The circuit model for the proposed 3-pole BSF (series-shunt-series) 48
Figure 4.5 Comparison between the circuit simulation results of the conventional and proposed 3-pole band-stop filters with a 1% bandwidth for different values of ‘a’ 49
Figure 4.6 circuit simulation of the BSF designed with the proposed method when a=500 50
Figure 4.7 Low-pass behaviour of the proposed filter at high frequencies, a=500 50
Figure 4.8 Circuit simulation for a BSF designed with the proposed method but a bandwidth of 10% for different values of 'a' 51
Figure 4.9 Proposed lumped element circuit model for a 3-pole BSF (shunt-series-shunt) 52
Figure 4.10 3D models for the first and second resonator of the BSF at 2GHz with a 1% BW .. 54
Figure 4.11 Group delay and S-parameter response of each resonator for the BSF with a 1% BW 54
Figure 4.12 3D model for the 3-pole BSF at 2GHz with a 1% BW 55
Figure 4.13 EM simulation results for the 3-pole BSF at 2GHz with a 1% BW 55
Figure 4.14 EM simulation results in wide frequency range 55

Figure 4.15 The circuit model chosen to design the BSF at 2GHz with a 5% BW 56
Figure 4.16 layouts of the first and second resonators of the BSF with a 5% BW..... 57
Figure 4.17 Layout of the 3-pole BSF at 2GHz with a 5% BW 57
Figure 4.18 EM Simulation results for the BSF with a 5% BW..... 57
Figure 4.19 Measurement results for the BSF with a 5% BW..... 58
Figure 4.20 The mesh generated by Sonnet on the ground plane of a microstrip TL with one layer dielectric..... 60
Figure 4.21 The mesh generated by Sonnet on the ground plane of a microstrip TL with multi-layer dielectric..... 60
Figure 4.22 Simulation results of the 3-pole BSF with smaller cell size..... 61
Figure 4.23 3D model of the BSF at 1GHz with a 10% BW..... 64
Figure 4.24 EM simulation results of the BSF with a 10% BW..... 64
Figure 4.25 Measurement results of the BSF with a 10% BW..... 65
Figure 4.26 A comparison between simulation and measurement results of the BSF with a 10% BW by including the kinetic inductance of the Nb..... 65
Figure 4.27 Layout of the BSF at 1GHz with a 10% BW (shunt-series-shunt)..... 67
Figure 4.28 EM simulation results for the BSF with a 10% BW 67
Figure 4.29 Measurement results of the BSF with a 10% BW (shunt-series-shunt) 67
Figure 4.30 Schematic of a 3-pole BSF with lumped resonators and 90° transmission lines 68
Figure 4.31 Equivalent circuits at the resonance frequency of the resonators..... 69
Figure 4.32 Layout of the 90° TL with defected ground plane 69
Figure 4.33 Comparison of the S-parameters and electrical lengths of transmission lines with and without defected grounds..... 70
Figure 4.34 Layout of the 3-pole BSF with lumped resonators and 90° microstrip TLs 71
Figure 4.35 EM Simulation results of the 3-pole BSF with 90° TLs 71
Figure 4.36 Measurement results of the 3-pole BSF with 90° TLs 71
Figure 4.37 Measured results of the BSF with all shunt resonators in wide frequency range..... 72
Figure 4.38 3D model of an RF MEMS varactor realized with HYPRES process [20]..... 73
Figure 4.39 SEM picture of tunable resonator 1 [20] 74
Figure 4.40 Measurement results of the tunable resonator 1 [20] 74
Figure 4.41 SEM picture of tunable resonator 2..... 75

Figure 4.42 Measurement results of the tunable resonator 2 75
Figure 4.43 picture of the 3-pole tunable BSF 76
Figure 4.44 Simulated results of the tunable filter. 77
Figure 4.45 Simulated return loss of the tunable BSF 77
Figure 4.46 Circuit model of the all-pass filters with phase of (a) 90° and (b) -90° at the centre frequency 78
Figure 4.47 Layout of an all-pass filter at 2GHz 79
Figure 4.48 EM simulation results of an all-pass filter at 2GHz 79
Figure 4.49 Phase response of an all-pass filter at 2GHz 80
Figure 4.50 Comparison between phase response of the all-pass filter and a 90° transmission line 80
Figure A. 1 A simple shunt resonator 84
Figure A. 2 The group delay of shunt LC resonator showing the peak and centre frequencies. . 86
Figure A. 3 Comparison between the S-parameters and group delay curves of narrowband and wideband shunt resonators. 87
Figure A. 4 Comparison between the S-parameters and group delay curves of shunt resonators with percentage bandwidths of 1%, 5%, 10%, 20%, 50% and 100% respectively. 89

List of Tables

Table 2.1 Comparison between the characteristics of superconductors and good conductors 8
Table 3.1 Conversions from the normalized low-pass prototype to low-pass, highpass, band-pass and band-stop filters 22
Table 3.2 Component values for the 7-pole lumped element BPF 23
Table 3.3 Formulas for calculating the group delay value of the first n cascaded resonators of a filter at its centre frequency [9] 26
Table 4.1 Comparison between the component values of two BSFs with 5% and 1% bandwidths 44
Table 4.2 Component values for a BSF at 2GHz with a 1% BW 52

CHAPTER 1

1 Introduction

1.1 Motivation

Rapid Single-Flux-Quantum (RSFQ) logic is a superconductor IC technology which is based on the quantum effects in superconductors. In RSFQ circuits, information bits are represented by the presence or absence of quantized magnetic flux (fluxons) rather than voltage levels in conventional CMOS digital circuits. The Josephson junctions are the basic components of this technology, the same way that transistors are for semiconductor technology.

Superconductor Microelectronics (SME) technology provides the opportunity of realizing RSFQ circuits such as ultra-fast analog to digital converters and processors. Such functioning speeds cannot be achieved by semiconductor or any other room-temperature technologies. Using SME technology, the data can be processed digitally at RF frequencies. Nonlinear frequency-specific

analog components, such as analog mixers and channelizers, are replaced with software reconfigurable digital counterparts. Figure 1.1 shows the block diagram of a digital-RF transceiver.

HYPRES [1] Superconducting MicroElectronics (SME) Technology provides great performance improvements in the digital domain. This allows for the first time the direct digital conversion of RF signals, while enabling the use of advanced ultra-high speed digital signal processing techniques.

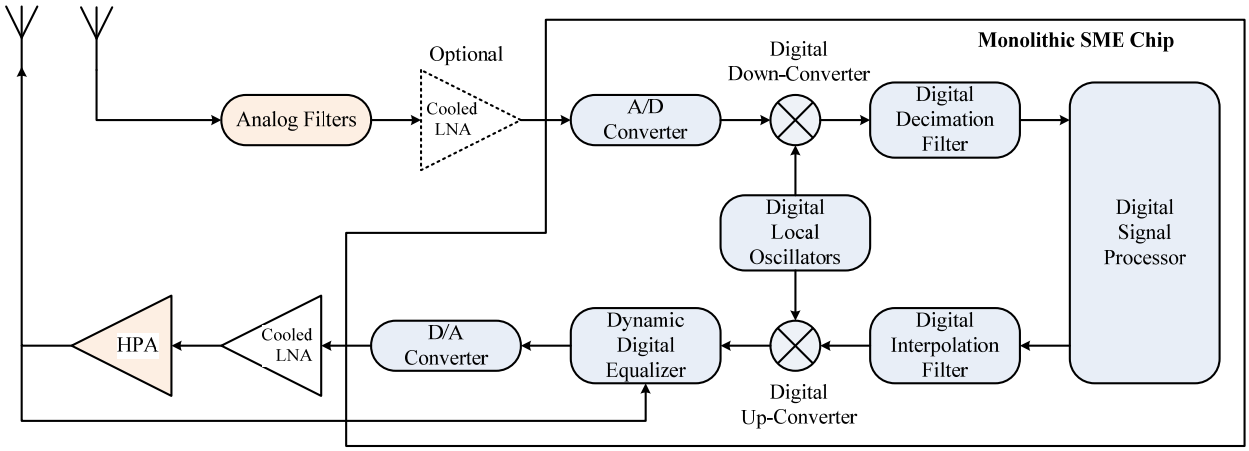

Figure 1.1 Block diagram of a digital-RF transceiver [21]

The analog filter shown in the block diagram is a key component to the front-end receiver and it should have minimal thermal noise. The superconducting metal layers and very thin dielectric layers provided by the HYPRES fabrication process allows for the design of highly miniaturized low noise lumped element superconducting filters. These can be integrated with the RSFQ circuits on the same chip as shown in Figure 1.2 [2]. Digital-RF receivers usually require two types of RF filters, a wideband band-pass filter and a band-stop filter to eliminate strong interferences.

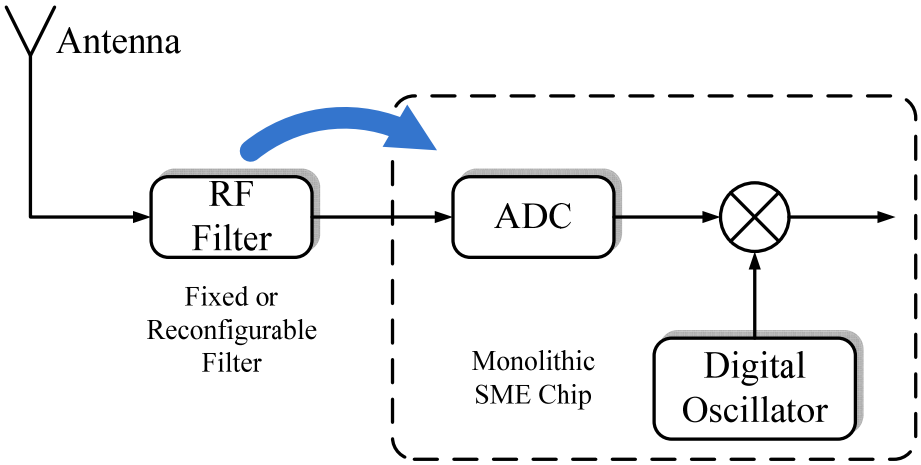

Figure 1.2 Integration of the analog filter in the receiver front-end with the SME chip

1.2 Objective

The purpose of this research is to investigate the possibility of realizing superconducting highly miniaturized wideband Band-Pass Filters (BPF) and Band-Stop Filters (BSF) to be integrated with the digital-RF receiver. The design of ultra-wideband band-pass filters using distributed elements is very challenging because a very strong coupling between the resonators is needed, which may not be realizable because of limitations in fabrication. Even if the physical realization is taken care of, the device is very sensitive to fabrication tolerances. On the other hand, the multi-layer niobium-based fabrication process offered by HYPRES allows for the design of miniaturized lumped element filters. So a lumped element approach is selected in this research for the design of the ultra-wideband BPF.

The challenge for designing a BSF is that a broadly matched pass-band is required which cannot be achieved if impedance or admittance inverters with narrowband approximations are used. Instead, 50Ω transmission lines are usually used to provide a 90° phase shift between the resonators. A 90° matched transmission line transfers a signal at all frequencies, however it

increases the filter size, especially at lower frequencies. Having access to superconducting multi-layer lumped element components, some new techniques can be used to realize miniaturized band-stop filters that provide a good transmission in their pass band without the need for 90° transmission lines.

1.3 Thesis Outline

Following the Introduction chapter, some background information and previous work on superconducting microwave filters (HTS and LTS) are presented in chapter 2.

In chapter 3, the possibility of designing lumped element ultra-wideband filters using a multi-layer superconducting fabrication process is investigated, and some miniaturization techniques is be discussed. The HYPRES fabrication process is introduced and step by step design of a wideband 7-pole band-pass filter to be realized by this process is presented. The measured results of the fabricated band-pass filter and a highly miniaturized low-pass filter are demonstrated in this chapter.

The focus of chapter 4 is mostly on lumped element band-stop filters. Some novel design methods are proposed and used to realize highly miniaturized band-stop filters that provide a good match from DC to high frequencies. The design method and the measured results of the band-stop filters are also demonstrated. In the last section of this chapter, the design and measurement results of the tunable notch resonators are presented. The tunability of the resonators is achieved by replacing the capacitor of the notch resonator with a superconducting Nb-based MEMS varactor designed by our group. A tunable 3-pole band-stop filter based on the measured results of the tunable resonators is designed and simulated.

Chapter 5 concludes this research.

CHAPTER 2

2 Literature Survey

2.1 Superconductivity at high frequencies

In normal metals, current is carried by electrons, while in superconductors the current carriers are a combination of normal electrons and electron pairs (Cooper pairs). The Cooper pairs travel without loss.

The ratio between the number of normal electrons (n_n) and cooper pairs (n_s) varies by temperature. At the transition temperature (T_c) of the superconductor (and higher temperatures) there are no Cooper pairs in the superconductor, but their number increases as temperature goes below T_c.

Equation (2.1) is a common expression used for calculating the number of normal electrons (n_n) and electron pairs (n_s) in the superconductor [3].

$$n_s = n_0(1 - t^4)$$
$$n_n = n_0 t^4 \tag{2.1}$$

Here n_0 is the total number of carriers in the material and $t = \frac{T}{T_c}$ where T is the actual temperature and T_c is the critical temperature of the superconductor.

This phenomenon is well known in superconductors and has been studied extensively. It has been shown that the existence of both normal electrons and Cooper pairs in the superconductors can be modeled by a complex conductivity as shown in equation (2.2).

$$J = J_s + J_n = (\sigma_1 - j\sigma_2)E \tag{2.2}$$

The circuit model that can describe this behavior is a resistor in parallel with an inductor as shown in Figure 2.1.

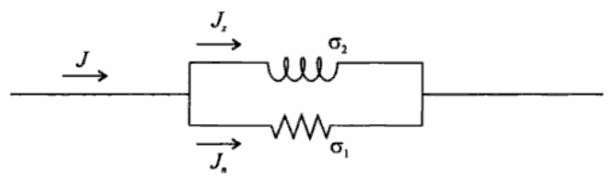

Figure 2.1 Circuit model for the current flow in superconductors

At DC the inductor will short out the resistor in the circuit model, so the superconductor is completely lossless. At low frequencies, the effect of the resistor is negligible; nonetheless, at high frequencies the high reactance of the inductor forces part of the current to flow through the resistor; therefore, the superconductor becomes lossy at very high frequencies.

The propagation constant and surface impedance of a material for a plane wave are calculated by equations (2.3) and (2.4) respectively.

$$\gamma = \sqrt{j\omega\mu(\sigma + j\omega\varepsilon)} \tag{2.3}$$

$$Z_s = \sqrt{\frac{j\omega\mu}{\sigma + j\omega\varepsilon}} \tag{2.4}$$

Substituting σ in the above equations by the complex conductivity($\sigma_1 - j\sigma_2$), the propagation constant and surface impedance is calculated by:

$$\gamma = \sqrt{\omega\mu\sigma_2}\left(1 + j\frac{\sigma_1}{2\sigma_2}\right) = \alpha + j\beta \tag{2.5}$$

$$Z_s = \sqrt{\frac{\omega\mu}{\sigma_2}}\left(\frac{\sigma_1}{2\sigma_2} + j\right) = R_s + jX_s \tag{2.6}$$

Two assumptions are made for deriving the above formulas. First, it is assumed that $\frac{\omega\varepsilon}{\sigma_2}$ is very small which is true because of the very high conductivity. The second assumption, is that the superconductor is well below its critical temperature; thus, $\sigma_2 \gg \sigma_1$.

The real part of the propagation constant, α, represents the decay of the electromagnetic wave as it travels in a superconductor. The depth where the wave decays by $e^{\alpha z}=e^{-1}$ is called the penetration depth for the superconductor and can be calculated by equation (2.7).

$$\lambda = \frac{1}{\sqrt{\omega\mu\sigma_2}} \tag{2.7}$$

An interesting fact about superconductors is that $\sigma_2 \alpha \frac{1}{\omega}$; therefore, λ is independent of the frequency. For a normal conductor on the other hand, σ_n is independent of frequency; hence, the skin depth is inversely proportional to the square root of the frequency.

Substituting equation (2.7) into (2.6), R_s and X_s are obtained by:

$$R_s = \frac{\omega^2 \mu^2 \sigma_1 \lambda^3}{2} \tag{2.8}$$

$$X_s = \omega \mu \lambda \tag{2.9}$$

Now the value of the inductor L_s in the circuit model can be calculated from the reactance derived in equation (2.9). L_s is called the kinetic inductance of the superconducting material.

$$L_s = \mu \lambda \tag{2.10}$$

Table 2.1 compares the parameters of a good conductor with a good superconductor. For a good conductor it is assumed that $\frac{\omega \varepsilon}{\sigma_2}$ is very small.

Table 2.1 Comparison between the characteristics of superconductors and good conductors

Parameter	Superconductor	Good conductor
Conductivity	$\alpha = \sqrt{\omega \mu \sigma_2}$	$\alpha_{normal} = \sqrt{\frac{\omega \mu \sigma_n}{2}}$
Penetration depth / Skin depth	$\lambda = \frac{1}{\sqrt{\omega \mu \sigma_2}}$	$\delta_{normal} = \sqrt{\frac{2}{\omega \mu \sigma_n}}$
Propagation velocity	$c = \sqrt{\frac{4\omega\sigma_2}{\mu\sigma_1^2}} = \frac{2}{\lambda \mu \sigma_1}$	$c_{normal} = \sqrt{\frac{2\omega}{\mu \sigma_n}}$
Surface resistance	$R_s = \frac{\omega^2 \mu^2 \sigma_1 \lambda^3}{2}$	$R_{s\,normal} = \sqrt{\frac{\omega \mu}{2\sigma_n}}$
Surface reactance	$X_s = \sqrt{\frac{\omega \mu}{\sigma_2}}$	$X_{s\,normal} = \sqrt{\frac{\omega \mu}{2\sigma_n}}$

Table 2.1 shows that the surface resistance of a superconductor is proportional to the frequency squared. However, for a good conductor, surface resistance is proportional to square root of the frequency. So the surface resistance of superconductors increases much faster in frequency compare to normal conductors. This means that at really high frequencies (usually several hundred GHz) the superconductor can produce more loss than normal metals. Figure 2.2 compares the variation of surface resistance versus frequency for superconductors and copper for normal conductors.

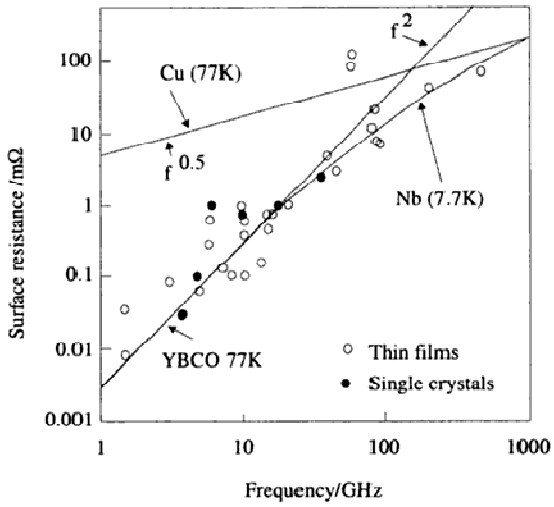

Figure 2.2 Surface resistance of superconductors and normal metal versus frequency [3]

2.2 Superconducting lumped element filter design

Microwave filters can benefit from superconductors in a number of ways. The most obvious advantage of superconductors is their significantly lower surface resistance compared to conventional metals used for microwave devices such as gold or copper. Therefore, by replacing the metal in a filter with a superconducting material, the insertion loss reduces significantly and as a result the quality factor of the filter (Q) improves accordingly. However, this does not

exploit the full potential of superconductivity. Miniaturizing microwave devices realized in normal conductors would degrade their performance. Superconductors on the other hand provide the possibility of miniaturizing filters, filter banks, diplexers and other microwave devices while maintaining a high performance. Some of these superconductor device designing techniques are listed in the following [4]:

1. Use of high dielectric constant substrates.
2. Use of internal inductance.
3. Meandering or coiling the transmission lines.
4. Use of slow wave transmission lines.
5. Use of lumped element components

Since the focus of this research is on lumped element designs, a summary of the previous works on this subject will be discussed in this section.

The downside of using superconductors is that there has to be a cryogenic system that cools down the device to liquid nitrogen temperature (77K) if high temperature superconductors (HTS) are used and liquid helium temperatures (4K) for low temperature superconductors (LTS). Such systems have been built with very good performances, however the complexity and reliability of these systems have limited the applications of superconductors.

Although there are many papers on High Temperature Superconducting (HTS) distributed filters in the literature, there are few published works on HTS lumped element filters, mainly because of some limitations in fabricating via holes and air bridges on HTS films. There are reported though a few via-less lumped element filters with very interesting designs and good measured results.

For example, a ninth order Chebyshev filter with a bandwidth of 800 MHz (and a pass band between 1.1 and 1.9 GHz) with great selectivity was designed and measured [5]. The size of the filter is 6mm by 15mm and the measured return loss is better than 17dB within the pass band. A waveguide filter that can provide the same performance will be more than three feet in length. In another work, a narrowband lumped element band-pass filter was designed at 10GHz with a percentage bandwidth of 3%. The measured results show a broad spurious free stop band between 1GHz to 21GHz [6]. In this filter, spiral inductors had been used with gold crossover contacts. The average Q of the filter was decreased to about 330 because of the use of gold. Figures 2.3 and 2.4 shows the layout and measured results of this filter, respectively. The size of the filter is 2.54mm by 7.62mm.

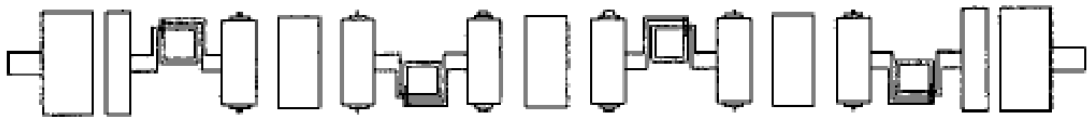

Figure 2.3 Layout for the 10GHz HTS band-pass filter [6]

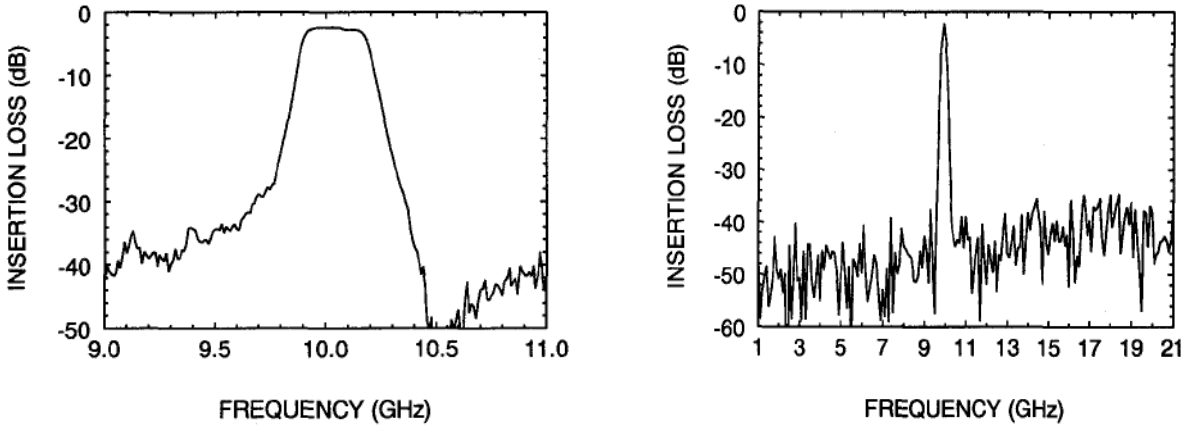

(a) (b)

Figure 2.4 Measured results of the superconducting lumped element filter reported in [6], (a) narrowband and (b) wideband frequency range

A 6-pole lumped element band-pass filter with 2% bandwidth is another example of a via-less HTS design reported in the literature [7]. The measured results for the 6-pole filter are shown in Figure 2.5.

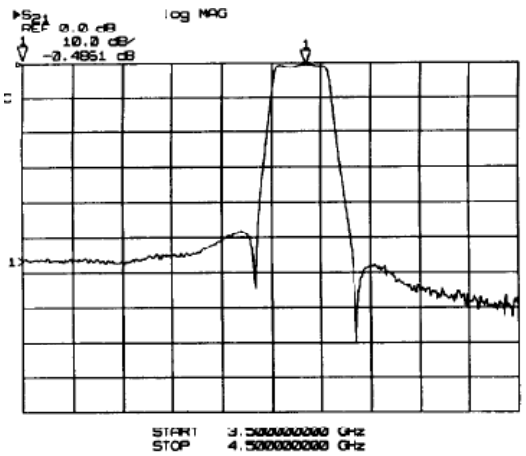

Figure 2.5 Measured results of an HTS lumped element 6-pole BPF [7]

A highly miniaturized 7-pole HTS band-pass filter at 610MHz with a bandwidth of less than 1% was also realized using interdigital capacitors and double-spiral inductors [8]. The resonator is shown in Figure 2.6. The final filter has a dimension of around 20mm by 5mm as shown in Figure 2.7 which is very compact for a 1-layer 7 pole filter at this frequency range. The simulated versus measured results for this filter are shown in Figure 2.8.

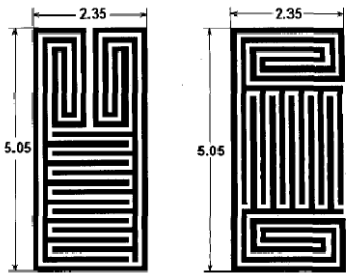

Figure 2.6 Layout of the resonators used for the 7-pole HTS band-pass filter [8]

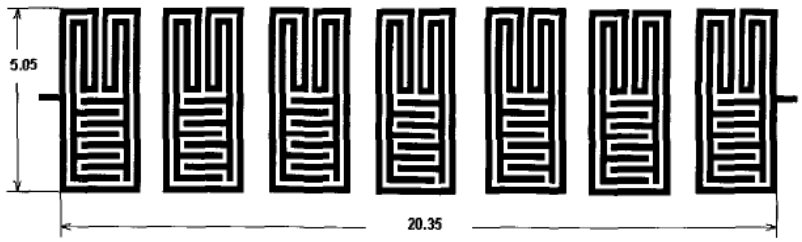

Figure 2.7 Final layout of the 7-pole HTS band-pass filter [8]

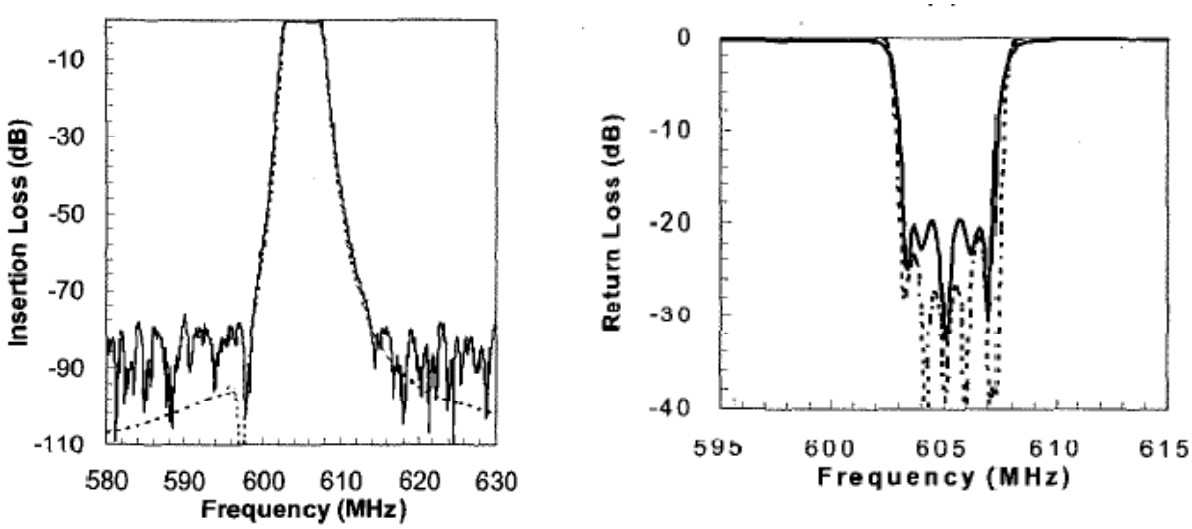

Figure 2.8 Simulation and measurement results for the 7-pole BPF [8]

All the lumped element resonators and filters mentioned so far were realized by HTS material and they were all limited to via-less single layer designs. Using niobium on the other hand which is a low temperature superconducting material, there is a commercial multi-layer fabrication process offered by the HYPRES foundry [1]. The most important benefit of this process for passive microwave devices is that it allows the fabrication of superconducting lumped element parallel plate capacitors and spiral inductors.

The first lumped element filter realized with the HYPRES process was a 3-pole band-pass filter at 1.28GHz with less than a 10% bandwidth [2]. The 3D model of the filter is shown in Figure 2.9(a). The dimension of the filter is only 2mm by 0.6mm which is extremely miniaturized

compared to the HTS filters. Parallel plate capacitors with really thin dielectric layers in this process could be realized. The measured result of this filter is shown in Figure 2.9(b).

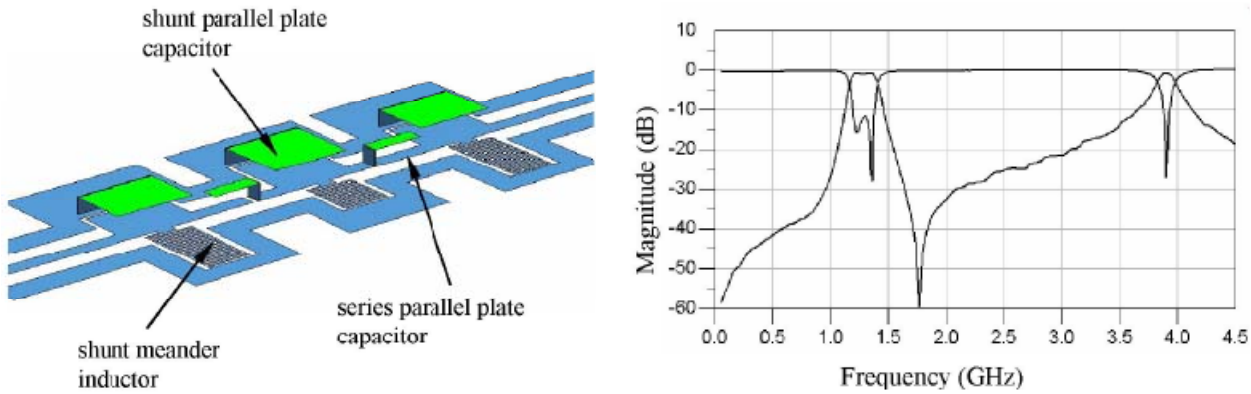

(a) (b)

Figure 2.9 (a)The 3D model of the niobium-based lumped element 3-pole filter, (b)Measured results for the 3-pole BPF [2]

CHAPTER 3

3 Highly Miniaturized Lumped Element Ultra-Wideband Band-pass Filter

The conventional distributed filter designs in general are practical for relative bandwidths of up to 20% or less. In a wideband filter, the couplings required the adjacent resonators are high. Achieving such a strong coupling is challenging for a number of reasons. For example, one way to increase the coupling is to decrease the gap between the resonators; however, there is a limit on how small the gap can be in terms of physical realization. Also, any small variation in the gap caused by fabrication tolerances can affect the performance of the device severely. The other problem with distributed wideband filter designs is in their low spurious frequency performance. As the bandwidth of the filter becomes wider, the spurious peak of the second harmonic gets closer to the pass band of the filter.

In theory, a wideband filter can be easily realized with ideal lumped element inductors and capacitors in a ladder type circuit with no limit on the bandwidth. There are no spurious peaks for this filter configuration, and the coupling between the resonators can be determined by changing the ratio between the value of the inductor and capacitor in each resonator. Although conventional lumped elements usually cannot be used in microwave devices because of the associated loss, superconducting lumped elements demonstrate great potential for high frequency microwave devices.

In this chapter, the possibility of realizing a superconducting ultra-wideband band pass filter using lumped elements is investigated. The effectiveness of the proposed method in addressing the aforementioned challenges has been verified through measurement.

All the devices that will be discussed in this chapter and chapter 4 are designed to be fabricated by the HYPRES process. The really thin dielectric layers and the possibility of using vias in this multi-layer superconducting process gives the designer the opportunity to create extremely miniaturized microwave devices compared to the HTS devices discussed in chapter 2.

The method used for the design and tuning of the filters was originally proposed by Ness [9], with some modifications that make it practical for wideband filters as well. A coarse model (Agilent ADS circuit simulator [10]) and a fine model (Sonnet EM simulator [11]) are used in the design and tuning process.

In this chapter the HYPRES fabrication process is first explained. Then the basic lumped element filter design using ideal capacitors and inductors will be reviewed. The Ness method will be discussed followed by the modification that makes it applicable to wideband filters. Next, a step by step design and realization of a lumped element 7-pole band-pass filter with an 80%

bandwidth, along with its measurement results will be presented. At the end of this chapter a miniaturized design for the spiral inductors is introduced which is used in designing a highly miniaturized low-pass filter. The size of the 7-pole BPF can be reduced in half if its inductors are replaced with the proposed design.

3.1 HYPRES fabrication process

The HYPRES process [1] is used to fabricate superconducting integrated circuits including very high speed data converters (ADCs and DACs), phased lock loops and oscillators, memories, digital signal processing cores, sensors and detectors, SQUIDs (Superconductor Quantum Interference Devices) and SQUID amplifiers, SIS (Superconductor-Insulator-Superconductor) mixers and RSFQ (Rapid Single Flux Quantum) logic gates.

The process also offers many possibilities for the fabrication of microwave components. The HYPRES process, as shown in Figure 3.1, has ten levels consisting of thin niobium layers, resistive metal layers, insulating layers, and the niobium–aluminum oxide–niobium tri-layer.

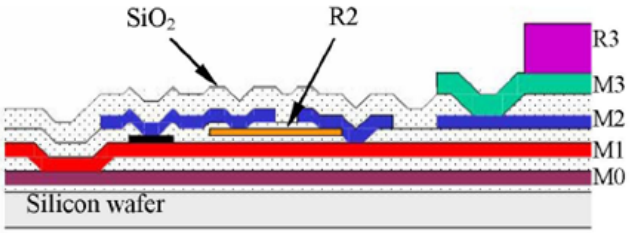

Figure 3.1 Cross section of the HYPRES process

The M0 is the first deposited superconducting metal layer (Niobium with a thickness of 100 nm) on the top of the silicon substrate. An insulating layer of silicon dioxide with a thickness of 150nm is deposited on top of the M0. The M1 niobium layer is deposited next, at a thickness of

135 nm. An insulating layer of silicon dioxide, a resistive layer (R2), and another insulating layer are then deposited. The two insulating layers both have a thickness of 100 nm, and the resistive layer is comprised of a thin layer of either molybdenum or Ti–AuPd–Ti. Another 300-nm-thick niobium layer (M2), a 500-nm-thick SiO_2 insulating layer, a 600-nm-thick niobium layer (M3), and a contact layer (R3) are the last four layers deposited during the fabrication process.

3.2 Lumped element filter design theory

Among different filter design methods, the insertion loss method is the most popular one, because it provides a high degree of control over the pass band and stop band amplitude and phase characteristics, with a systematic way to synthesize a desired response [12]. In this method, the filter response is defined by its insertion loss or power loss ratio defined by equation (3.1).

$$P_{LR} = \frac{\text{Power available from source}}{\text{Power delivered to load}} = \frac{1}{1 - |\Gamma(\omega)|^2} \tag{3.1}$$

Where $\Gamma(\omega)$ is the reflection coefficient at the input port of the filter. It can be shown mathematically that $|\Gamma(\omega)|^2$ is an even function of ω. As a result it can be written in the form of equation (3.2).

$$|\Gamma(\omega)|^2 = \frac{M(\omega^2)}{M(\omega^2) + N(\omega^2)} \tag{3.2}$$

Substituting the above equation into equation (3.1), the expression for the power loss ratio of a physically realizable filter can be written in the form of equation (3.3).

$$P_{LR} = 1 + \frac{M(\omega^2)}{N(\omega^2)} \tag{3.3}$$

The power loss ratio expression for the maximally flat (Butterworth) and equal ripple (Chebyshev) types of filters is presented in equations (3.4) and (3.5), respectively.

$$P_{LR} = 1 + k^2 \left(\frac{\omega}{\omega_c}\right)^{2N} \tag{3.4}$$

$$P_{LR} = 1 + k^2 T_N^2 \left(\frac{\omega}{\omega_c}\right) \tag{3.5}$$

Where N is the order of the filter and ω_c is the cutoff frequency. $T_N(x)$ is the Nth order Chebyshev polynomial and is defined by equation (3.6).

$$\begin{gathered} T_1(x) = x \\ T_2(x) = 2x^2 - 1 \\ T_N(x) = 2xT_{N-1}(x) - T_{N-2}(x) \end{gathered} \tag{3.6}$$

The ladder circuits for the low-pass filter prototypes of order N are shown in Figure 3.2. It is possible to solve for the value of inductances and capacitances by equating the desired filter function to the P_{LR} of the ladder circuit. For the maximally flat and Chebyshev filter types however there are formulas that can be used to calculate the values of the components (g-values) directly. The g-values are derived for a normalized low-pass design where the source impedance is 1Ω and the cutoff frequency is ω_c=1. So impedance and frequency conversion should be done according to the filter specifications.

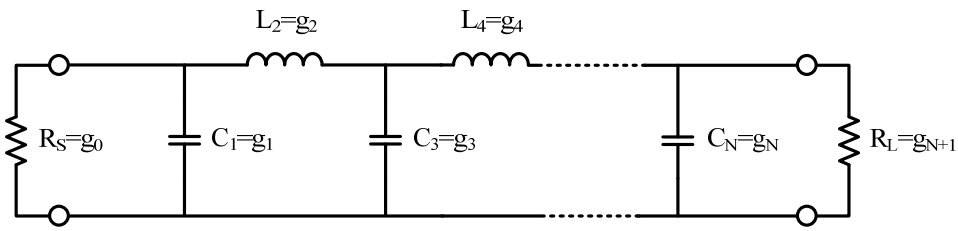

Figure 3.2 Ladder type circuit for the normalized low-pass filter prototype

The g-values for the normalized low-pass maximally flat and Chebyshev designs can be calculated using equations (3.7) and (3.8) respectively

For maximally flat filters:

$$g_0 = 1$$

$$g_k = 2\sin\left[\frac{(2k-1)\pi}{2n}\right], \qquad k = 1, 2, \ldots, n \tag{3.7}$$

$$g_{n+1} = 1$$

For Chebyshev filters with the specified Return Loss (RL):

$$g_0 = 1$$

$$\beta = \ln\left(\coth\left(\frac{L_{AR}}{17.37}\right)\right)$$

$$\gamma = \sinh\left[\frac{\beta}{2n}\right]$$

$$a_k = \sin\left[\frac{(2k-1)\pi}{2n}\right], \qquad k = 1, 2, \dots, n$$

$$b_k = \gamma^2 + \sin^2\left(\frac{k\pi}{n}\right), \qquad k = 1, 2, \dots, n \tag{3.8}$$

$$g_1 = \frac{2a_1}{\gamma}$$

$$g_k = \frac{4a_{k-1}a_k}{b_{k-1}g_{k-1}}, \qquad k = 2, 3, \dots, n$$

$$g_{n+1} = \begin{cases} 1 & n \text{ odd} \\ \coth^2\left(\frac{\beta}{4}\right) & n \text{ even} \end{cases}$$

Where n is the filter order and L_{AR} is the ripple level in the pass band in dB. The ripple level can be calculated in terms of the filter Return Loss (RL) by the following equation (3.9).

$$L_{AR} = -20\log\left(\sqrt{1 - 10^{\frac{-RL}{10}}}\right) \tag{3.9}$$

For example, a filter with a 25dB return loss, and has a ripple value of 0.0137dB.

The normalized low-pass design can be transformed into low-pass, high-pass, band-pass or band-stop filters at the desired cutoff or centre frequency. The proper characteristic impedance of the transformations are presented in table 3.1.

Δ is the percentage bandwidth of the filter $\left(\Delta = \frac{\omega_2 - \omega_1}{\omega_0} = \frac{BW}{\omega_0}\right)$ and Z_0 is the characteristic impedance of the network.

Table 3.1 Conversions from the normalized low-pass prototype to low-pass, highpass, band-pass and band-stop filters

Normalized Low-pass	Low-pass	High-pass	Band-pass	Band-stop
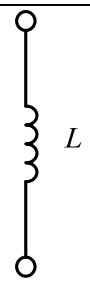	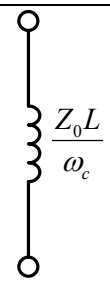	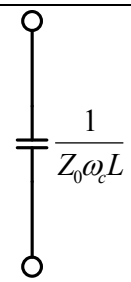	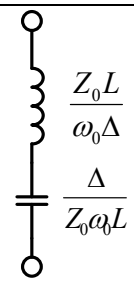	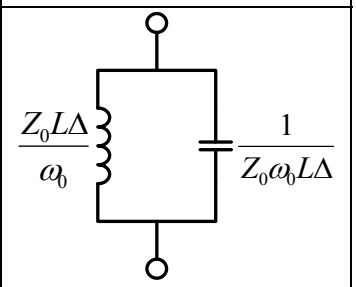
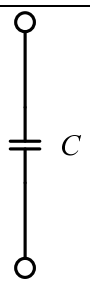	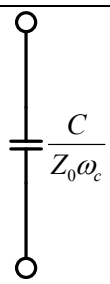	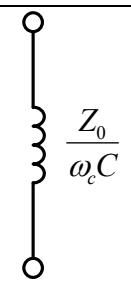	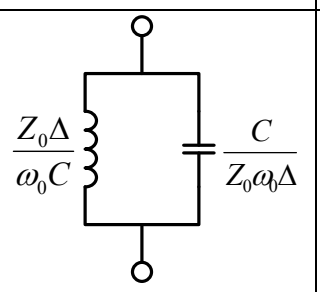	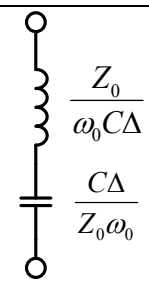

Theoretically at this point, the circuit model of the filter is complete, however in practice it is often inconvenient or even impossible most of the time to realize a filter with both shunt and series resonators depending of the structure of the filter (distributed filters, dielectric resonator filters, …). Therefore, usually the next step in the design is to convert all the resonators to the same kind using impedance or admittance inverters [12]. Although it is possible for lumped element filters to have both shunt and series resonators, it is really challenging to realize a

narrowband lumped element filter with both types of resonators, because of the wide spread component values. However, impedance and admittance inverters provide a good performance for narrowband applications (bandwidths less than 20%). On the other hand, as the bandwidth of the filter becomes wider, the component values in both series and shunt resonators lie in ranges that are more feasible for fabrication. Therefore lumped element configuration with alternating shunt and series resonators is a great candidate for realizing very wideband filters.

A 7-pole Chebyshev lumped element band-pass filter with a centre frequency of f_0=375MHz and 80% bandwidth (BW=300MHz) is designed with alternating shunt and series resonators. The filter is designed to have a 25dB return loss.

The calculated g-values for this filter are:

g_0=1 g_1=0.8358 g_2=1.4074 g_3=1.7843 g_4=1.6368 g_5=1.7843 g_6=1.4074 g_7=0.8358 g_8=1

By transforming the g-values to the band-pass LC prototype, the filter component values can be calculated. The calculated values for the inductors and capacitors of each resonator are listed in Table 3.2. It should be noted that in this design the first resonator is assumed to be a shunt.

Table 3.2 Component values for the 7-pole lumped element BPF

L(nH)	L_1=20.3121	L_2=37.3321	L_3=9.5146	L_4=43.4165	L_5=9.5146	L_6=37.3321	L_7=20.3121
C(pF)	C_1=8.8679	C_2=4.8250	C_3=18.9317	C_4=4.1488	C_5=18.9317	C_6=4.8250	C_7=8.8679

Figure 3.3 shows the final lumped element circuit model for a 7-pole band-pass filter. The circuit is simulated using the Agilent ADS circuit simulator. The simulation results are shown in Figure 3.4. The realization of this filter will be discussed later in this chapter.

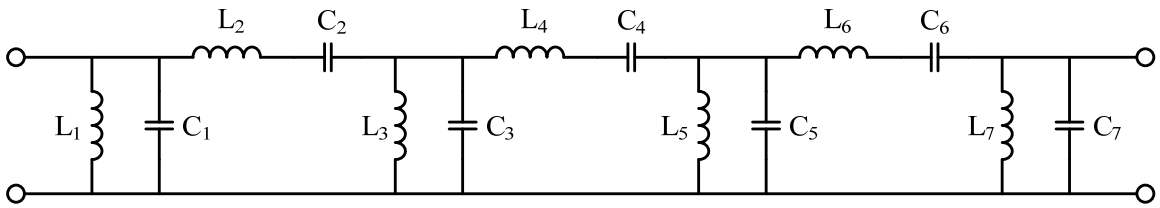

Figure 3.3 The lumped element circuit model for the 7-pole BPF

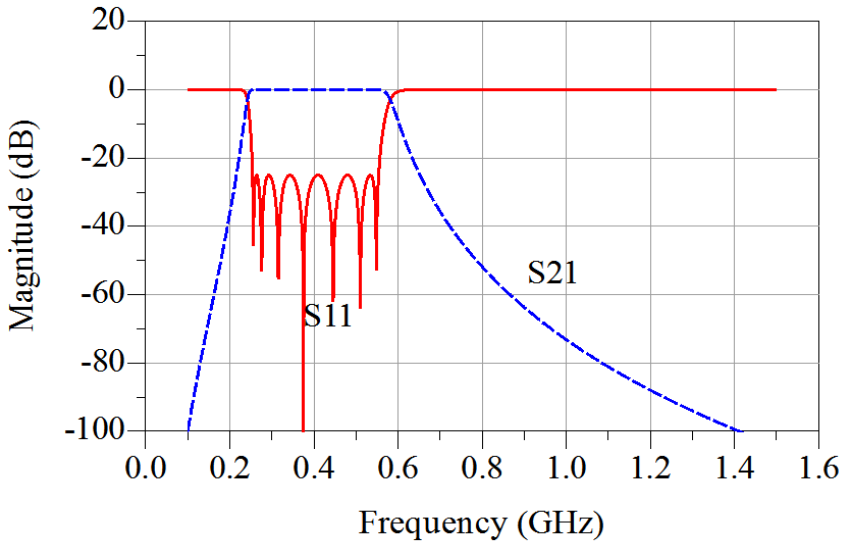

Figure 3.4 Circuit simulation for the 7-pole BPF

3.3 Realization of the lumped element wideband BPF

To realize the 7-pole band-pass filter, the capacitors and inductors can be designed simulated and tuned individually by an EM simulator until their values at the centre frequency of the filter are matched. These calculated values are listed in Table 3.2. If we connect these tuned components to form the shunt and series resonators and then simulate the whole filter, the simulation results will be quite different from the circuit simulation. This is expected since the connections between the components and other parasitic effects can shift the resonance frequency of all the resonators, therefore all the components have to be optimized. Considering the long EM

simulation time with too many variables to be tuned for a high order filter, optimization can take days if possible at all. So a new approach should be developed to design and tune the filter. There are many different EM-based advanced design techniques reported in the literature such as space mapping [13] and the Calibrated Coarse Model (CCM) [14] techniques, along with numerous other optimization techniques [15] that can be applied to accomplish accurate EM-based designs with a reasonable computation time.

The technique that is used here does not optimize all the parameters of the filter all at once. Instead it starts by tuning the first resonator by optimizing its parameters, then the next resonator is added and gets tuned and this process continues until the whole filter is tuned. The computation time reduces significantly in this method by lowering the number of parameters that require tuning at each stage of the design. The criterion for tuning each stage of the filter is the reflection group delay of the simulated design that should be matched to that of the circuit model. This method is a more generic version of the tuning technique which was first introduced by Ness [9].

3.3.1 Ness Method

Ness proposed a method for tuning microwave filters by monitoring the group delay of the input reflection coefficient at the input as the resonators get tuned sequentially [9]. This method can be used for the tuning of a manufactured filter or during the design process. The reflected Group Delay (GD) can be extracted from the phase information of the reflected signal.

$$GD = -\frac{\partial \varphi}{\partial \omega} \tag{3.10}$$

Where $\varphi = \angle(\mathrm{S11})$. For a given filter low-pass prototype's g-values, centre frequency and its bandwidth, Ness has derived formulas for calculating the group delay of the input reflection

coefficient for the first *n* tuned resonators at the centre frequency of the filter, in terms of the low-pass prototype g-values, centre frequency of the filter and its bandwidth. Meanwhile the rest of the resonators (resonators n+1, n+2, …,N) are detuned intentionally [9]. The derived formulas are listed in the Table 3.3.

Table 3.3 Formulas for calculating the group delay value of the first n cascaded resonators of a filter at its centre frequency [9]

n=1	$\Gamma_{d1}(\omega_0) = \frac{4g_0 g_1}{\omega_2 - \omega_1}$
n=2	$\Gamma_{d2}(\omega_0) = \frac{4g_2}{g_0(\omega_2 - \omega_1)}$
n=3	$\Gamma_{d3}(\omega_0) = \frac{4g_0(g_1 + g_3)}{(\omega_2 - \omega_1)}$
n=4	$\Gamma_{d4}(\omega_0) = \frac{4(g_2 + g_4)}{g_0(\omega_2 - \omega_1)}$
n=5	$\Gamma_{d5}(\omega_0) = \frac{4g_0(g_1 + g_3 + g_5)}{(\omega_2 - \omega_1)}$
n=6	$\Gamma_{d6}(\omega_0) = \frac{4(g_2 + g_4 + g_6)}{g_0(\omega_2 - \omega_1)}$

It is important to note that this method is useful only if the group delay curve of the tuned resonators is symmetric around the filter's centre frequency. It will be shown later in this chapter that as the bandwidth of the filter goes higher, the symmetry of the group delay curve fades away. This limits its application to narrowband filters.

To tune a manufactured narrowband filter using Ness method, all the filter's resonators should be detuned from their centre frequency first. The tuning process starts with the first resonator of the filter. The resonator is tuned when its reflected group delay is symmetric around the filter's

centre frequency and its value is equal to $\Gamma_{d1}(\omega_0)$. This can be done by changing the input coupling and the resonance frequency of the first resonator. The second resonator should be tuned next by changing its resonance frequency and the coupling between the first and second resonators. It should be noted that changing the coupling could affect the resonance frequency of the first resonator slightly. So to make the group delay symmetric with the correct value at the centre frequency ($\Gamma_{d2}(\omega_0)$) a slight tuning of the first resonator might be required. The tuning process for the rest of resonators is the same and at each stage the only parameters that need major tuning are the ones in the recently added resonator while minor tuning of the parameters may be necessary in the resonator just before it. Figure 3.5 shows the correct group delay curves for successively tuned resonators of a 7-pole band-pass filter with a centre frequency of 1GHz and a relative bandwidth of 1%.

The same tuning method can be applied to an EM-based filter design. In the design process, the method can be simplified because we are not dealing with a manufactured filter. For example, there is no need of detuning the resonators. Instead to design the nth shunt resonator, resonators n+1, …, N can simply be removed. A series resonator, on the other hand should be shorted to the ground to be tuned while the rest of the resonators are removed. Also since filter elements are designed in symmetry, we just need to perform the design up to the middle resonator and the rest will be the mirror image of the first half of the design.

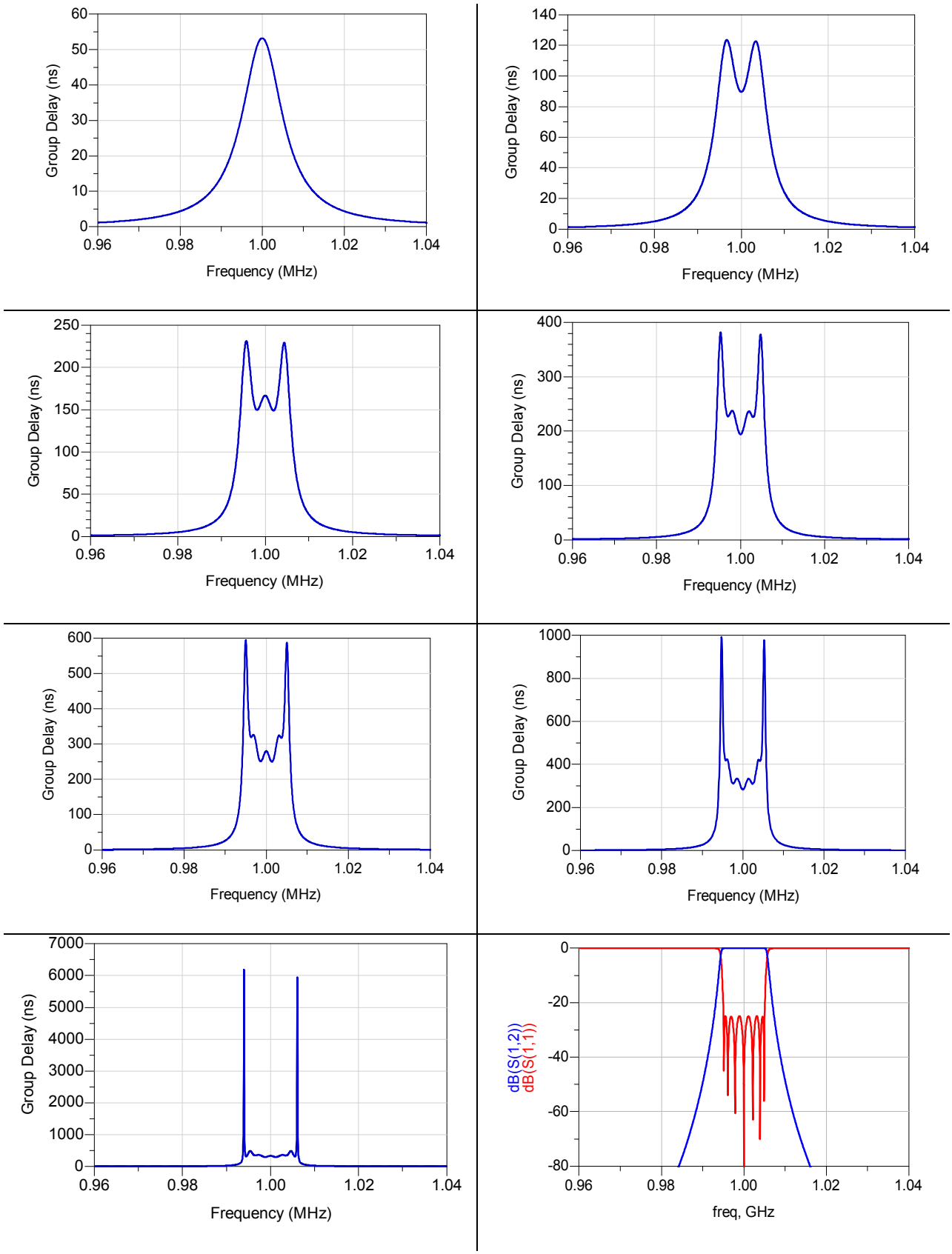

Figure 3.5 Group delays of the first n cascaded resonators of a 7-pole BPF with a 1% BW [23]

3.3.2 Proposed method for wideband filter design

As it was mentioned earlier, the group delay curve is not perfectly symmetric around the filter's centre frequency. This is shown mathematically for the group delay curve of the first tuned resonator in Appendix A. However, for filters with a percentage bandwidth of 1% or less the symmetry assumption can be safely used.

It will be shown in this section that filters with higher bandwidths can still be designed and tuned by matching the group delays of the resonators generated by the EM simulator and the circuit simulator. The only difference is that we do not try to make a symmetric group delay with the peak values calculated by Ness. Instead we match the group delay of the resonator to the one generated by the circuit simulator.

To show the validity of this method, the 7-pole lumped element band-pass filter with an 80% bandwidth is designed and tuned using this technique. The step by step tuning of the resonators is demonstrated here.

Design Steps:

The calculated values for the inductor and capacitor in the first resonator are 20.3121 nH and 8.8679 pF respectively. In the first step, a parallel plate capacitor and a spiral inductor is designed and tuned individually in an EM simulator so their values match the calculated values at the filter's centre frequency. Then the designed inductor and capacitor should be connected in parallel to form the first shunt resonator. Performing an EM simulation on the single port resonator would give a reflection from the resonator over the frequency (S11).

The ideal group delay generated by the Agilent ADS circuit simulator is plotted in Figure 3.6(b). It can be seen that although the resonance frequency of the filter is at 375MHz, the peak value of

the group delay for the first resonator is located at f=326MHz. The resonator elements in the layout need to be tuned until the group delay generated by the EM simulator matches the one from the circuit simulation. For a lumped element resonator, L×C defines its resonance frequency while changing the L/C (or C/L depending on the type of the resonator) ratio determines the peak value of the group delay curve.

The layout that provides the matched group delay is shown in Figure 3.6.

To tune the second resonator, again a capacitor and inductor should be designed and tuned separately so their values match the calculated values for C2 and L2. The designed L and C should then be connected in series and then shorted to the ground as shown in Figure 3.7(a). After running an EM simulation on the new layout, the group delay can be extracted. The group delay for the circuit model generated by ADS is also shown in Figure 3.7(b). Again the components in the second resonator need to be tuned so that the group delays generated by the EM and the circuit simulator match. To achieve the perfect match, it may be necessary to do small re-tuning on the first resonator as well.

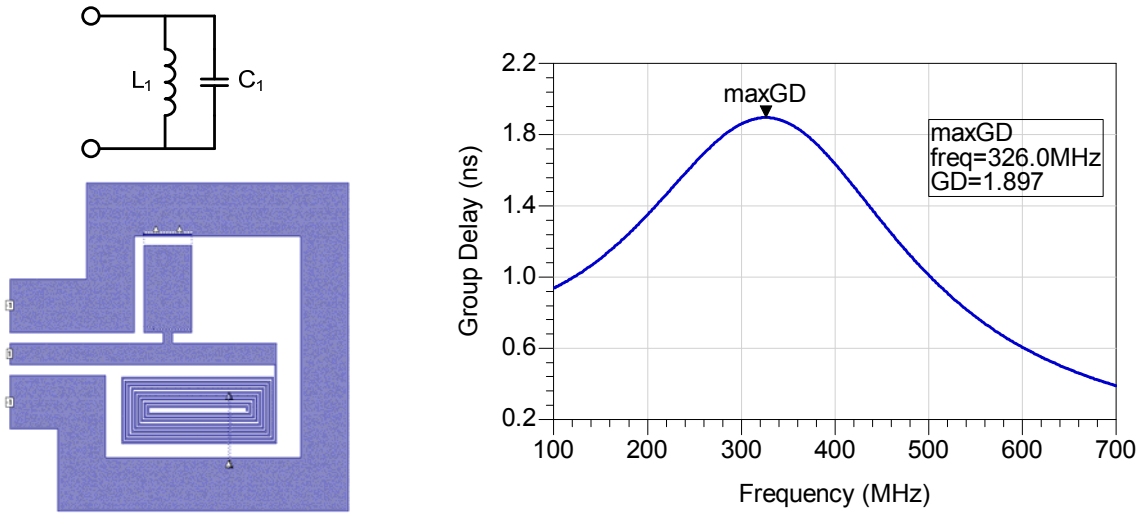

(a) (b)

Figure 3.6 (a) Layout of the first tuned resonator, (b) Correct group delay curve for the first resonator

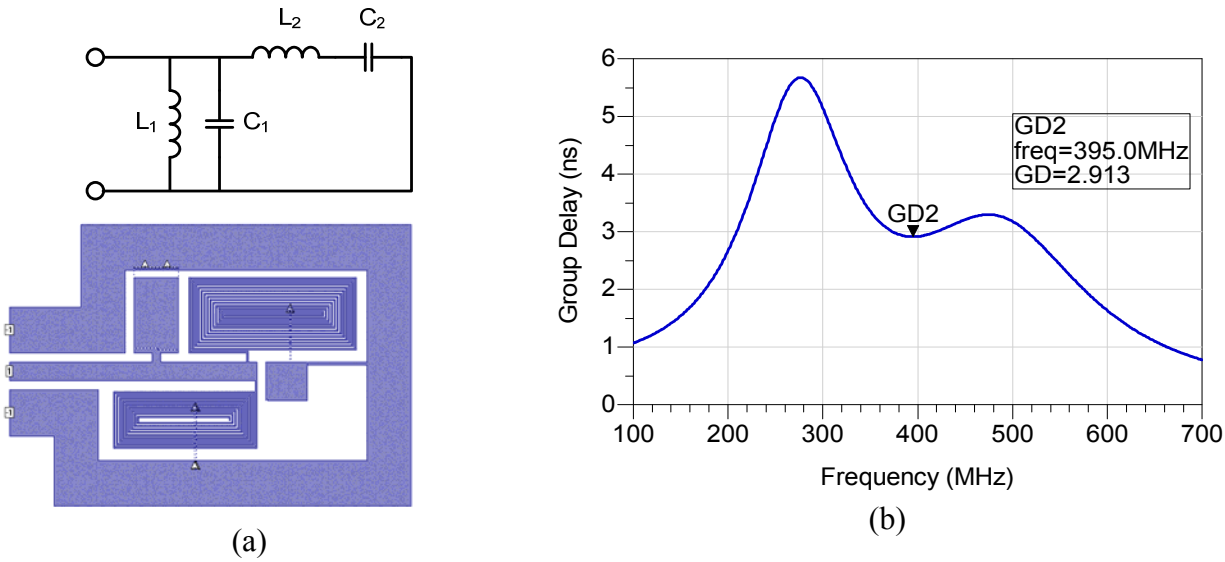

Figure 3.7 (a) Layout of the first two tuned resonators, (b) Correct group delay curve for the first two resonators

When the first two resonators get tuned, the third resonator can be added as shown in Figure 3.8. The ideal group delay curve is also shown in the same figure for the first three tuned resonators. By tuning L3 and C3 and maybe a small re-tuning of the first two resonators, the EM simulated group delay will match the ideal one really well.

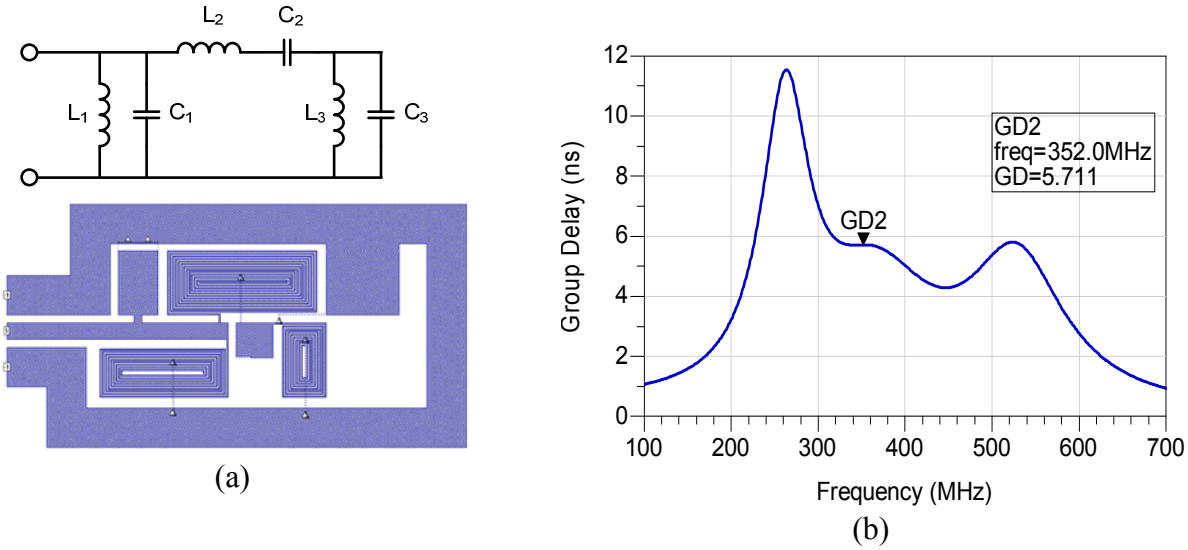

Figure 3.8 (a) Layout of the first three tuned resonators, (b) Correct group delay curve for the first three resonators

Resonator 4 is the last resonator that needs tuning, because the rest of the resonators are the mirror image of the first 3 resonators. L4 and C4 are designed first and they get connected in series. At one end of the series, the resonator will be attached to the tuned resonators and the other end will be shorted to ground. The components in the 4th resonator will be tuned until the EM simulated group delay matches the ideal one shown in Figure 3.9. Again minor re-tuning of the other resonators may be necessary.

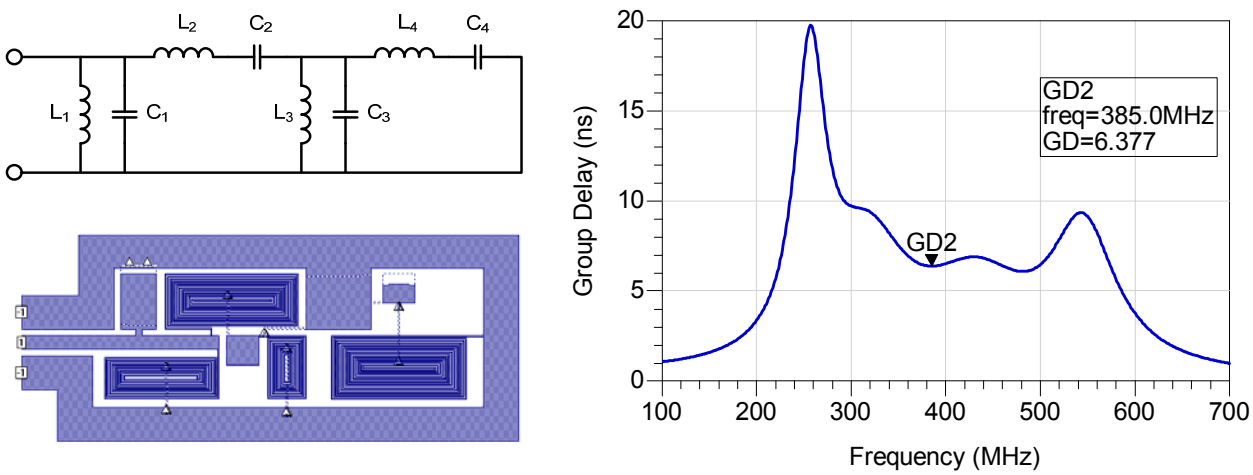

(a) (b)

Figure 3.9 (a) Layout of the first four tuned resonators, (b) Correct group delay curve for the first four resonators

After tuning the first 4 resonators, the layout of the whole filter can be constructed. The last 3 resonators are the mirror image of the first 3. At this point the two port filter can be simulated. The EM simulation should be close to the circuit simulation of the ideal filter. Some final tuning on the last tuned resonator (the middle resonator in the filter) may be done to improve the response even more. Figure 3.10 shows a picture of the fabricated device. The dimension of the filter is 3mm×0.9mm while the wavelength at the center frequency of the filter is 800mm. Figure 3.11 illustrates the EM simulation results. Figure 3.12 and 3.13 compare the return loss and insertion loss of the EM simulation and ideal circuit simulation of the 7-pole band-pass filter.

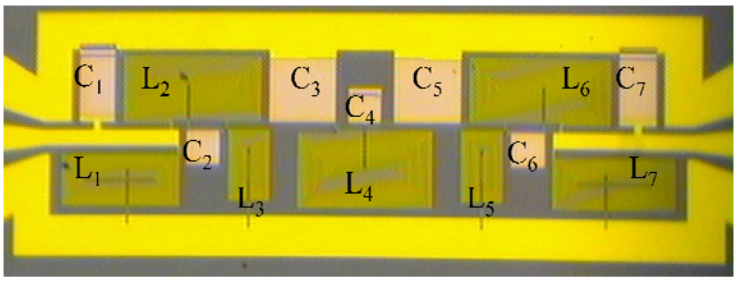

Figure 3.10 A picture of the fabricated 7-pole BPF

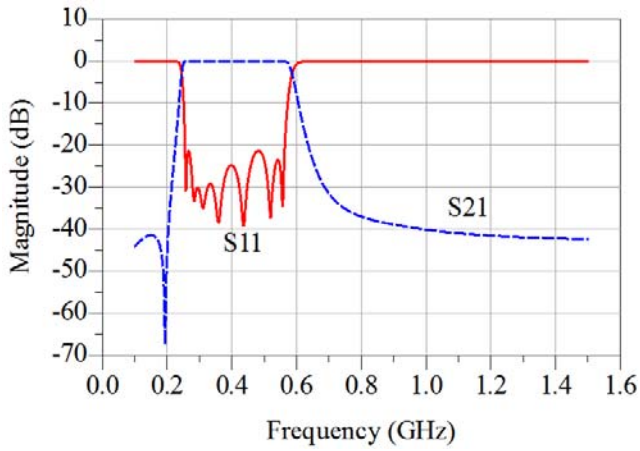

Figure 3.11 EM simulation of the 7-pole BPF filter after tuning

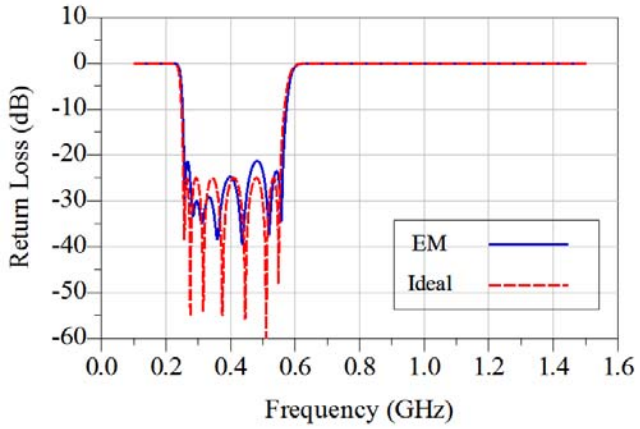

Figure 3.12 Comparison between the return loss of the 7-pole filter derived from circuit and EM simulations

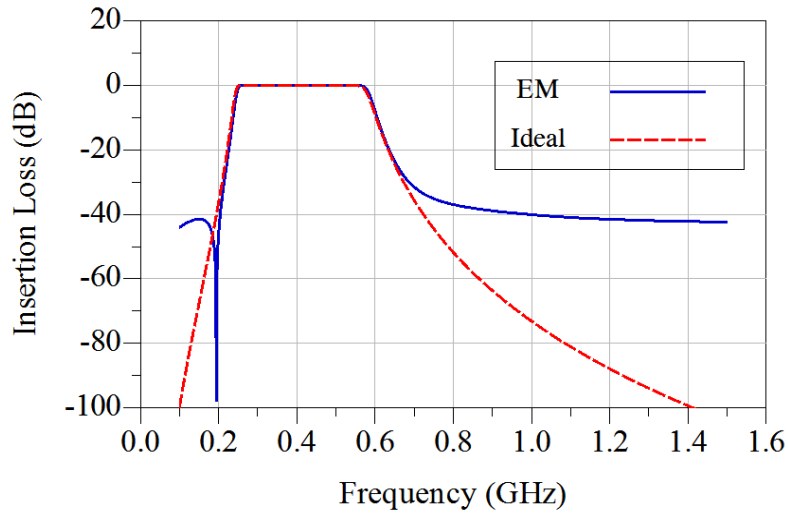

Figure 3.13 Comparison between the insertion loss of the 7-pole filter derived from circuit and EM simulations

This filter was fabricated by HYPRES and measured at the CIRFE lab at the University of Waterloo. The measurement result is shown in Figure 3.14.

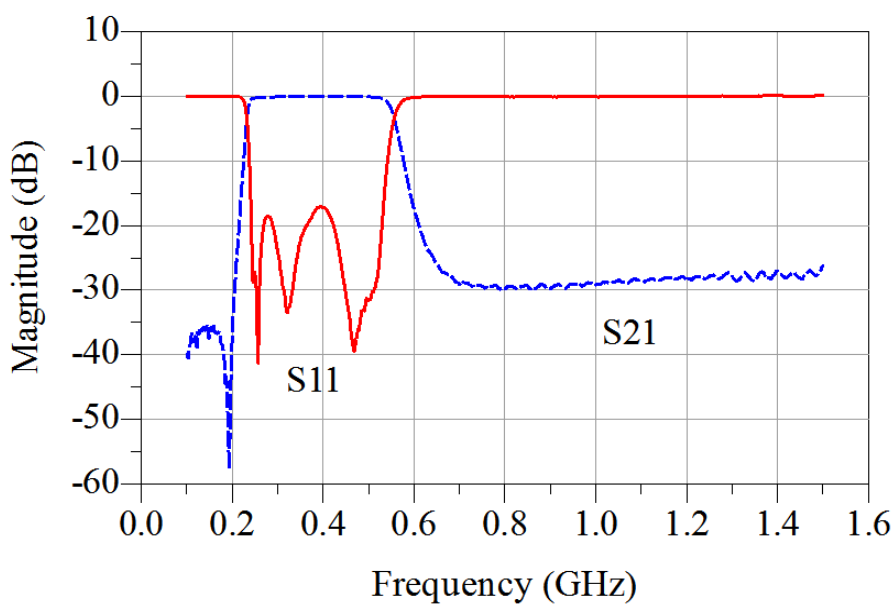

Figure 3.14 Measured results of the fabricated 7-pole filter

3.3.3 Measurement Setup

The device is also measured in a cryogenic environment. The two port network device is wire bonded to a gold coplanar waveguide (CPW) transmission line in a metal housing. The housing is then immersed in liquid helium. Semi-rigid coaxial cable is used to connect to the MEMS varactor through the housing and to a vector network analyzer (VNA). A picture of the housing used for the measurements in this work is shown in Figure 3.15.

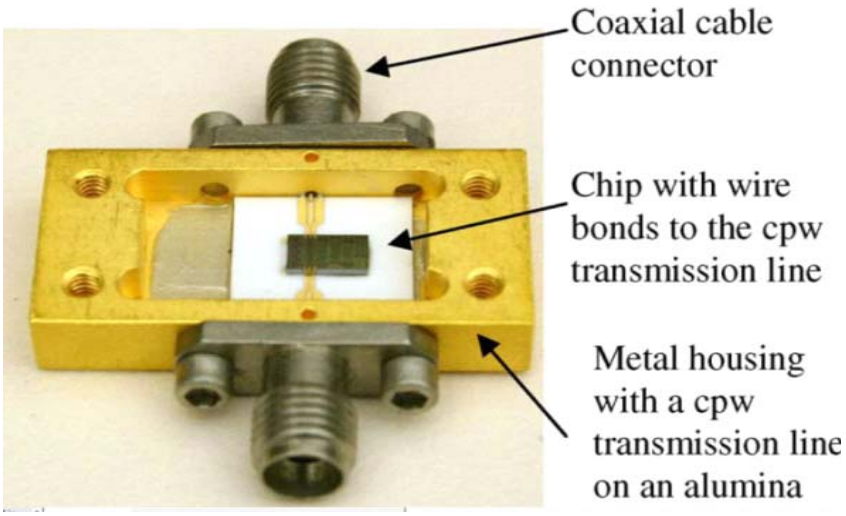

Figure 3.15 A picture of the housing used for measurement purposes.

3.4 Further Miniaturization

Although the size of the designed 7-pole filter is extremely small in comparison to the wavelength, there is still room for miniaturization specially by modifying the inductors' design.

Proposed in this work is the use of multi level spiral inductor instead of the one layer inductor. If N identical spiral inductors, each with an inductance value of L, are connected side by side in series as demonstrated in Figure 3.16(b), the total inductance adds up to N×L. However, if they are stacked on top of each other as shown in Figure 3.16(c), the total inductance will be

proportional to $N^2 \times L$. The rationale behind this phenomenon is that, similar to coils, the magnetic flux generated by each layer of inductor will pass through all the other layers. It is important to note that the direction of current flow in all the levels should be the same, otherwise the flux from two levels will cancel each other out to a great extent and the total inductance will be even less than L.

Figure 3.15 compares the inductance value and size of different combinations of spiral inductors. The inductance of each topology shown in Figure 3.17 is derived from the S-parameters using EM simulation.

The inductors shown in Figure 3.16 are designed to be compatible with the HYPRES process. The two metal layers used in these designs are M0 and M3, and the total oxide thickness between them is 0.85µm. Consequently, there is a parasitic capacitance between the spiral inductors in the 2-layer designs which causes the self resonance frequency of the inductor to shift to a lower frequency. However, if a thick oxide layer (more than 10µm) is available in a fabrication process, the self resonance frequency will shift to even higher frequencies than the 1-layer design in Figure 3.16(e) simply because of shorter length of wire in the 2-layer design.

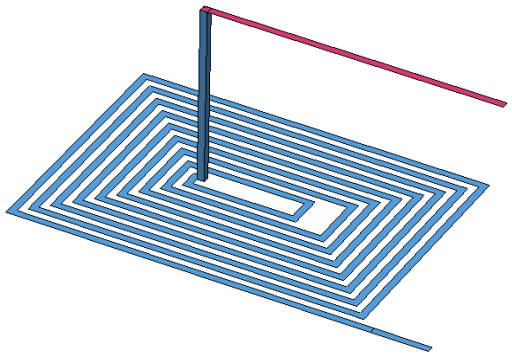

a. A Spiral inductor the of value 5.9nH and dimension of 153µm×105µm

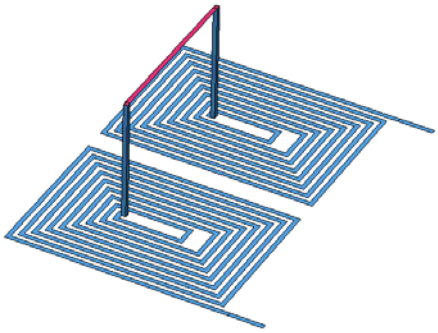

b. Two sets of spiral inductors shown in (a) in series side by side. Total inductance is 11.6nH. The dimension is 153µm×225µm.

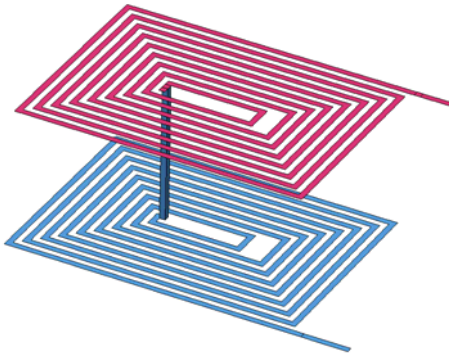

c. Two sets of spiral inductors shown in (a) stacked on top of each other. The direction of current on both inductors is counter clock wise. Total inductance is 22nH. The dimension is 153µm×105µm.

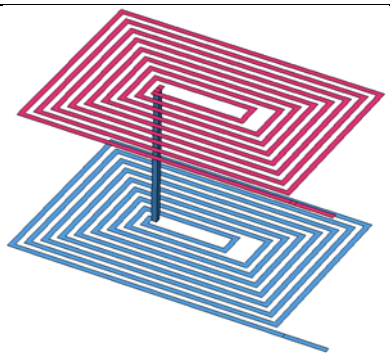

d. Two sets of spiral inductors shown in (a) stacked on top of each other. The direction of current on the top inductors is clock wise, but it is counter clock wise on the other one. Total inductance is 1.25nH. The dimension is 153µm×105µm.

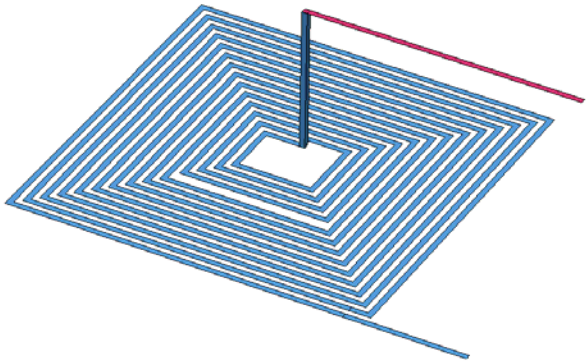

e. 1-layer spiral inductor that provides the same inductance as the 2-layer inductor in (c) which is (22nH).
The dimension of this inductor is 198µm×192µm. So the area of this inductor is almost 2.4 times bigger than the one in (c).

Figure 3.16 Layouts of different configurations for spiral inductors

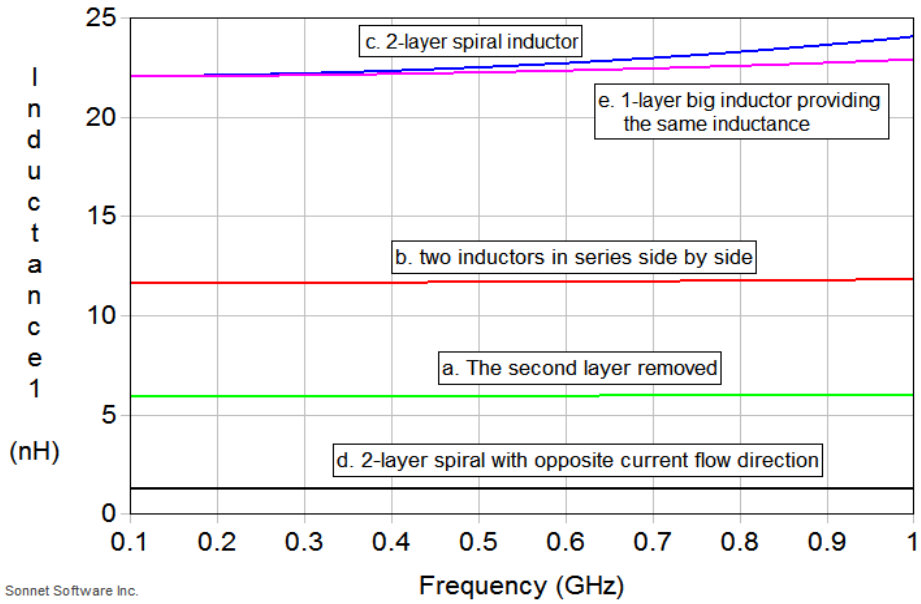

Figure 3.17 Inductances of different spiral inductors shown in Figure 3.15 derived from EM simulation

A 3-pole Chebyshev low-pass filter with a cut-off frequency of 300MHz and a return loss of 25dB is designed using this concept with a similar concept for capacitor miniaturization. Three different metal layers of M0, M1 and M2 are used to make miniaturized multilayer capacitors, The plates on the M0 and M2 layers are connected to each other with a via and are connected to the signal line of the CPW transmission line; while the plate on the M1 layer in the middle is connected to the ground of the CPW transmission line. The result is two capacitors in parallel. This kind of multilayer capacitor was also used in [16]. Moreover one of the ground planes of the CPW transmission line is removed, so the ports of the filter are not 50Ω. This is not a problem at low frequencies because the filter size is much smaller than the wavelength; at higher frequencies it even provides better rejection. The design is extremely miniaturized using all these techniques and has a dimension of 549μm×123μm.

The 3D model of the low-pass filter is shown in Figure 3.18. The simulated and measured results are demonstrated in Figure 3.19 and Figure 3.21 respectively. Figure 3.20 shows the simulation results over a wide frequency range. The filter exhibits a spurious free window of up to 4 GHz.

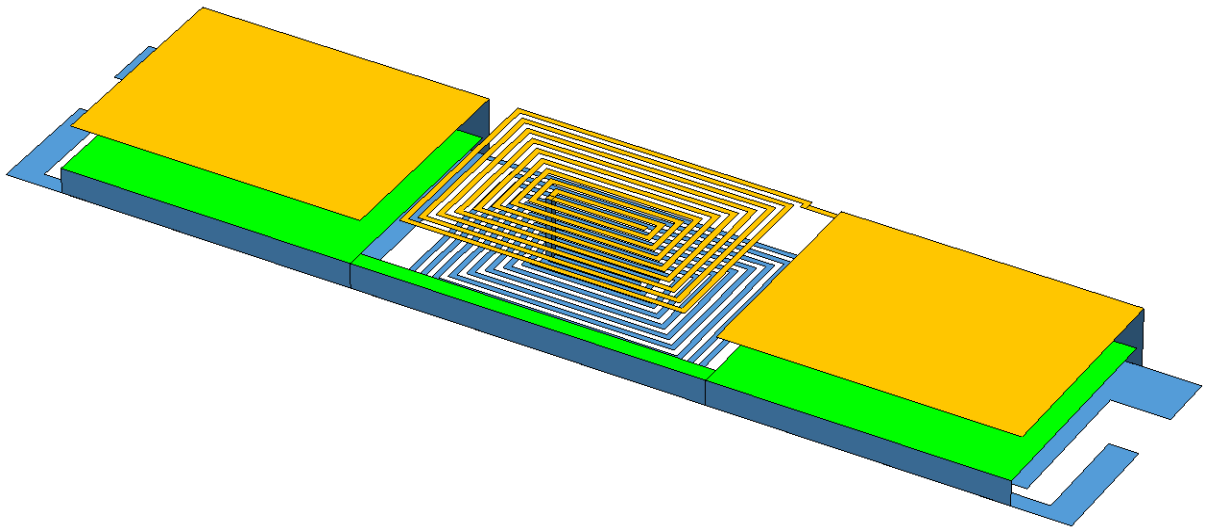

Figure 3.18 The 3D model of the highly miniaturized 3-pole low-pass filter

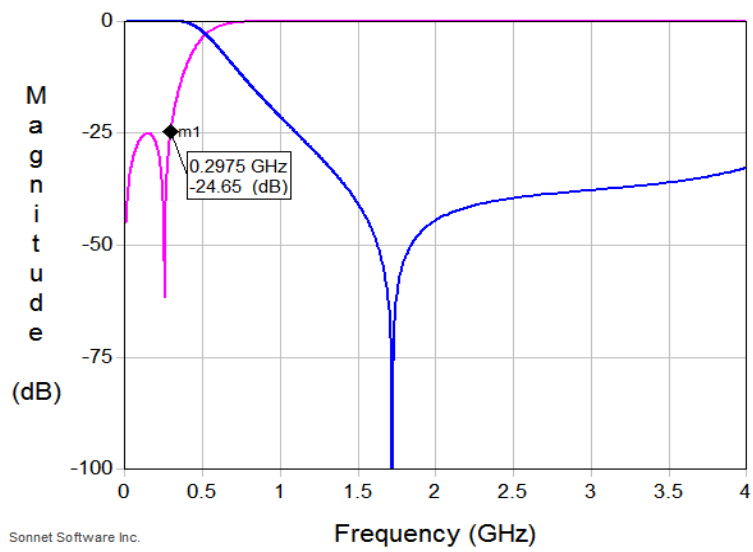

Figure 3.19 EM Simulation results of the LPF

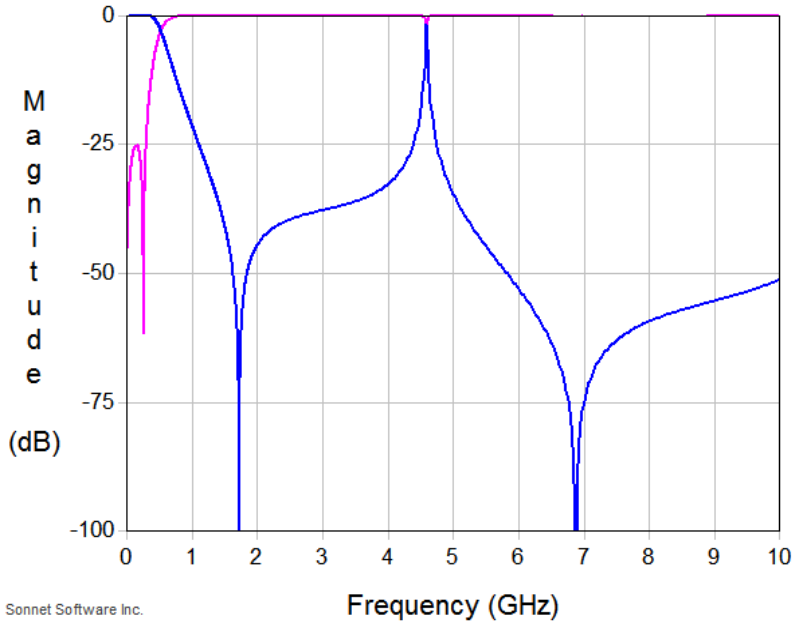

Figure 3.20 EM simulation results of the LPF in the wide frequency range

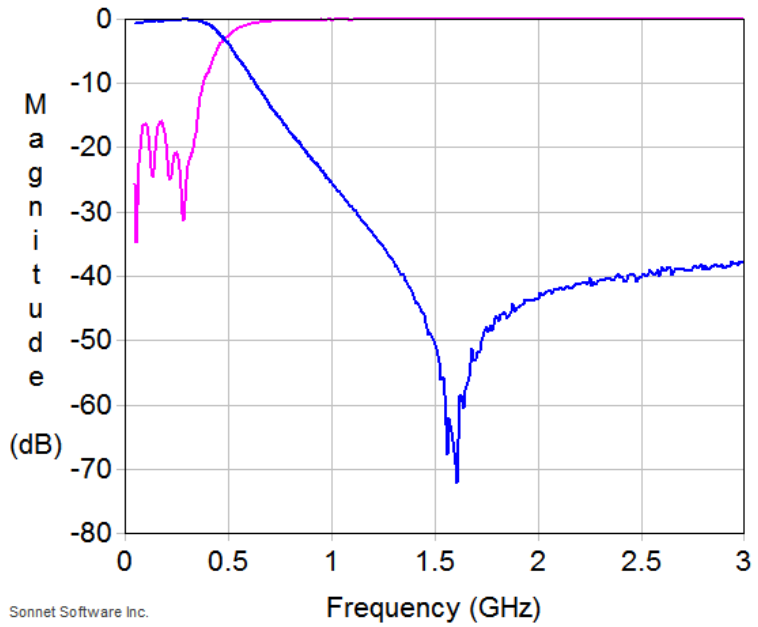

Figure 3.21 Measured results of the LPF

CHAPTER 4

4 Band-stop Filter Design

4.1 Introduction

Band-Stop Filters (BSF) are usually used to suppress interference and unwanted signals. The most important specification of a BSF is that it should suppress any signal in its stop-band while the rest of the frequencies are left without either attenuation or amplification. Therefore, a broadly matched pass band is required which cannot be achieved if impedance or admittance inverters with narrowband approximations are used. Instead, 50Ω transmission lines are usually used to provide a 90° phase shift between the resonators [17][18]. A 90° matched transmission line transfers the signal at all frequencies, however it increases the filter size especially at lower frequencies. Similar to the wideband lumped element BPF design discussed in chapter 3, the multilayer niobium-based superconducting fabrication process offered by HYPRES allows for the realization of highly miniaturized band-stop filters. Thus, the use of any kind of inverter can be eliminated which decreases the size of a multi-pole band-stop filter significantly while

maintaining a good match from DC to high frequencies. Althought, for narrowband lumped element band-stop filters, the wide spread of element values in each resonator can be problematic in terms of physical realization especially when both series and shunt resonators are being used.

In this chapter the challenges associated with designing lumped element band-stop filters is discussed in more detail and a solution to address this problem is presented. The proposed design method is then used to design a BSF with a 1% BW. The design, simulation and measurement results of a few fabricated band-stop filters are presented next. To achieve tunability, a superconducting MEMS varactor is integrated into a shunt band-stop resonator. A measured tunability of more than 25% is achieved by applying voltage to the plates of the varactor. Next, a proper band-stop filter design that can be tuned using MEMS-based varactors that provides a continuous tuning range of 20% is presented. Finally, it is proposed to use an all-pass filter to provide the 90° phase shift between resonators of a band-stop filter with just series or shunt resonators instead of λ/4 transmission lines. A miniaturized lumped element all-pass filter is also designed.

4.2 Lumped element BSF with alternating series and shunt resonators

To design a lumped element BSF, first the low-pass normalized prototype is constructed similar to the band-pass filter design. Frequency and impedance scaling and transformation to the band-stop prototype are done according to Table 3.1.

The basic circuit models for a 3-pole lumped element band-stop filter are shown in Figure (a) and (b).

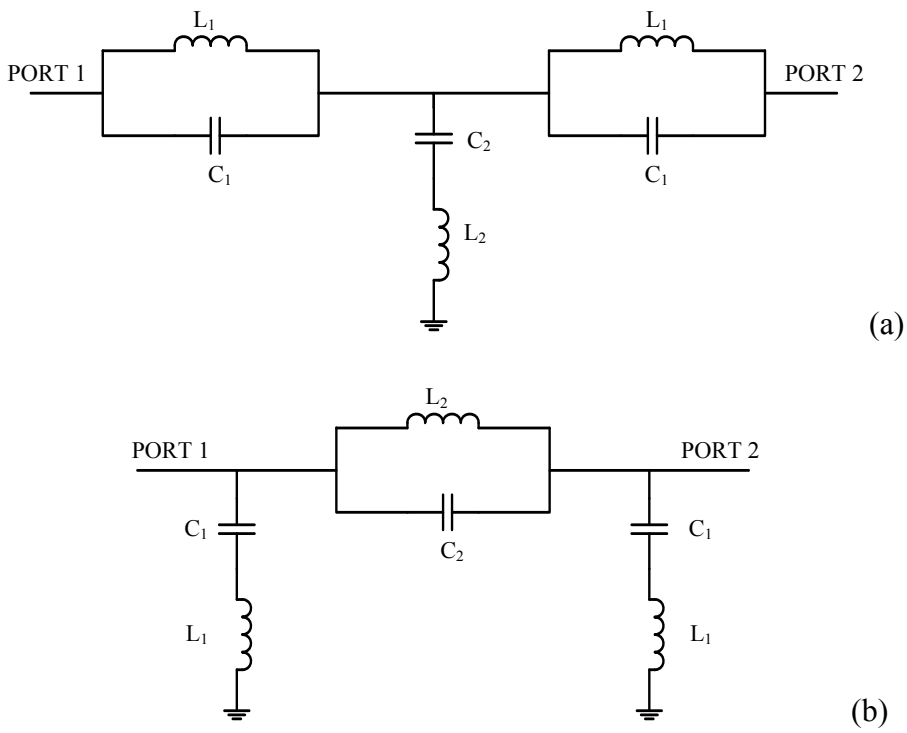

Figure 4.1 Circuit models for lumped element band-stop filters, (a) series-shunt-series and (b) shunt-series-shunt topology

Besides achieving miniaturization, one important advantage of a multilayer lumped element filter design is the fact that both series and shunt lumped element resonators can be realized in the same device. Consequently, lumped element filters with alternating shunt and series resonators can be designed, eliminating the need for impedance or admittance inverters. Since the common inverter for band-stop filters is a 90° matched transmission line, a design that eliminates the inverter can reduce the size of the filter significantly. The drawbacks of this topology are as follow:

The shunt resonator of a lumped element BSF has a large inductor and a small capacitor. On the other hand the series resonator for a BSF is the exact opposite. This results in a significant difference between the corresponding capacitor and inductor values in adjacent resonators. The difference intensifies as the bandwidth of the filter becomes narrower. As a result the device will

be more sensitive to imperfections caused by fabrication tolerances. Table 4.1 compares the inductor and capacitor values for two 3-pole Chebyshev BSFs with a centre frequency of 2GHz but with different percentage bandwidths. The filter on the left column is designed to have a percentage bandwidth of 5% while the designed bandwidth for on the right is 1%.

Table 4.1 Comparison between the component values of two BSFs with 5% and 1% bandwidths

3-pole BSF at 2GHz, 5% BW Series-shunt-series format	3-pole BSF at 2GHz, 1% BW Series-shunt-series format
$C_1 = C_3 = 47.4839$ pF	$C_1 = C_3 = 237.4195$ pF
$C_2 = 0.0798$ pF	$C_2 = 0.0160$ pF
$L_1 = L_3 = 0.1334$ nH	$L_1 = L_3 = 0.0267$ nH
L_2=79.3593 nH	L_2=396.7963 nH

The other problem of designing lumped element resonators for narrowband filters is that the inductors and capacitors which are either too big or too small become literally impossible to realize. For example, as shown in Table 4.1, to design a BSF at 2GHz with a 1% BW, an inductor value of almost 400nH is needed. A spiral inductor with such inductance value will probably have self resonance at frequencies much lower than the filter's centre frequency. The realization of a very low value inductance of 0.0267nH is not practical either. The same problem exists for realizing the capacitor values. A design method to overcome these problems is proposed in section 4.3.

4.3 Proposed Design Method

In this section, it will be shown that by adding an extra component to the resonators of a narrowband filter, the values of all the components of the resonator will lie in ranges that are more feasible for fabrication. It was noticed that in a sharp shunt band-pass resonator, adding a small inductor in series with the capacitor would moderate the value of the capacitor [19]. In the following, a detailed analysis of the impact of adding the proper component to a sharp resonator is presented. By applying this method to the design of a BSF with a 1% bandwidth, the values of the large inductors in the series resonators' shunt resonators and capacitors can be decreased by two orders of magnitude while maintaining the same performance.

For the series resonator, the goal is to reduce the value of the capacitor. It will be shown that the resonator can be redesigned to have three components as shown in Figure 4.2. In the new resonator, the value of C is divided by the factor 'a'. The values of the two inductors (L_p and L_s) shown in Figure 4.2(b) can be calculated in terms of the factor 'a' and the original inductor L.

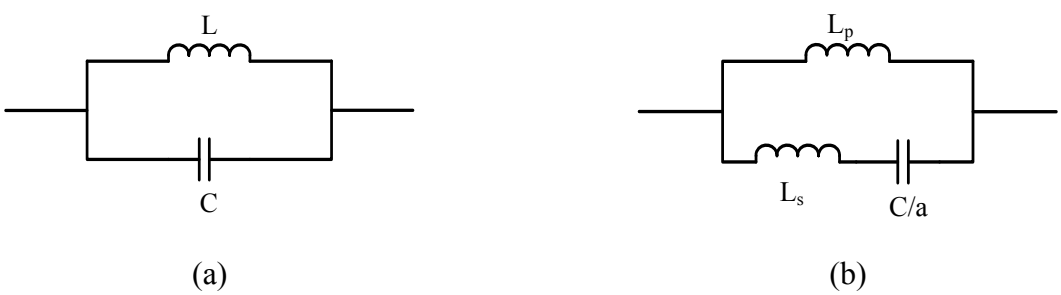

Figure 4.2 Circuit models for conventional and proposed series band-stop resonator

The proper values for L_p and L_s that make the performance of the proposed resonator to be the same as the conventional one at the centre frequency is calculated analytically. The S-parameter of both circuits with the calculated values will be demonstrated later.

In order to have the same resonance frequency for both resonators, the following equation should be satisfied:

$$LC = (L_s + L_p) \times \frac{C}{a} \tag{4.1}$$

$$L_p = aL - L_s \tag{4.2}$$

By equating the impedance of the both resonators the following formula is derived:

$$aL = (L_s - aL) \times (L_s C\omega^2 - a) \tag{4.3}$$

For frequencies close to the resonator's centre frequency it can be assumed that $LC\omega^2 \cong 1$. So $C\omega^2$ in the above equation can be replaced by $\frac{1}{L}$ with a good approximation.

$$L_s^2 - (2aL)L_s + L(a^2 - a) = 0 \tag{4.4}$$

Solving the above equation,

$$L_s = aL\left(1 - \frac{1}{\sqrt{a}}\right) \tag{4.5}$$

$$L_p = \sqrt{a}L \tag{4.6}$$

So for series resonator of the BSF with a 1% BW, if the new capacitor value is a 100 times smaller than the original value (a=100), the values of the inductor L_p and L_s should be 10 times and 90 times bigger than the L value in the conventional resonator respectively. Since the inductor value in the conventional resonator is really small and hard to design, it is even more desirable to be able to use inductor values that are 10 times and 90 times bigger.

Similarly it can be shown that the narrowband shunt resonator shown in Figure 4.3(a) can be replaced with a circuit in Figure 4.3(b) whose elements have reasonable values.

Figure 4.3 Circuit models for conventional and proposed shunt band-stop resonator

The correct values for C_s and C_p are calculated using a similar analysis to be:

$$C_p = aC\left(1 - \frac{1}{\sqrt{a}}\right) \tag{4.7}$$

$$C_s = \sqrt{a}C \tag{4.8}$$

The proposed 3-element resonator circuit should look exactly like the conventional 2-element resonator if a=1. The derived formulas for calculating the inductance and capacitance values also confirm this. If a=1 in these formulas, the value for the added element becomes zero as expected.

The question is, what is the maximum value that can be chosen for a? Adding a third component to the notch resonator generates an extra zero to its S_{11}. The frequency of this zero can be calculated easily to be $f = \frac{\sqrt{a}}{\sqrt{CL_s}}$ for the series resonator and $f = \frac{\sqrt{a}}{\sqrt{LC_p}}$ for the shunt resonator. As 'a' increases, the frequency of the new zero becomes closer to the centre frequency of the notch resonator. As a result, a multi-pole filter designed with this method will show the characteristics of a multi-pole low-pass filter at high frequencies. The cut off frequency of this low-pass filter depends on the value of 'a' as well. As an example, consider the circuit model of a 3-pole BSF shown in Figure 4.4. The S_{11} of this filter for different values of 'a' is simulated and

demonstrated in Figure 4.5. The filter is designed for a centre frequency of 2GHz and a percentage bandwidth of 1%. It is shown in the circuit simulations that 'a' can go up to 100 without affecting the response of the filter in the stop band. Figure 4.6 and 4.7 show the simulation results if a=500. It can be seen in Figure 4.6 that the return loss of the filter has become non-symmetric across the stop band. The low-pass behaviour of the filter at very high frequencies is shown in Figure 4.7. However, as shown in Figure 4.8 if the filter is designed for a different percentage bandwidth (10%), the maximum value of 'a' will be different.

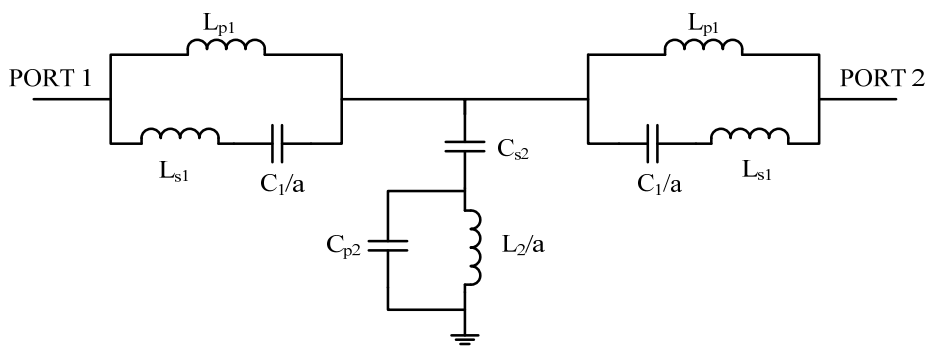

Figure 4.4 The circuit model for the proposed 3-pole BSF (series-shunt-series)

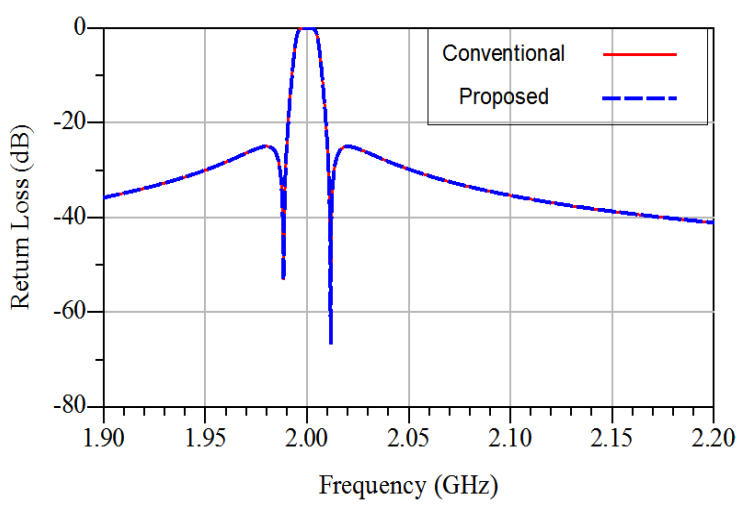

a=1

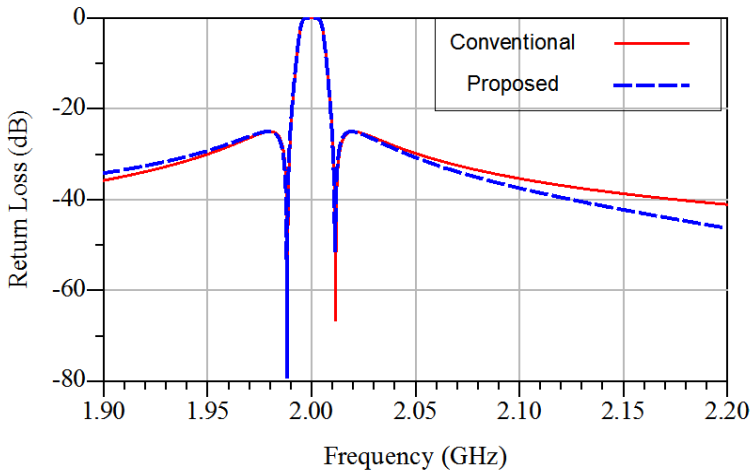

a=10

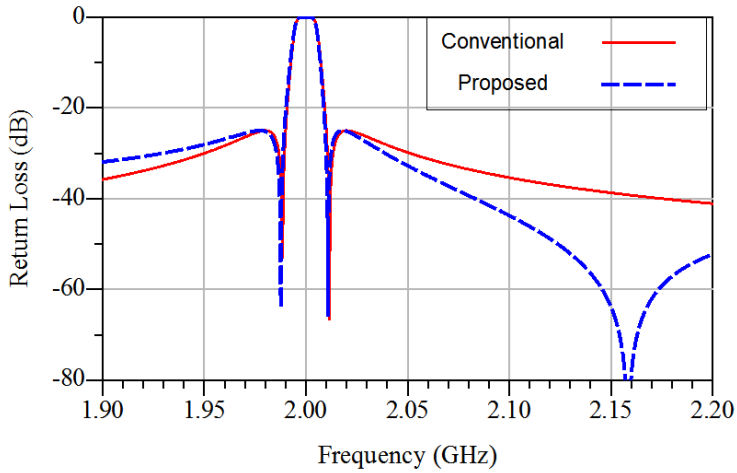

a=50

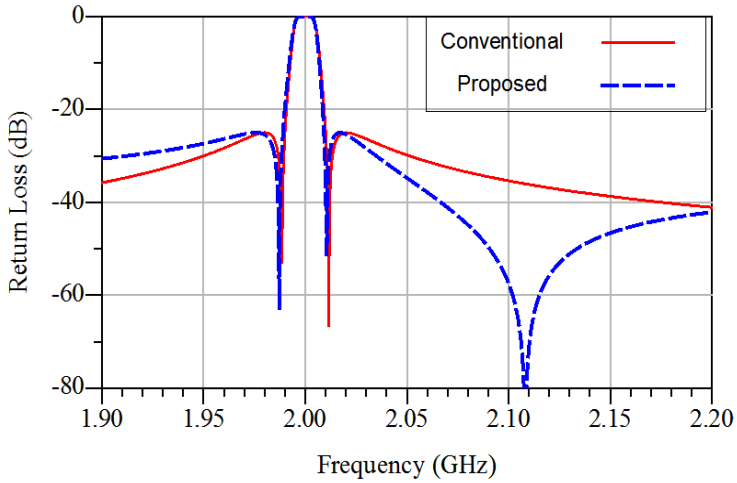

a=100

Figure 4.5 Comparison between the circuit simulation results of the conventional and proposed 3-pole band-stop filters with a 1% bandwidth for different values of 'a'

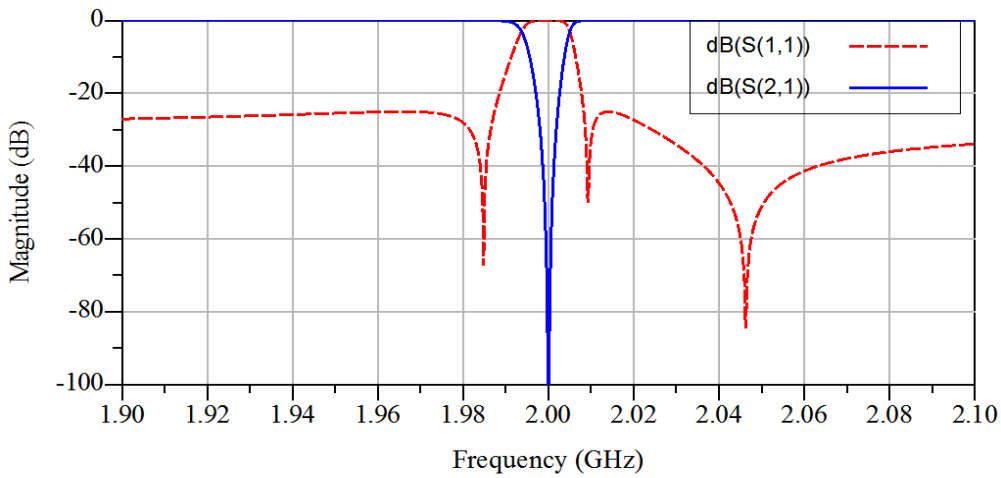

Figure 4.6 circuit simulation of the BSF designed with the proposed method when a=500

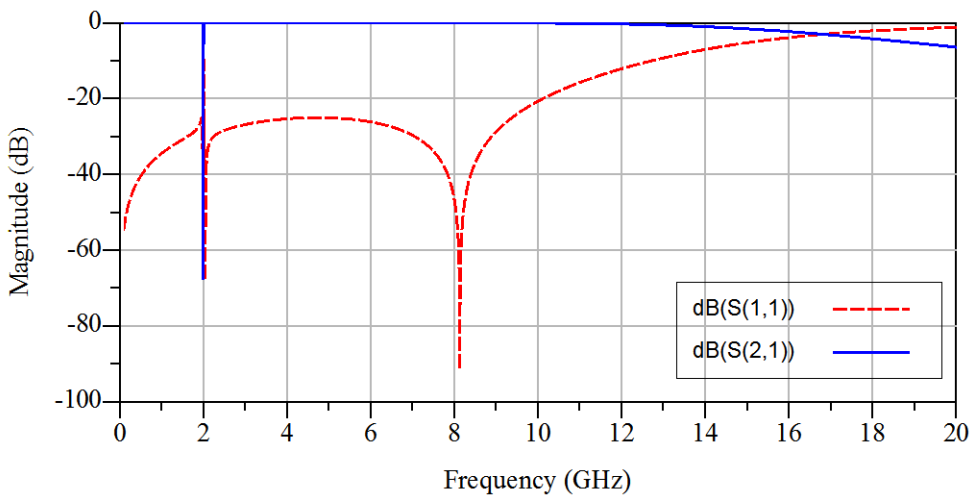

Figure 4.7 Low-pass behaviour of the proposed filter at high frequencies, a=500

Figure 4.8 shows the S-parameters for a BSF at 2GHz but with a 10% bandwidth when 'a' is changing. As shown in the circuit simulation results, for this bandwidth if 'a' is chosen to be more than 9, the other zeros of the S_{11} is shifted to lower frequencies resulting in a non-symmetric response in the stop band.

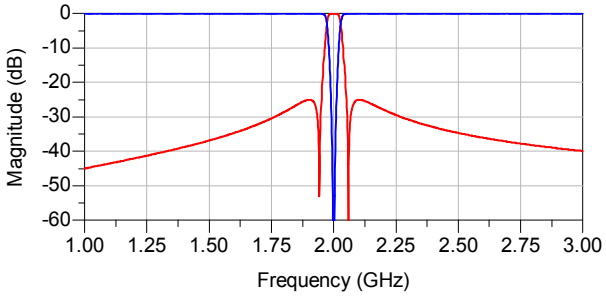

a=1

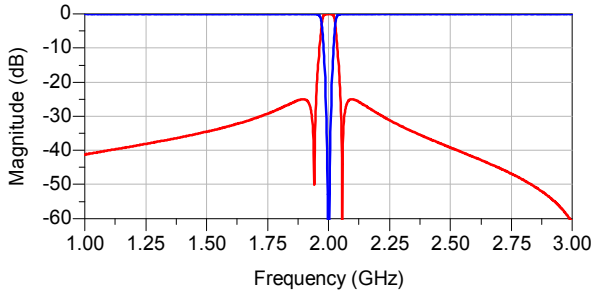

a=3

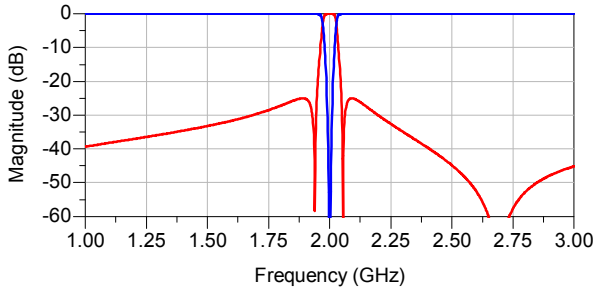

a=5

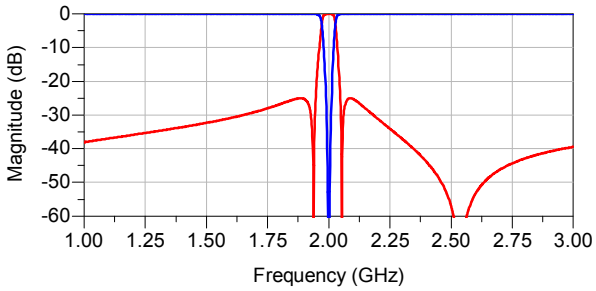

a=7

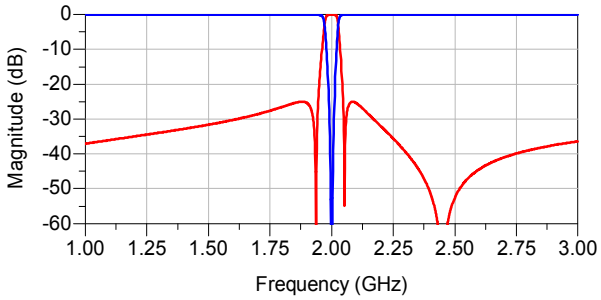

a=9

Figure 4.8 Circuit simulation for a BSF designed with the proposed method but a bandwidth of 10% for different values of 'a'

4.4 Design of a lumped element BSF using the proposed method

So far all the simulations were done on ideal lumped element circuits. To show the validity of the proposed method in practice, a 3-pole lumped element BSF at 2GHz is designed and simulated with an EM simulator. A shunt-series-shunt resonator combination is used. The percentage bandwidth that the filter is designed for is 1%. Figure 4.9 shows the circuit model of this filter.

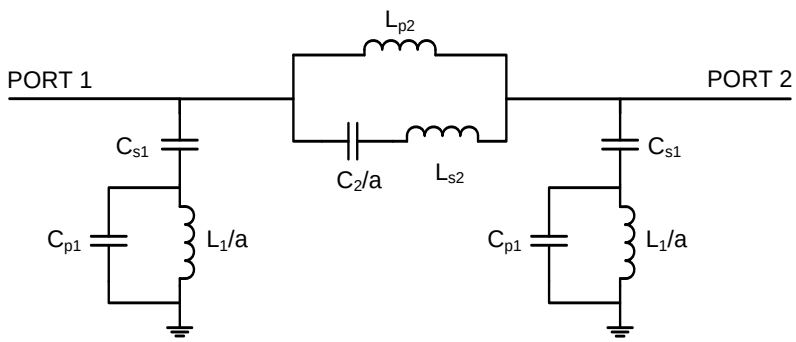

Figure 4.9 Proposed lumped element circuit model for a 3-pole BSF (shunt-series-shunt)

Table 4.2 shows the calculated inductance and capacitance values for such filter if it is to be realized using the conventional method.

Table 4.2 Component values for a BSF at 2GHz with a 1% BW

3-pole BSF at 2GHz, 1% BW

Shunt-series-shunt format

$C_1 = C_3 = 10.669$ fF

$C_2 = 158.7185$ pF

$L_1 = L_3 = 593.55$ nH

L_2=39.89815 pH

If a=100 is used, an inductance value of less than 6nH can be used in the first resonator; otherwise the inductor value has to be 593nH as calculated in Table 4.2. To realize the first shunt resonator, a 6nH spiral inductor is designed first. The capacitors in the resonator can be realized in a parallel plate format. To tune the resonator, the group delay method can be used easily. Although there are three components that can be tuned in this resonator, group delay can be matched just by tuning the capacitors because changing the inductor in the shunt resonator will just change the value of 'a'. So the tuning process will not be more complicated than that for the conventional resonators. Changing the dimensions of the capacitors individually will change the resonance frequency (location of the group delay curve peaks) and the value of the group delay while changing their ratio will just change the maximum value of the group delay.

In this work, each resonator was designed and tuned individually. Since in a Chebyshev band-stop filter all the transmission zeros have to be at the same frequency, it is very critical for the individual resonators to have the exact same resonance frequency. The peak of the reflected group delay however is not exactly at the resonator's centre frequency. On the other hand shorting and opening the series and shunt resonators can add some parasitic components, which in return results in a small error in the first tuning step, and consequently more challenges in tuning the cascaded multiple resonators. To minimize this error, each resonator was designed to have a 50 ohm termination at both ports and then a 2-port simulation was done on the individual resonators. The reflected group delay of each resonator was matched to the corresponding ideal 2-port circuit simulation. The three resonators were then cascaded to make the 3-pole filter. This method of design is particularly beneficial in terms of tuning, because after cascading the resonators the end result is really close to the defined characteristics, as a result a slight tuning will do the job.

The individual resonators with their simulated group delay are shown in Figures 4.10 and 4.11. The 3-D model and EM simulation of the final filter are shown in Figure 4.12 and 4.13 respectively. Figure 4.14 shows the EM simulation results in wide frequency range. Different colors in the 3-D model represent different metal layers. Blue is the first metal layer on top of the substrate (M0), pink is the second metal layer (M1) and green is M2.

The dimensions of the designed filter are 1.25×0.5mm or 0.625mm^2. If the filter were to be designed with the conventional two element resonators, the area of the capacitor in the series resonator itself would be just 0.57mm^2. Thus the filter is miniaturized to a great extent.

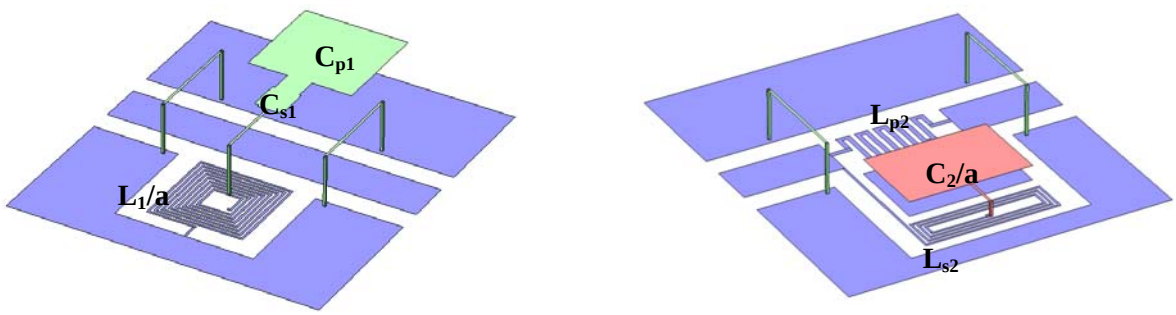

Figure 4.10 3D models for the first and second resonator of the BSF at 2GHz with a 1% BW

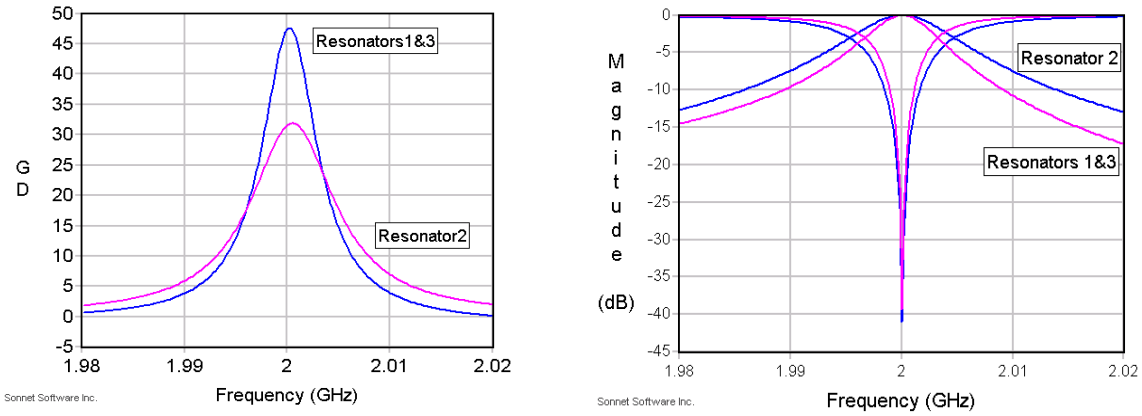

Figure 4.11 Group delay and S-parameter response of each resonator for the BSF with a 1% BW

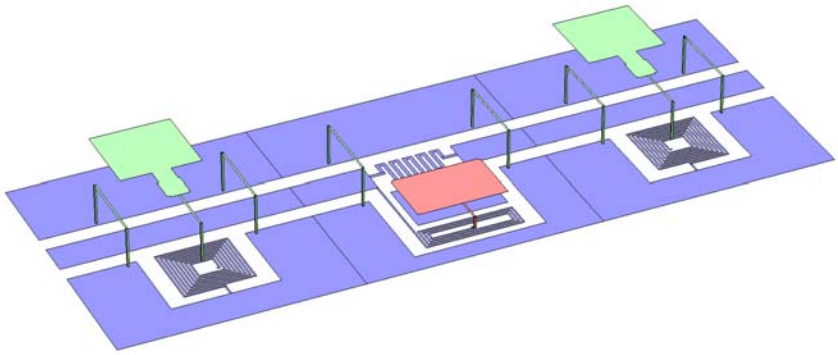

Figure 4.12 3D model for the 3-pole BSF at 2GHz with a 1% BW

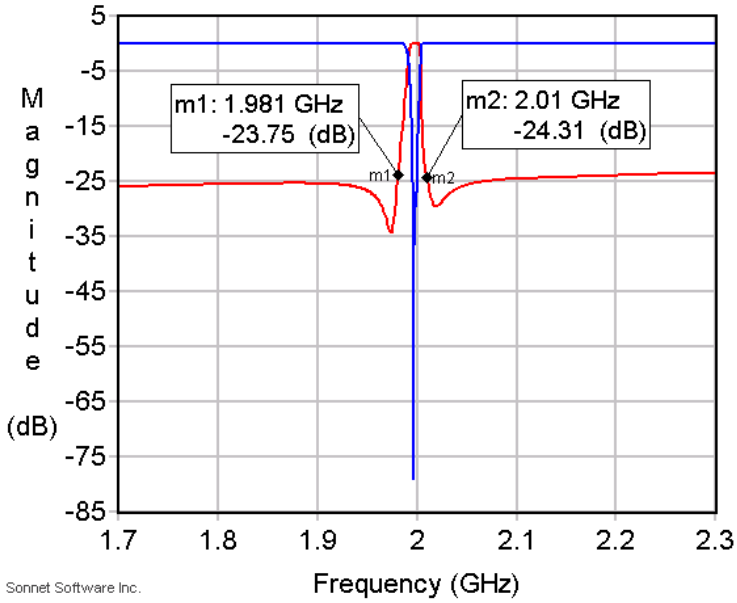

Figure 4.13 EM simulation results for the 3-pole BSF at 2GHz with a 1% BW

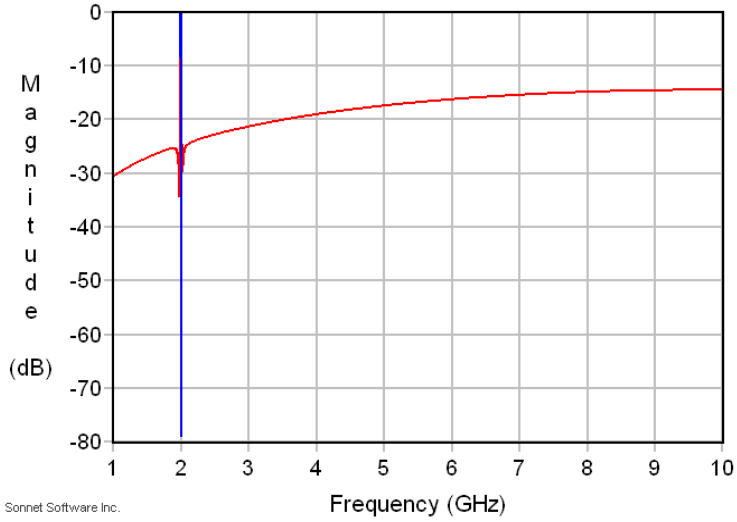

Figure 4.14 EM simulation results in wide frequency range

4.5 Design and realization of a 3-pole BSF with both shunt and series resonators

A 3-pole BSF at 2GHz with a 5% bandwidth is designed, fabricated and measured. The series-shunt-series combination of resonators was used. The circuit model of the filter is shown in Figure 4.15. The g-values for a 3-pole filter with a 25dB return loss is calculated using the equations (3.8).

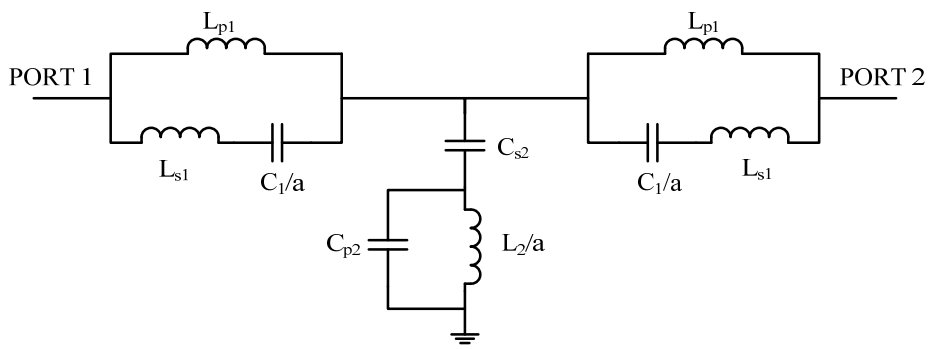

Figure 4.15 The circuit model chosen to design the BSF at 2GHz with a 5% BW

The inductance and capacitance values can be derived from the g-values using the equations in Table 3.1. The final values for the inductors and capacitors are presented as the following:

L_1=0.1334 nH L_2=79.3593 nH L_3=0.1334 nH

C_1=47.4839 pF C_2=0.0798 pF C_3=47.4839 pF

The proposed method (resonators with 3 elements) is used in this design to make it easier to be realized. First each resonator was designed and tuned individually to match its group delay to the corresponding resonator in the ideal circuit model.

Figure 4.16 shows the 3-D model of the individual resonators and their simulated group delay. The layout of the tuned BSF is shown in Figure 4.17. Figure 4.18 shows the final EM simulation

of the filter. This filter is fabricated by the HYPRES process. Figure 4.19 shows the measurement results for this device.

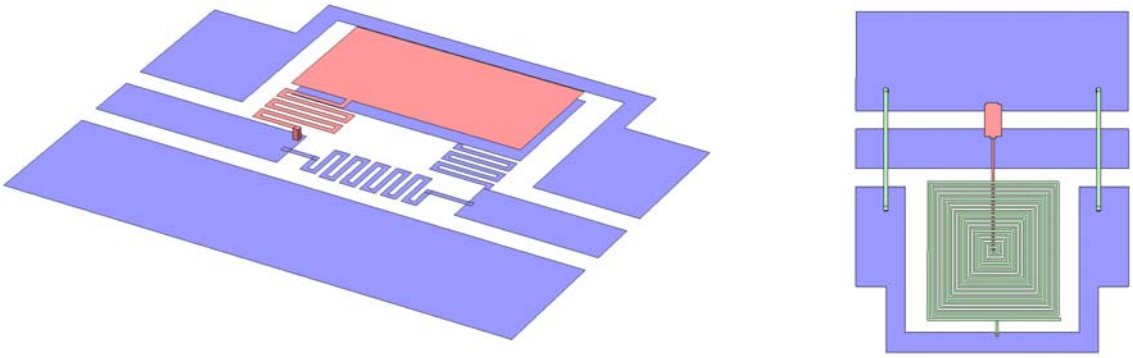

Figure 4.16 layouts of the first and second resonators of the BSF with a 5% BW

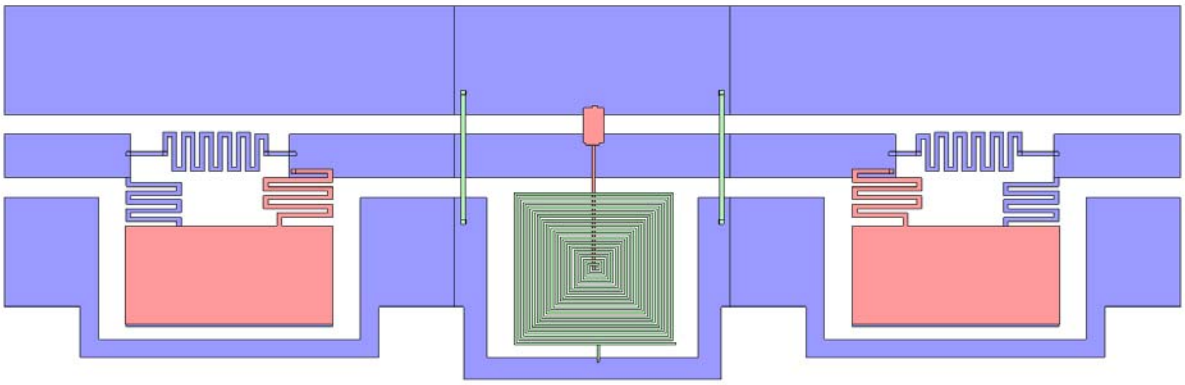

Figure 4.17 Layout of the 3-pole BSF at 2GHz with a 5% BW

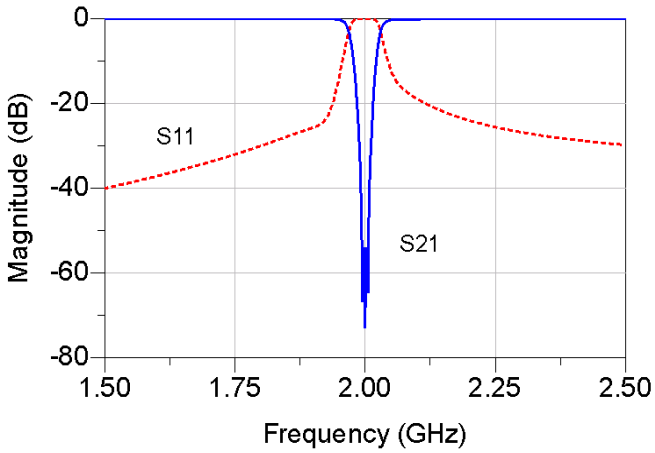

Figure 4.18 EM Simulation results for the BSF with a 5% BW

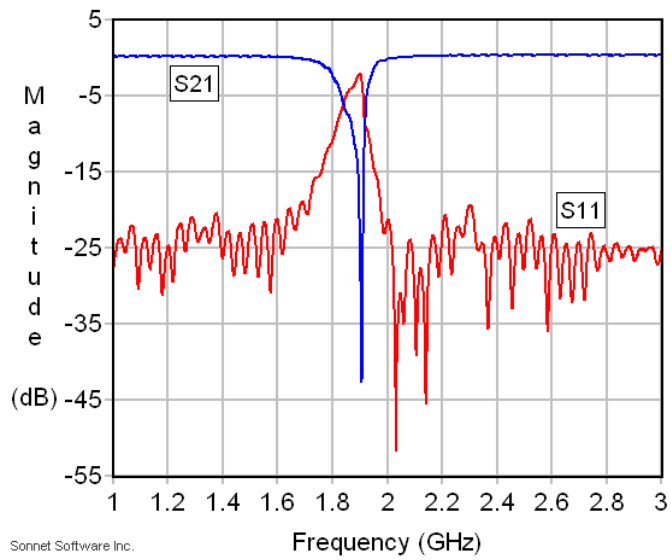

Figure 4.19 Measurement results for the BSF with a 5% BW

The discrepancy between the simulation and measurement results is extensively studied. New bandstop filters are designed and simulated with modified parameters considering some potential sources of error. The newly designed filters are fabricated and measured. Other sources of error are discovered by matching the simulation and measurement results of the new filters. Therefore, the sources of error are summarized as follows:

1- The dielectric constant used in the simulation is different from the measured value.
2- Sonnet EM simulator, by default, subsections each metal layer by checking just one metal layer on top and one beneath it. In other words, if the design has 3 metal layers, the effect of the third layer on the first layer is not properly accounted for in the simulation result. The subsectioning setting should be changed for designs which include more than 2 layers as explained in section 4.5.1.
3- Poor choice of cell size for a design with both spiral and meander line inductors contributes to inaccurate simulation results.

4- Kinetic inductance is not considered in the EM simulation. The lack of this consideration generates a noticeable error in simulation results of designs with both series and shunt resonators. The total kinetic inductance depends on the number of squares in the design which affects the inductors in particular. The resonator with a meander inductor will experience a larger shift in its resonance frequency when kinetic inductance exists. This results in a separation of the transmission zeros in the band-stop filter.

The new bandstop filter designs and sources of errors are discussed in details in the following.

4.5.1 Investigation of discrepancy between simulated and measured result

According to the HYPRES foundry website [22], the capacitance between the layers M0 and M1 is 0.28fF/μm^2 ±20%. The large variation of this capacitance explains the shift in the filter's center frequency.

<u>Subsectioning Settings in Sonnet</u>

As mentioned briefly earlier, the subsectioning settings that Sonnet uses by default is valid for a design with just two layers. For example a simple microstrip transmission line is simulated using the default subsectioning settings in Sonnet. The dielectric layer has a relative permittivity of ε_r and thickness of t. Figures 4.20 shows the mesh generated by Sonnet on the ground plane of the transmission line. It can be seen that the density of the sections is higher in the center of the ground plane because the software recognizes that there is a metal at that spot on the top layer (the signal line) that can affect the response of the device. This simulation shows that the transmission line has a characteristic impedance of 50.5Ω. In another simulation the same device is simulated, but instead of just one layer of dielectric with a thickness of t, three dielectric layers with the same permittivity and thicknesses of t_1, t_2 and t_3 are used. The total thickness is the same

as t. Although the two devices are exactly the same, simulation of the second device shows a characteristic impedance of 96.4Ω. Figure 4.21 shows the generated mesh for the second device. The density of mesh is the same on the ground plane except for the edges. That means that the software does not recognize the existence of the signal path that is on the third layer of dielectrics, simply because the subsectioning setting is not right.

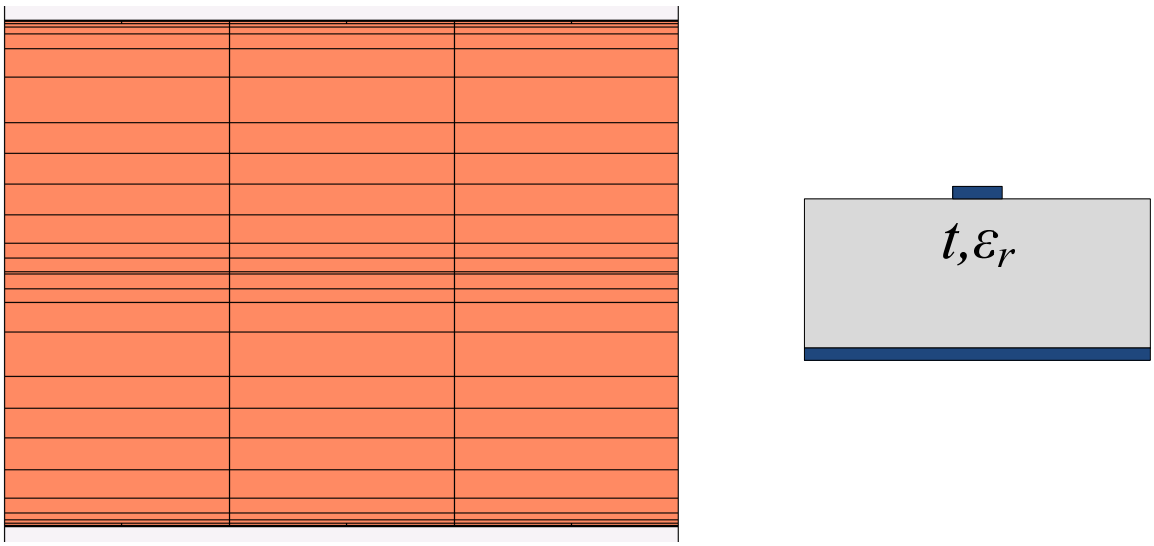

Figure 4.20 The mesh generated by Sonnet on the ground plane of a microstrip TL with one layer dielectric.

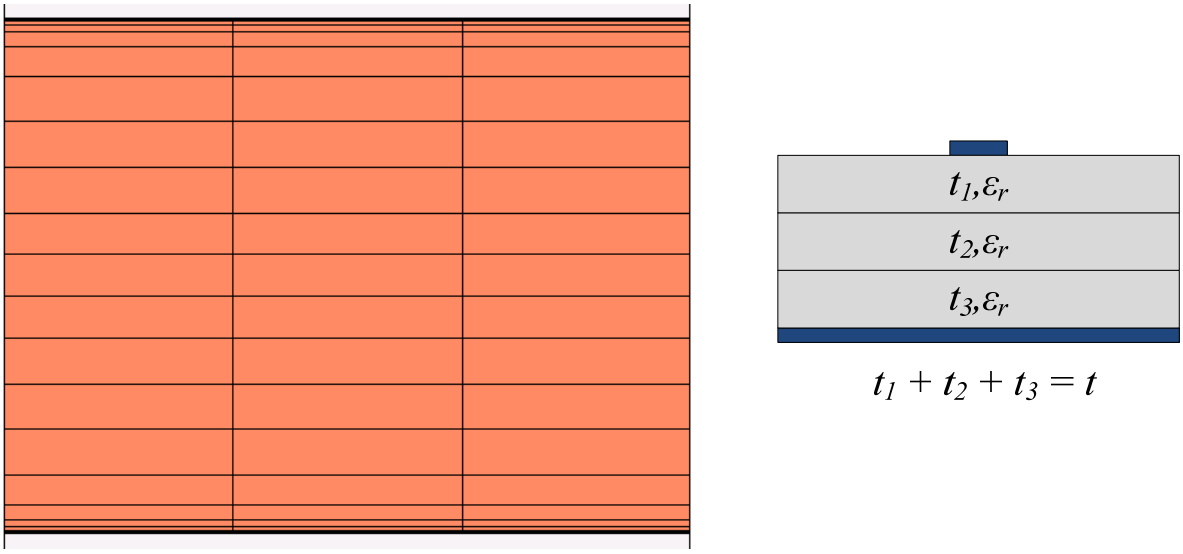

Figure 4.21 The mesh generated by Sonnet on the ground plane of a microstrip TL with multi- layer dielectric.

To change this setting, one can choose the “Advanced Subsectioning” from the “analysis” menu in the project editor of Sonnet software, put a check mark beside the “Polygon Edge Checking” and insert the number of layers to be checked in the box in front of this option.

Proper choice for Cell size:

It is clear that if the simulation results of the same device with different cell sizes are different, the results are not accurate. Therefore the proper cell size is the one that generates the same response as the one with smaller cell size. However, the memory of the system that runs the simulation limits the total number of cells in the design.

The minimum width of line is used for the inductors in all the resonators of the BSF. The width of the spiral inductor in the middle resonator is 3µm while the width of the meander line in the first and last resonators is 6µm. Considering the minimum widths in the layout, it was assumed that a cell size of 1µm×1µm provides accurate results. However, it was confirmed later by simulation that a smaller cell size of 0.5µm×0.5µm shifts the resonance frequency of the series resonators (first and last) to a higher frequency as shown in Figure 4.22.

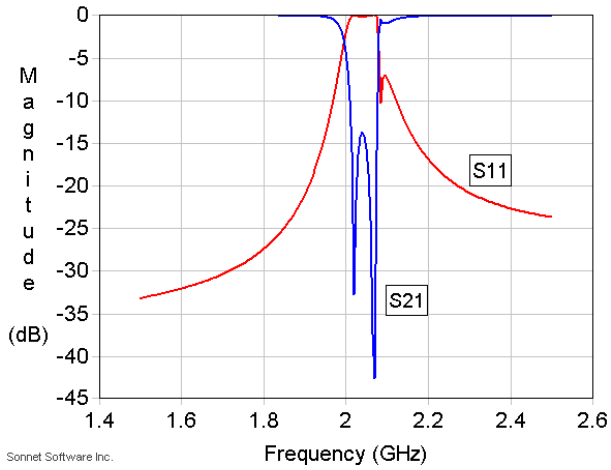

Figure 4.22 Simulation results of the 3-pole BSF with smaller cell size.

It was noted by simulation that the inductance value of the meander line is changing with the choice of a smaller cell size. To investigate the proper cell size for a meander line inductor, a series of simulations is done on a meander line inductor with a width of 24μm. Similar simulations are also done on a spiral inductor with a width of 24μm. the cells chosen for simulations are squares with dimensions of 24, 8, 4, 2 and 1μm. The relative change of inductance in both inductors at 1 GHz is compared as the cell size decreases. The calculated change in the spiral inductor's value when the cell size decreases from 8μm to 4μm is about 0.7%. The same variation in the inductance value of the meander line happens when the cell size decreases from 2μm to 1μm. Assuming that this error is acceptable, the meander line inductor should be designed in a way that its width has between 10 to 12 cells.

Kinetic Inductance

The superconductive effect known as "kinetic inductance" slows the velocity of the electrons with no loss of energy. This can be modeled as a surface inductance. Kinetic inductance is a function of temperature and can be approximated by equation (4.9).

$$L_s = \mu_0 \lambda_L(T) \tag{4.9}$$

Where $\mu_0 = 4\pi \times 10^{-7}$(H/m) and $\lambda_L(T)$ is the London depth of penetration at temperature T.

$$\lambda_L(T) = \frac{\lambda_0}{\sqrt{1 - \left(\frac{T}{T_c}\right)^4}} \tag{4.10}$$

Where λ_0 is the London depth at T=0 and has a unit of meter. T_c is the critical temperature of the superconducting material. According to the HYPRES foundry, λ_0= 90nm for all the

superconducting layers in the process. So the kinetic inductance value will be around 0.115pH/□ at the liquid Helium temperature (4K).

It is shown in the next BSF designs that the kinetic inductance affects the resonators with a meander line inductor more than the ones with spiral inductor. Therefore the resonance frequency of the series resonator changes more than that of the shunt resonator. In the case of a bandstop filter, the zeros separate as a result of this effect.

4.5.2 BSF at 1GHz with 10% bandwidth

Series-shunt-series topology

A 3-pole band-stop filter at 1GHz with a 10% BW was designed, fabricated and measured. As mentioned earlier, one reason for the discrepancy between the simulated and measured results for the BSF at 2GHz in Figure 4.17 was the choice of cell size for simulation. In this design, each resonator was tuned separately by the smallest cell size possible that can be simulated (before the simulating machine runs out of memory). The whole filter could not be simulated with the same cell size used for its resonators. Alternatively the filter could be subdivided into three resonators to be simulated. Since there is not a lot of coupling between the lumped element resonators, subdividing the circuit will not affect the results much. The component values for this filter are as the following:

L_1=0.5335 nH L_2=79.3593 nH L_3=0.5335 nH

C_1=47.4839 pF C_2=0.3192 pF C_3=47.4839 pF

In order to miniaturize the capacitors in the first and third resonators, three metal layers (M0, M1 and M2) were used to make 2 capacitors in parallel. Figure 4.23 shows the layout for the filter. Different colors in the layout represent different layers in the process. The simulation results for this filter are presented in Figure 4.24.

It should be noted here that the kinetic inductance was not considered in the EM simulation. Figure 4.25 shows the measured result for this filter. By adding the kinetic inductance to the metal in the simulation and changing the dielectric constant to the measured one, the simulation result matched the measured results to a great extent as shown in Figure 4.26.

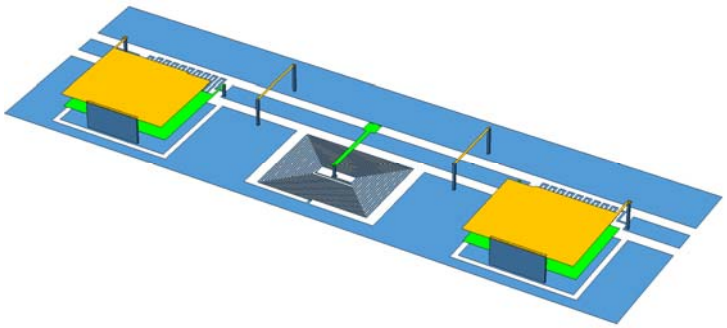

Figure 4.23 3D model of the BSF at 1GHz with a 10% BW

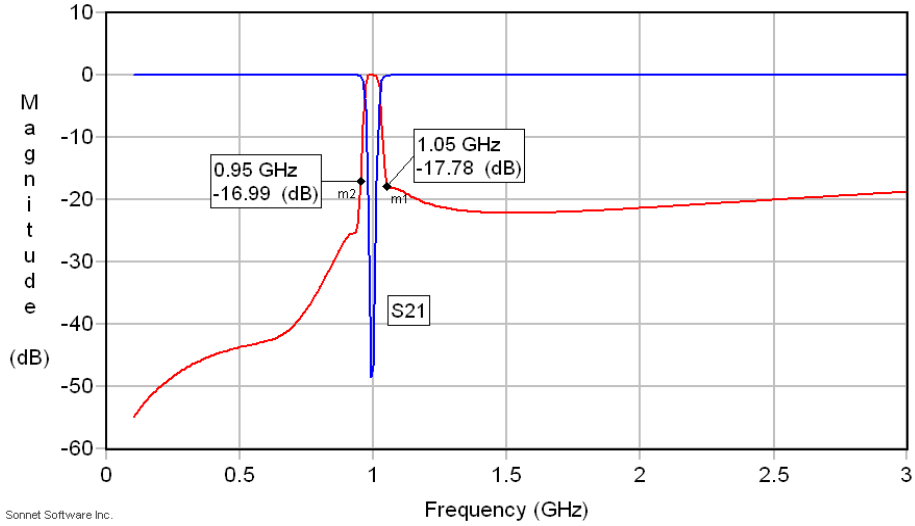

Figure 4.24 EM simulation results of the BSF with a 10% BW

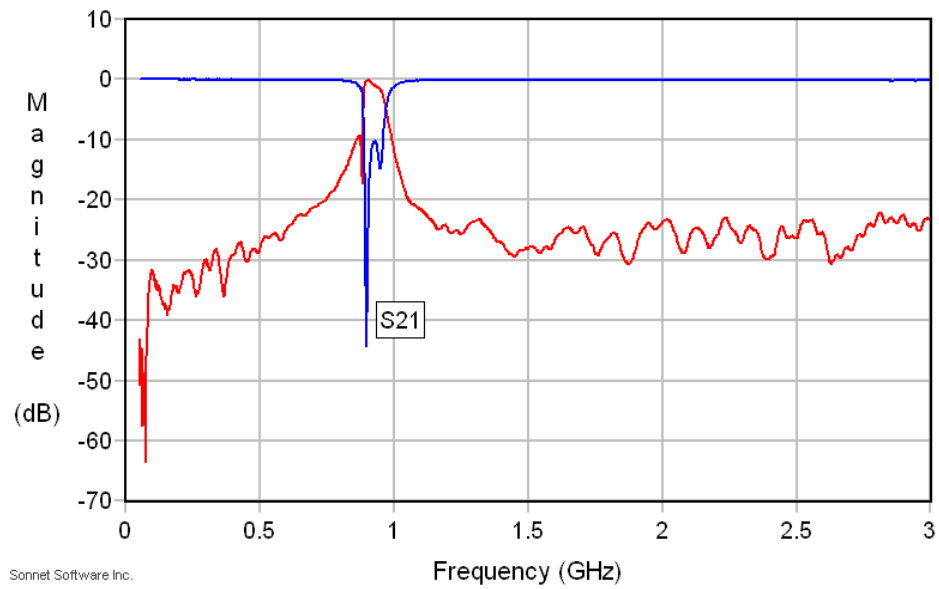

Figure 4.25 Measurement results of the BSF with a 10% BW

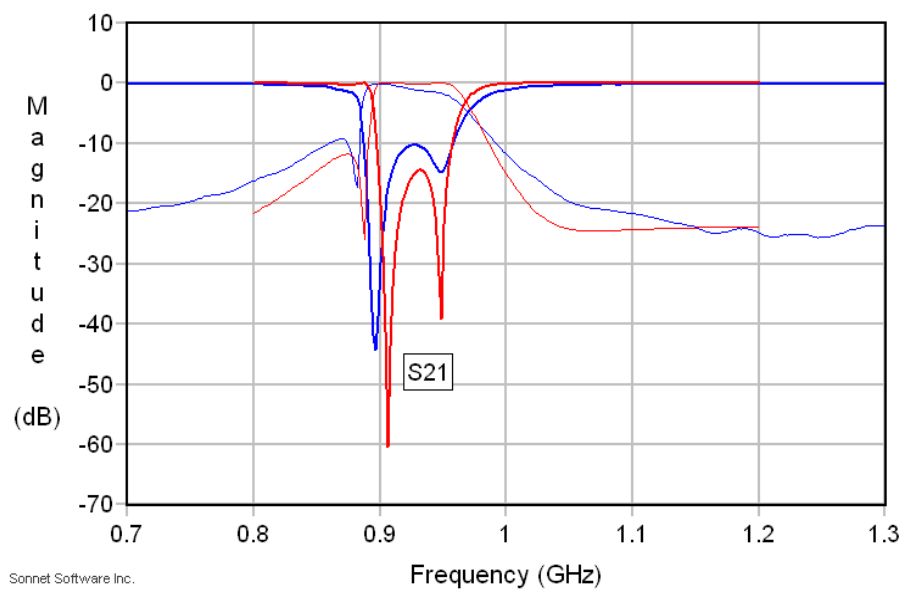

Figure 4.26 A comparison between simulation and measurement results of the BSF with a 10% BW by including the kinetic inductance of the Nb

It is interesting to note that the kinetic inductance will affect the meander inductor more than that of the spiral inductor. This is attributed to the fact that the ratio of number of squares to the inductance value is much larger for the meander inductors. For example, in the layout of the BSF at 1GHz, the meander inductor in the first resonator with a value of 0.5335nH has approximately 130 squares, while the spiral inductor in the second resonator is 79.3593nH and has approximately 6280 squares. Assuming that the temperature of the device is 4K at the time of measurement, the kinetic inductance of one square is 0.115pH. So the meander inductor value increases by 14.95pH which is 2.8% of its nominal value while the spiral inductor value increases by 0.7222nH which is just 0.91% of its original value.

The gold wirebonds that connect the device to the CPW line in the housing also cause some discrepancy between the simulated and measured results. The sets of gold wirebonds used for the measurement have a diameter of 25um and a length of almost 2mm each.

Shunt-series-shunt topology

Another band-stop filter with the same specifications (at 1GHz with a 10% BW) was designed and fabricated but a shunt-series-shunt topology was used. The design process was exactly similar to the previous one. The simulation result for this filter is presented in Figure 4.28 whereas Figure 4.29 shows the measured results. Unfortunately the kinetic inductance was not considered in the simulation. This explains the discrepancy between measured and simulated results. Figure 4.27 shows the 3D model of the filter.

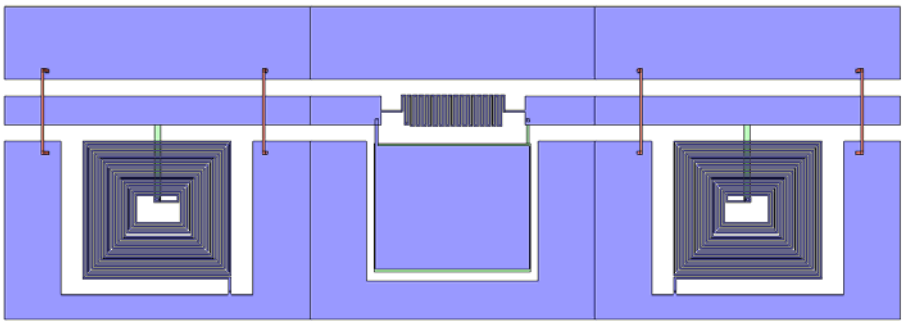

Figure 4.27 Layout of the BSF at 1GHz with a 10% BW (shunt-series-shunt)

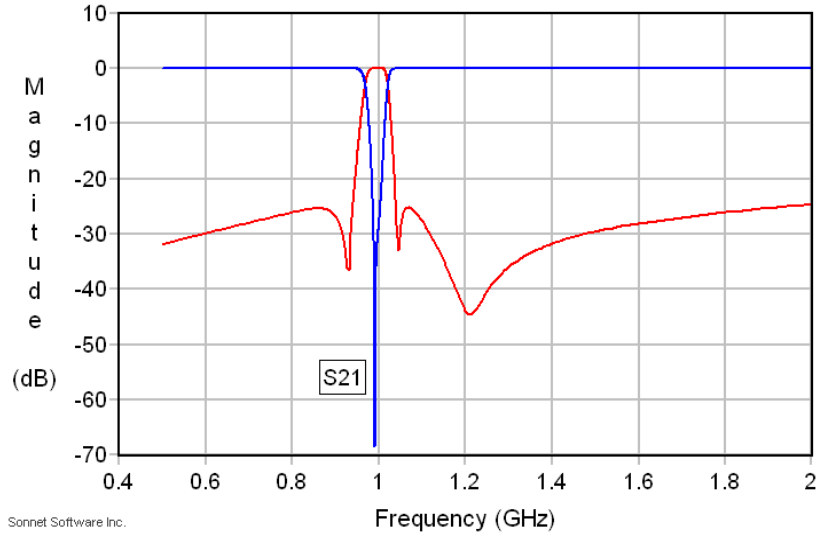

Figure 4.28 EM simulation results for the BSF with a 10% BW

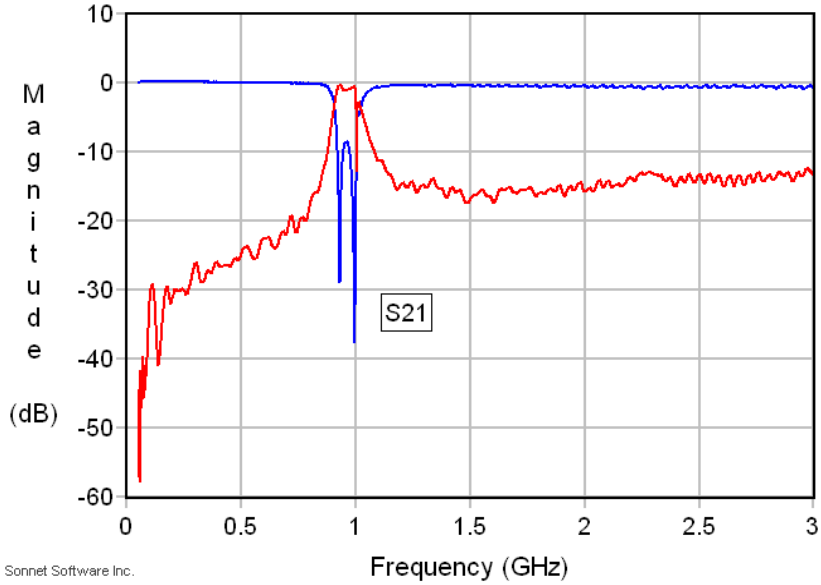

Figure 4.29 Measurement results of the BSF with a 10% BW (shunt-series-shunt)

4.6 BSF with lumped all shunt resonators

It is more often desirable to have just one kind of resonator in a filter, either shunt or series. This can be done easily in lumped element band-pass filters using lumped element inverters. However, band-stop filters should provide a good match for a very wide frequency band (ideally all frequencies except for the stop band). To realize a band-stop filter with a one kind of resonator, a 90° phase shift should be provided between the resonators. The inverter should not cause any attenuation outside the band. A simple way to realize such an inverter is to use a λ/4 transmission line. Since the phase of a transmission line varies by frequency, the percentage bandwidth of the filter realized with this method cannot exceed 10%. Another drawback of using transmission lines is that they can be very spacious and long.

A band-stop filter at 2GHz with a percentage bandwidth of 10% was designed, fabricated and measured. The resonators of this filter are all shunt and designed with lumped element inductors and capacitors. The 90° phase shift between the resonators is provided with λ/4 meandered microstrip transmission lines. Figure 4.30 shows the schematic of this filter.

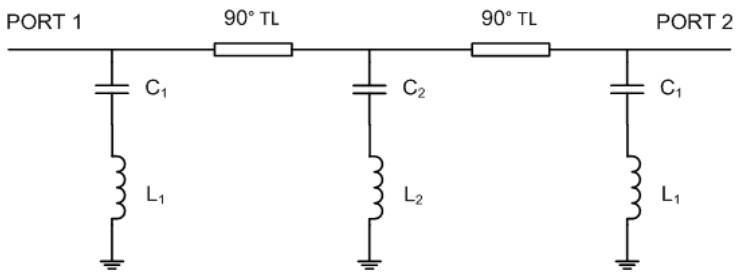

Figure 4.30 Schematic of a 3-pole BSF with lumped resonators and 90° transmission lines

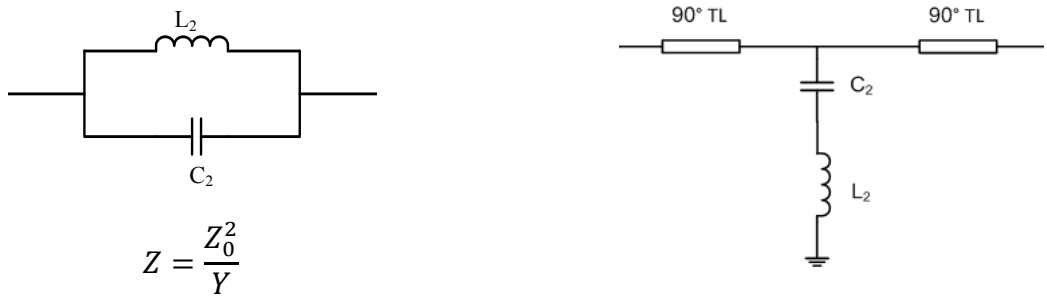

$$Z = \frac{Z_0^2}{Y}$$

Figure 4.31 Equivalent circuits at the resonance frequency of the resonators

As mentioned before, there are 3 layers of dielectric (silicon dioxide) in the HYPRES process with a total thickness of 0.85µm. To design a 50Ω microstrip transmission line with such a thin oxide layer, the width of the transmission line should be less than 2µm. However, the minimum width allowed by the foundry to use on the top metal layer (M3) is 2µm. By adding some defects to the ground plane of the transmission line a characteristic impedance of 50Ω could be achieved with a width of 2.5µm. Moreover, by including the defects, the 90° phase shift could be achieved by a slightly shorter length of line. Figure 4.33 compares the S-parameters of the designed transmission line with and without the defects in the ground plane.

The transmission line layout is shown in Figure 4.32. Since the width of the transmission line is so small, it could be meandered and fit into a smaller space. The designed λ/4 transmission line with the defected ground plane has a dimension of less than 1.2mm by 0.65mm.

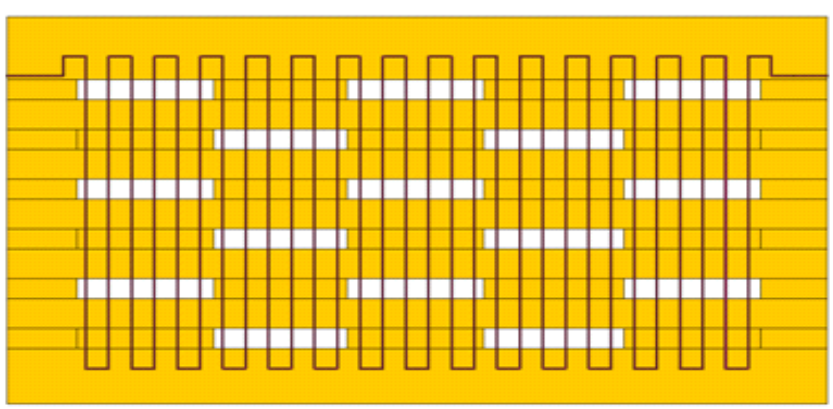

Figure 4.32 Layout of the 90° TL with defected ground plane

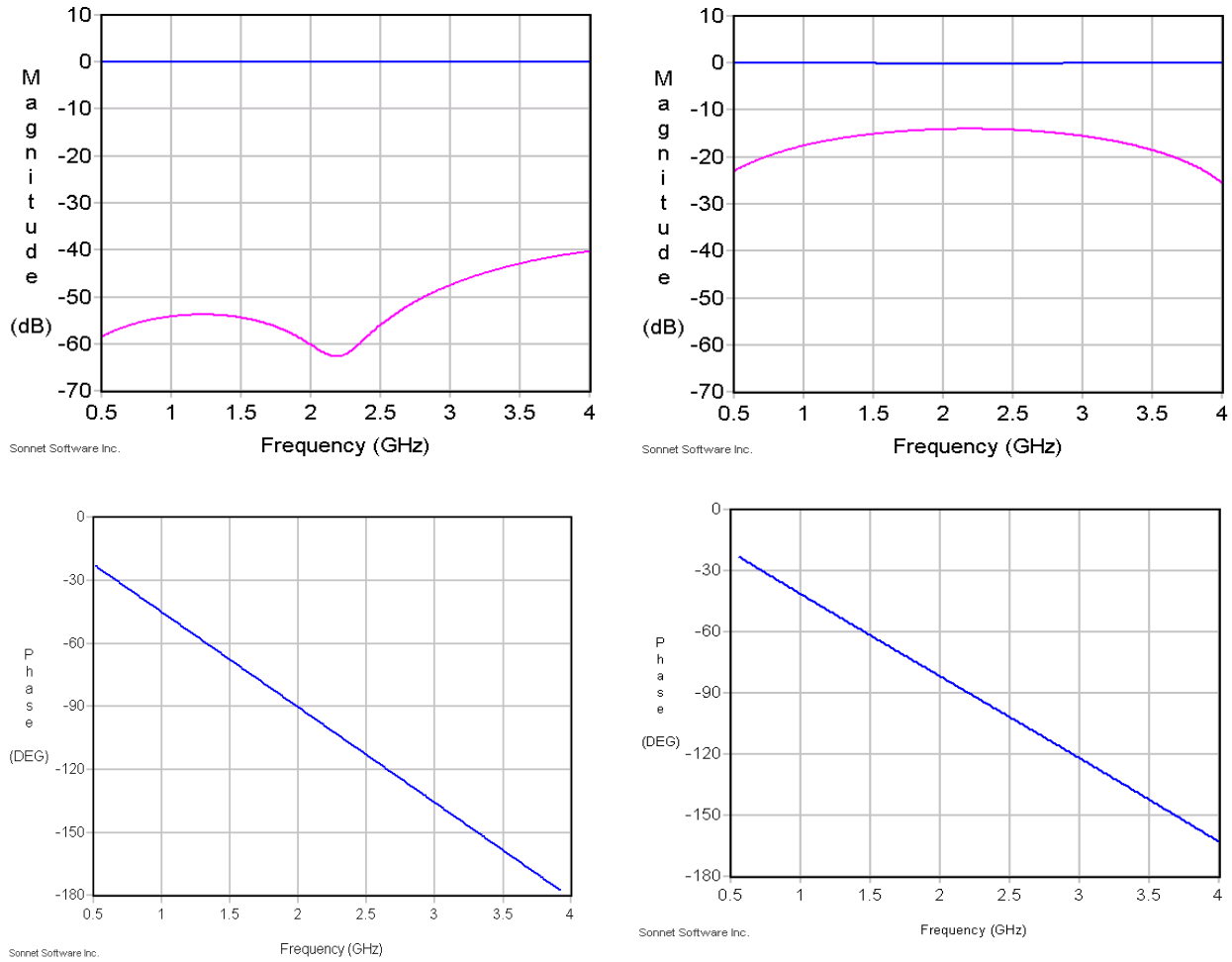

Figure 4.33 Comparison of the S-parameters and electrical lengths of transmission lines with and without defected grounds

The resonators of the filter were designed and tuned individually until their group delay matched to the group delay of the ideal circuit model. The filter is shown in Figure 4.34. Simulation and measurement results of the filter are presented in Figure 4.35 and 4.36. Figure 4.37 shows the measured results in a wide frequency range.

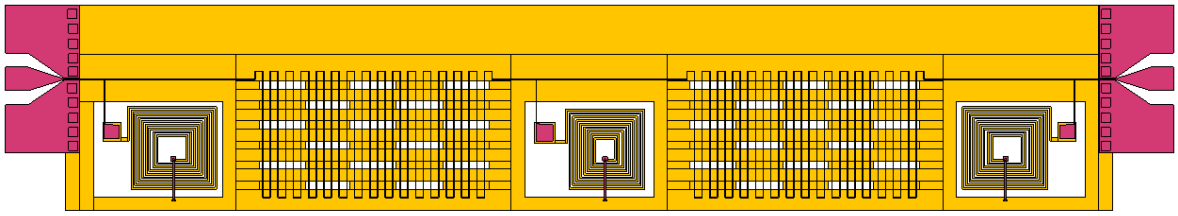

Figure 4.34 Layout of the 3-pole BSF with lumped resonators and 90° microstrip TLs

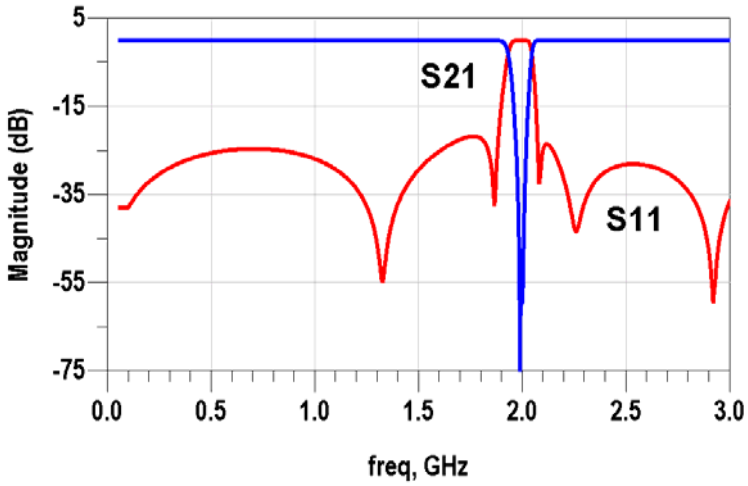

Figure 4.35 EM Simulation results of the 3-pole BSF with 90° TLs

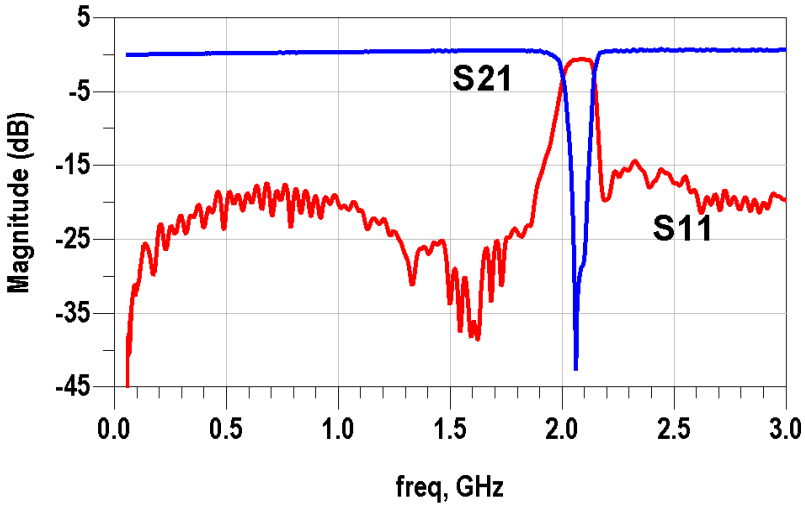

Figure 4.36 Measurement results of the 3-pole BSF with 90° TLs

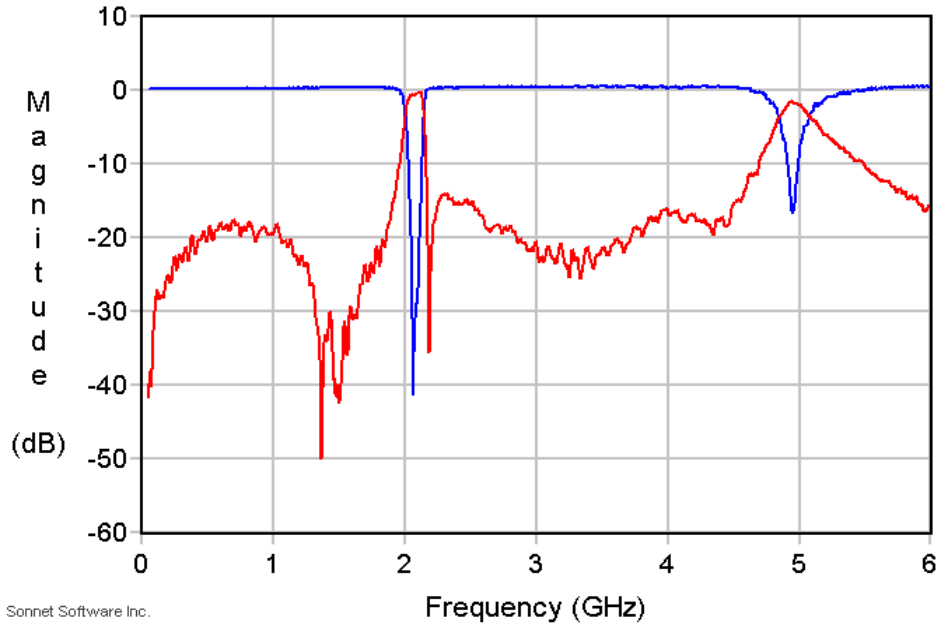

Figure 4.37 Measured results of the BSF with all shunt resonators in wide frequency range

4.7 Tunability of superconducting lumped element band-stop filters

It has been shown in our group that MEMS varactors and switches at cryogenic temperatures can be realized by doing some post processing on the devices fabricated by HYPRES [1].

The RF MEMS varactors used in the tunable resonators were electrostatically actuated. Figure 4.38 shows the 3D model of a varactor created using CoventorWare software. Using this software, the mechanical performance of the MEMS varactor can be evaluated.

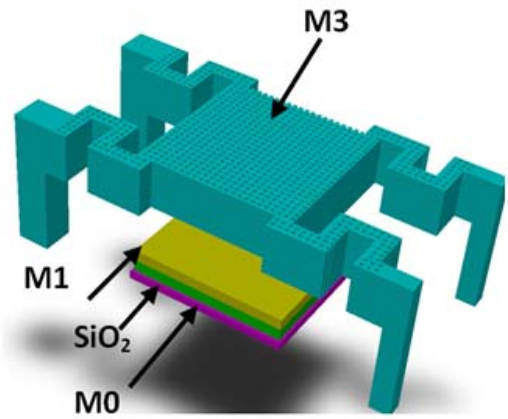

Figure 4.38 3D model of an RF MEMS varactor realized with HYPRES process [20]

As shown in the picture, three metal layers are used in this varactor. The biasing voltage is applied between M0 and M3. Since M3 is the movable plate, the dielectric layer between M3 and M1 (sacrificial layer) has to get etched away to create an air gap. In order to do that, the chip should go through a wet etching process. The release holes should be designed placed over the entire moving plate so the wet etching can be fast and isotropic. A plate is designed to be on M1. This plate will cover the dielectric layer between M0 and M1 and protect it from being etched away during the release process. This will prevent the occurrence of a short circuit between the electrodes of the varactor (M0 and M3). The designed varactor can be modeled by a fixed and a tunable capacitor in series.

A few tunable superconducting band-stop resonators were realized by employing MEMS varactors.

The SEM picture of the first tunable resonator is shown in Figure 4.39. The measured resonance frequency of the notch before applying any voltage (when the moveable plate of the varactor is in its upstate position) was at 3.218GHz as shown in Figure 4.40. Voltage was applied through a bias tee between the signal and the ground of the CPW transmission line. The first shift in the

resonance frequency was noticed at V=9V. A continuous tuning of a resonance frequency between 3.218GHz and 2.571GHz (more than 20%) was achieved by increasing the applied voltage to 78V.

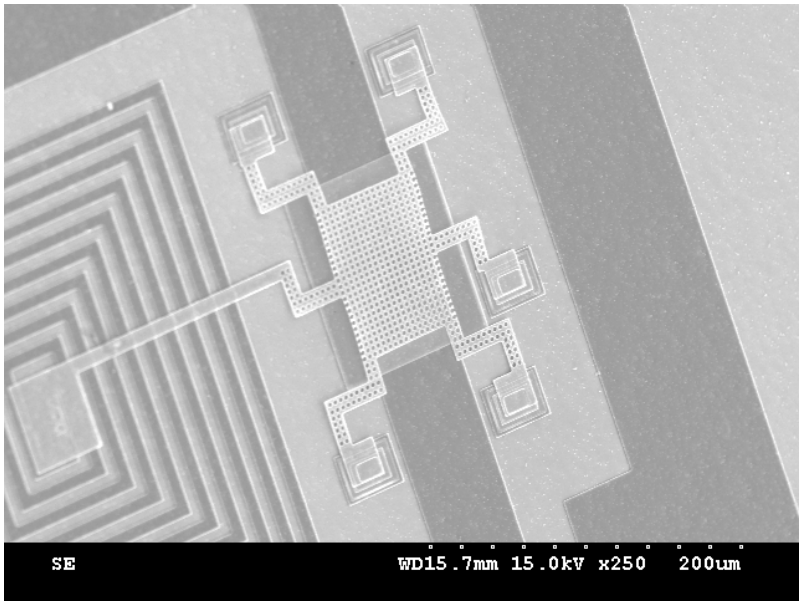

Figure 4.39 SEM picture of tunable resonator 1 [20]

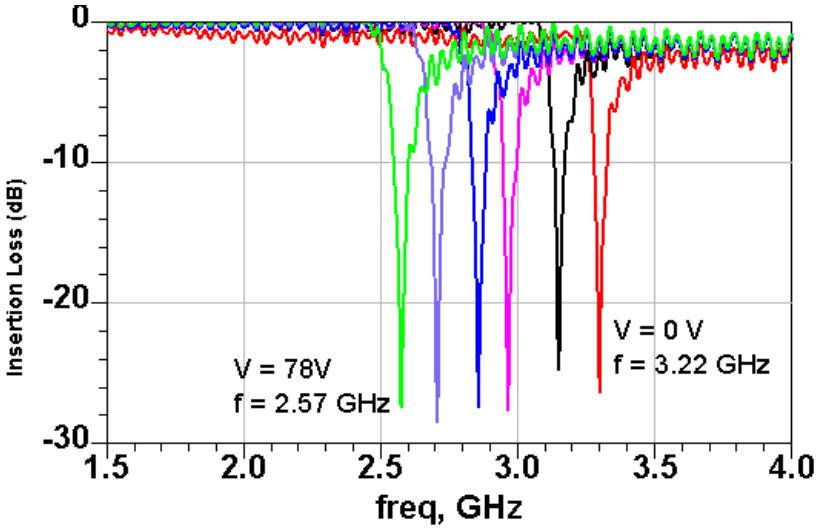

Figure 4.40 Measurement results of the tunable resonator 1 [20]

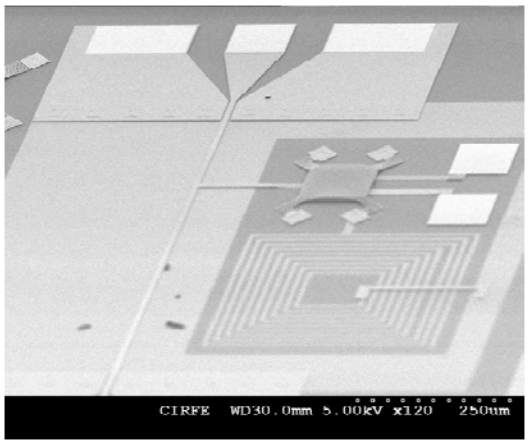

Figure 4.41 SEM picture of tunable resonator 2

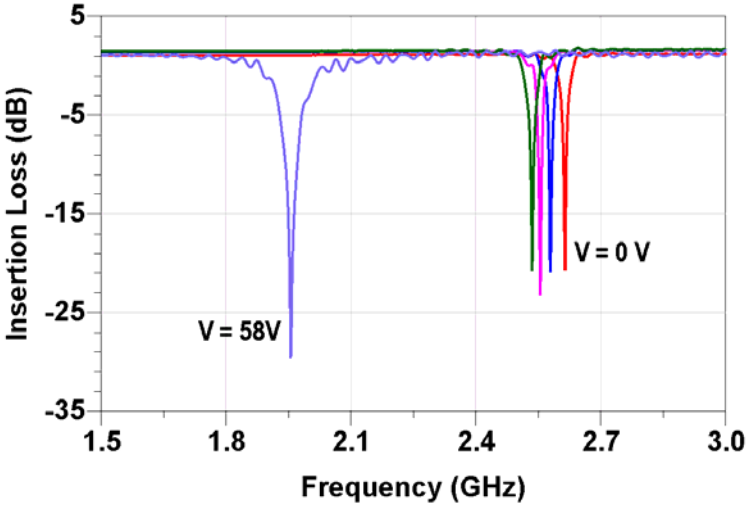

Figure 4.42 Measurement results of the tunable resonator 2

Superconducting tunable filters can be realized by employing the tunable resonators discussed earlier. The topology of the filter has a great impact on its tunability range. If varactors are the only tunable elements in the filter, it is more practical to design a tunable band-stop filter with all shunt resonators, because the size of the capacitors would be small and almost in the same range for all the resonators (unless the bandwidth is really high). This means a good tunability range could be achieved although the bandwidth of the filter changes as it gets tuned to other

frequencies. The other limitation comes from the inverters that provide the 90° phase shift between the resonators like the transmission lines or all-pass filters as shown earlier. These phase shifts provided by these inverters changes with frequency.

A tunable 3-pole BSF that uses the second type of varactors as the tunable elements was realized. The SEM picture shown in Figure 4.41 is the first resonator of this filter. The filter has the same topology of the one shown in Figure 4.30. The picture of this tunable filter is shown in Figure 4.43.

It is shown by EM simulation that the filter topology allows for a 20% tuning before the return loss outside the stop band reaches -16dB. The simulated results are shown in Figures 4.44 and 4.45. As expected the bandwidth becomes wider at lower frequencies and narrower at higher frequencies.

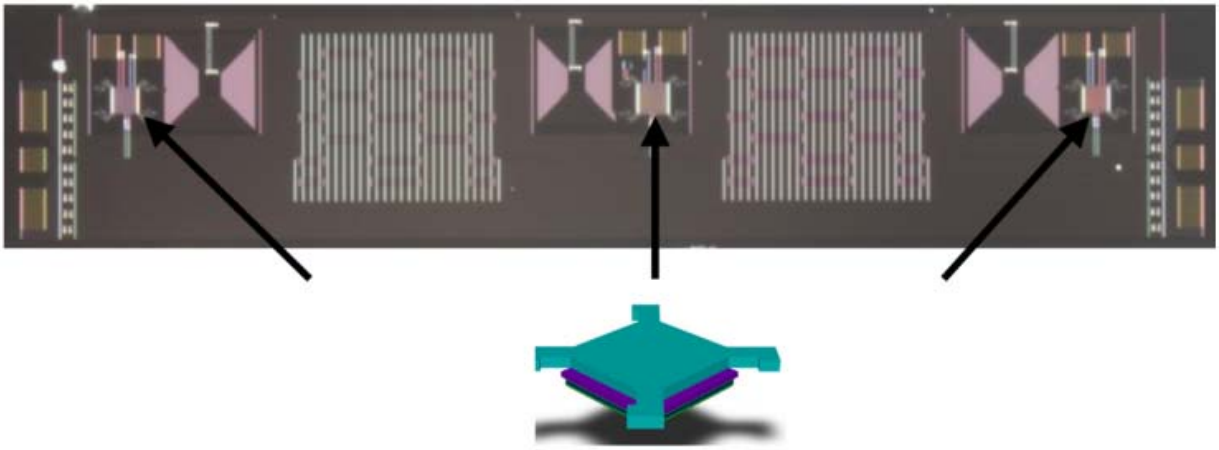

Figure 4.43 picture of the 3-pole tunable BSF

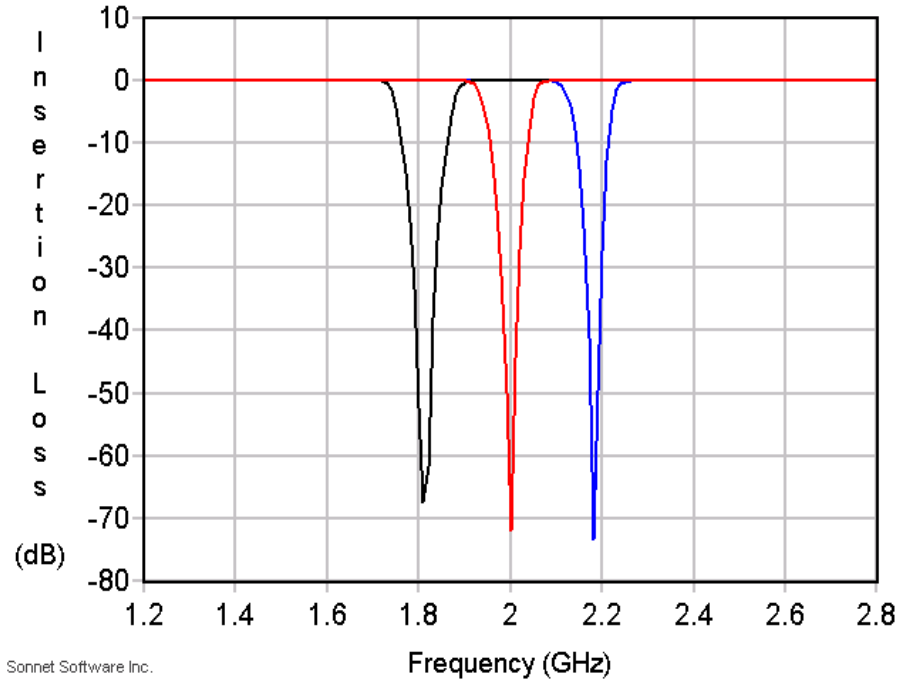

Figure 4.44 Simulated results of the tunable filter.

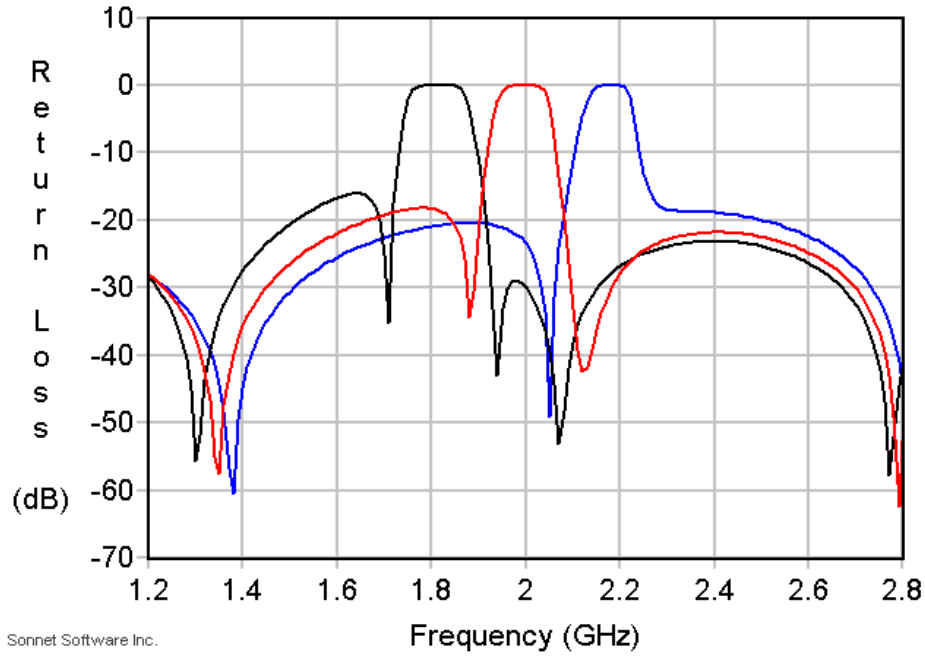

Figure 4.45 Simulated return loss of the tunable BSF

4.8 All-pass filters

All-pass filters allow perfect transmission at all frequencies and provide a 90° phase shift at the frequency they have been designed for. Therefore, an all-pass filter can play the role of an inverter and replace the long and spacious transmission line between the shunt resonators of a band-stop filter. A lumped element circuit model for an all-pass filter is shown in Figure 4.46.

In this model if L=C=1 and the characteristic impedance is normalized to 1Ω, the filter will have a 90° phase shift at ω=1rad/s.

Figure 4.46 Circuit model of the all-pass filters with phase of (a) 90° and (b) -90° at the centre frequency

Figure 4.47 shows the layout of an all-pass filter designed at 2GHz. The dimension of the filter is 0.3mm×0.5mm. The simulation results are shown in Figures 4.48 and 4.49. Figure 4.50 compares the phase of the designed all-pass filter with the phase of a 90° transmission line. It is noted that the rate of change in the phase of the all-pass filter is much less than a λ/4 transmission line. Consequently they can be used in the design of highly miniaturized BSF for wideband applications.

The dimensions of the designed all-pass filter at 2GHz are 0.3mm×0.5mm.

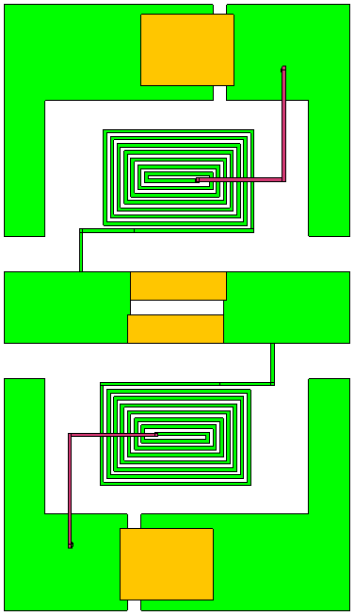

Figure 4.47 Layout of an all-pass filter at 2GHz

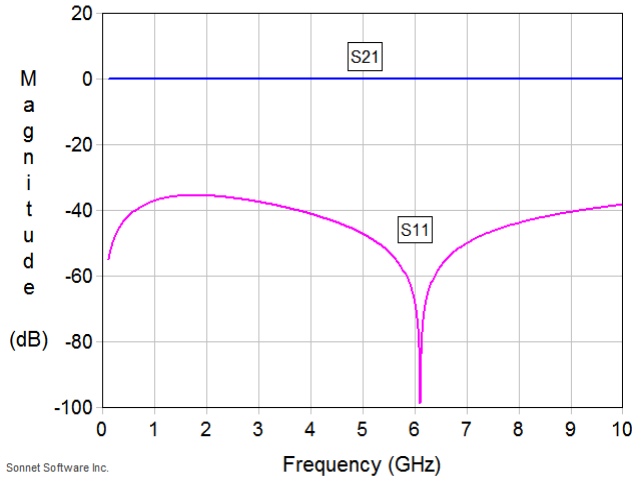

Figure 4.48 EM simulation results of an all-pass filter at 2GHz

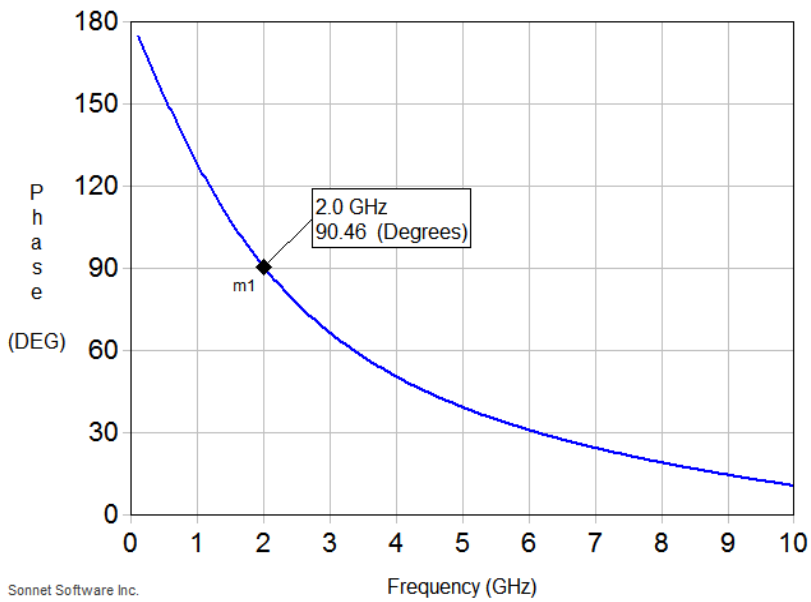

Figure 4.49 Phase response of an all-pass filter at 2GHz

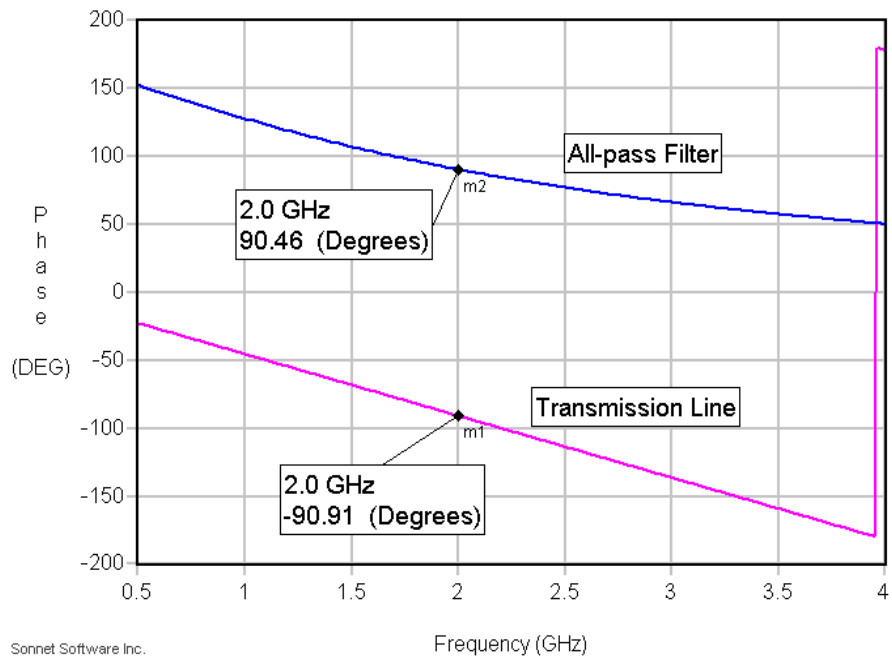

Figure 4.50 Comparison between phase response of the all-pass filter and a 90° transmission line

CHAPTER 5

5 Conclusion

In the first part of this work, a highly miniaturized UHF superconducting lumped element 7-pole band-pass filter with a relative bandwidth of 80% was designed, fabricated and measured. The filter design makes use of the thin dielectric layers and the small feature sizes of the standard niobium process offered by HYPRES to create a highly miniaturized filter. This filter design can thus be integrated with digital receivers realized with Superconducting Microelectronics (SME) technology on a single chip. The filter topology is that of the band-pass transformed low-pass prototype filter with alternating shunt and series lumped element resonators. This lumped element topology allows for the design of very wide band filters by eliminating the need to use frequency-dependent impedance inverters which typically limit the filter bandwidth to narrowband operation. The 7-pole filter has a centre frequency of 375 MHz, a bandwidth of 300MHz and a total size of 3mmx1mm. Each resonator has dimension of 0.5mmx1mm which is about 800 times smaller than the free space wavelength at the filter's centre frequency. Due to

the resonators being realized in lumped element form, the filter has a wide spurious free stop band of up to 4GHz. The measured return loss is better than 17 dB across the pass band without any post-fabrication tuning. It was shown that the size of the filter can further be reduced to half by using double layered spiral inductors. A 3-pole highly miniaturized low-pass filter was designed and tested employing the double layer inductor. The low-pass filter has a dimension of 549μm×123μm.

In the second part of this research, various configurations for lumped element Band-Stop Filters (BSF) were designed and tested. In order to eliminate the use of any inverters in the design, a band-stop transformed low-pass prototype filter with alternating shunt and series lumped element resonators was employed. The problem with this design was the wide spread of component values in adjacent resonators especially for narrowband designs. To solve this problem, the resonators were redesigned to have three elements instead of two in a way that the values for the new resonator were all in realizable ranges. A 3-pole BSF at 2GHz with a relative bandwidth of 1% was designed and simulated using this method. The values of the large components in each resonator could be reduced by a factor of 100. The total dimension of the filter is 1.25mm×0.5mm, while a 90° CPW transmission line designed with the same process would have a dimension of 17mm×0.5mm.

A band-stop filter at 2GHz with a bandwidth of 5% was also designed with this method, fabricated and tested. Another two band-stop filters were designed at 1GHz with a bandwidth of 10%. Since the values for wider bandwidths are realizable, the conventional resonator design was applicable. The measured results of all the three band-stop filters showed a broad match in the pass band of the filters; however, there were some discrepancies between the simulation and

measurement in their stop band. It was shown that the source of this discrepancy was the effect of kinetic inductance that was not considered in the simulations.

In order to achieve tunability, a superconducting MEMS varactor was integrated with a shunt band-stop resonator [20]. A measured tunability of more than 25% was achieved by applying different voltages to the varactor.

In order to be able to investigate the tunability of a band-stop filter, a 3-pole BSF with all shunt lumped element resonators. MEMS varactors were integrated with all the resonators. The 90° phase shift between the resonators was achieved using a 50Ω meandered Microstrip transmission lines. The simulation of the tunable filter shows a return loss of 20dB over a tuning range of 20%.

Appendix A

The peak value of a resonator's group delay is not at its centre frequency

Here, it is shown by both theory and simulation that for a single resonator, the value of the group delay is not at its maximum at the resonator's centre frequency.

For the resonator shown in the figure below, GD can be calculated as the following:

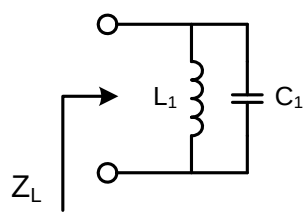

Figure A. 1 A simple shunt resonator

$$\Gamma = \frac{Z_L - Z_0}{Z_L + Z_0}$$

$$Z_L = j\omega L || \frac{1}{j\omega C} = \frac{j\omega L}{1 - LC\omega^2}$$

$$\Gamma = \frac{j\omega L - Z_0(1 - LC\omega^2)}{j\omega L + Z_0(1 - LC\omega^2)}$$

$$\varphi = \angle\Gamma = -2\tan^{-1}\left(\frac{\omega L}{Z_0(1 - LC\omega^2)}\right)$$

$$GD = -\frac{\partial\varphi}{\partial\omega} = \frac{2LZ_0(1 + LC\omega^2)}{L^2\omega^2 + {Z_0}^2(1 - LC\omega^2)^2}$$

The value of the group delay at the centre frequency can be calculated from the above formula:

$$GD = -\frac{\partial \varphi}{\partial \omega} = \frac{4Z_0}{L\omega^2} = 4CZ_0$$

Ness, in his paper, has also calculated the group delay of a single resonator at its centre frequency and has derived the same expression. He claims though, that this value of the peak of the group delay curve versus the frequency which is not correct. To prove this, it is shown that the derivative of GD at the centre frequency is not zero.

$$\frac{\partial GD}{\partial \omega}$$

$$= \frac{4L^2 C\omega Z_0\left(L^2\omega^2 + {Z_0}^2(1 - LC\omega^2)^2\right) - \left(2L^2\omega - 4\omega LC{Z_0}^2(1 - LC\omega^2)\right)\left(2LZ_0(1 + LC\omega^2)\right)}{\left(L^2\omega^2 + {Z_0}^2(1 - LC\omega^2)^2\right)^2}$$

Replacing ω with ω_0 gives the slope of the GD curve at the centre frequency which is not zero:

$$\frac{\partial GD}{\partial \omega}(\omega = \omega_0) = -\frac{4CZ_0}{\omega}$$

To check the validity of the above formula, simulation on an ideal lumped element resonator has been done in ADS. The GD and also the derivative of the GD versus the frequency are plotted.

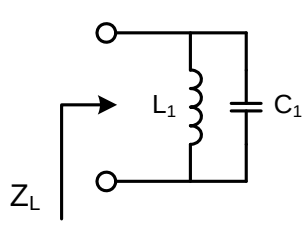

L1=20.3121 nH, C1=8.8679 pF

A simple calculation shows that the above resonator will resonate at 375MHz. Substituting the C value in the above equation, the slope of the GD curve at the resonator's centre frequency is calculated to be -4.73×10^{-18}.

The GD of the resonator generated by ADS circuit simulator is shown in Figure A.2.

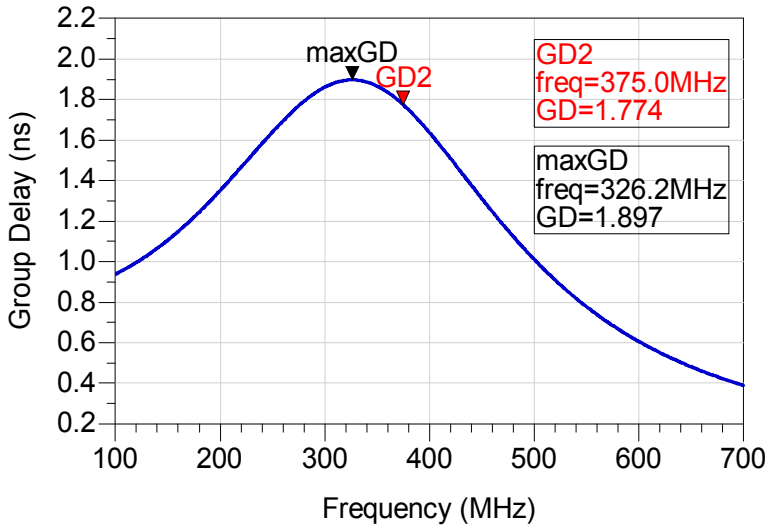

Figure A. 2 The group delay of shunt LC resonator showing the peak and centre frequencies.

It is noted that if the resonator is narrowband, the frequency of the group delay's peak value is extremely close to the resonance frequency, thus the Ness theory works perfectly for such applications. However, for the case of the wideband resonators and filters, the frequency of the group delay curve's peak value starts to drift apart from the resonance frequency. This is demonstrated in the Figure A.3 by comparing the group delay of two resonators with the same resonance frequency but different bandwidths. Column (a) shows the simulation results for the first resonator of a 7-pole BPF at 1GHz with a percentage bandwidth of 50%, while in (b) the simulation results is of the first resonator of a 7-pole filter at the same frequency but a percentage bandwidth of 5% is demonstrated.

The first resonator of a 7-pole BPF at 1GHz with **50%** BW:

L = 4.7607 nH

C = 5.3208 pF

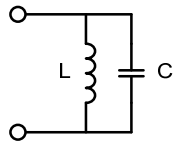

The first resonator of a 7-pole BPF at 1GHz with **5%** BW:

L = 0.4761 nH

C = 53.2076 pF

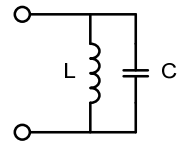

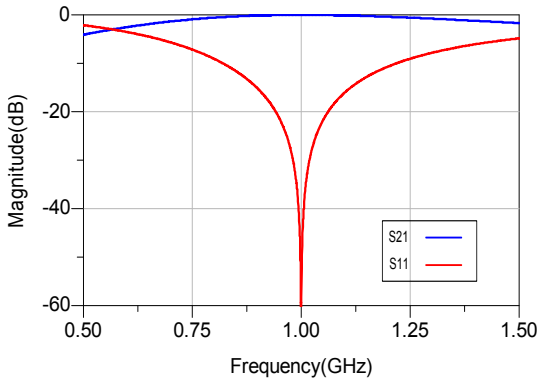

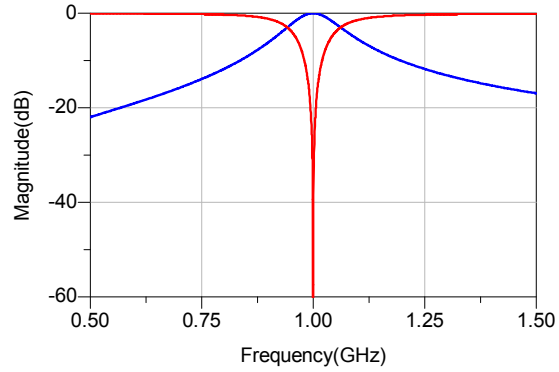

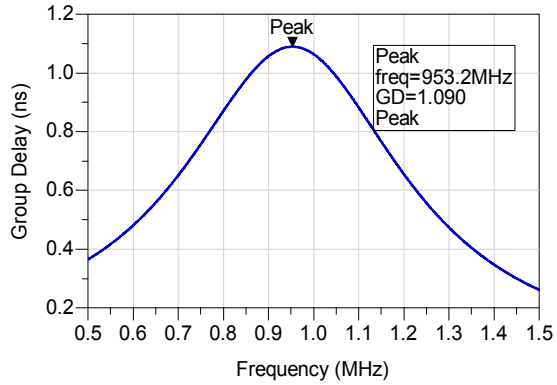

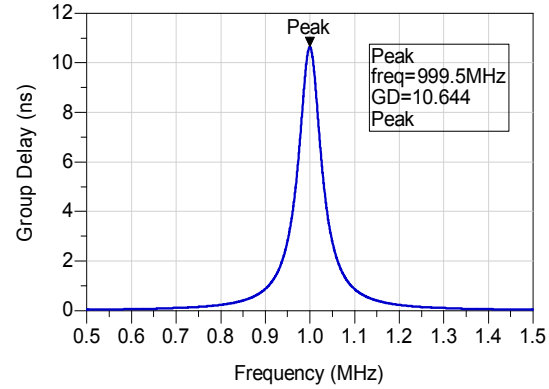

The marker shows the frequency of the peak

The marker shows the frequency of the peak

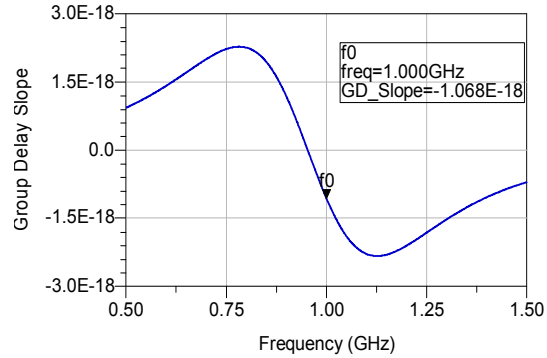

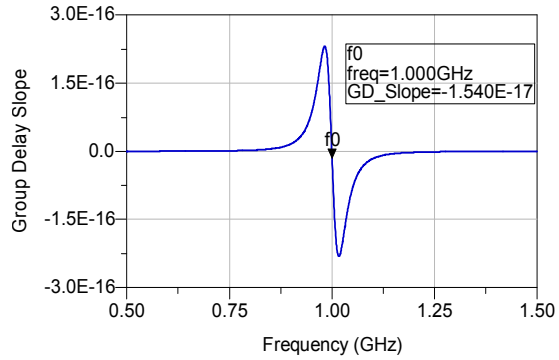

The marker shows the group delay slope at the centre frequency of the filter.

The marker shows the group delay slope at the centre frequency of the filter.

Figure A. 3 Comparison between the S-parameters and group delay curves of narrowband and wideband shunt resonators.

In Figure A.4 the S-parameter and group delay curve of a 7-pole band-pass filter's first resonator at 1GHz is plotted for different bandwidths. The marker on the group delay curve is showing the frequency when the peak value of the group delay happens. It can be seen that for bandwidths less than 10%, the peak frequency is close enough to the centre frequency of the filter, thus the Ness method works perfectly.

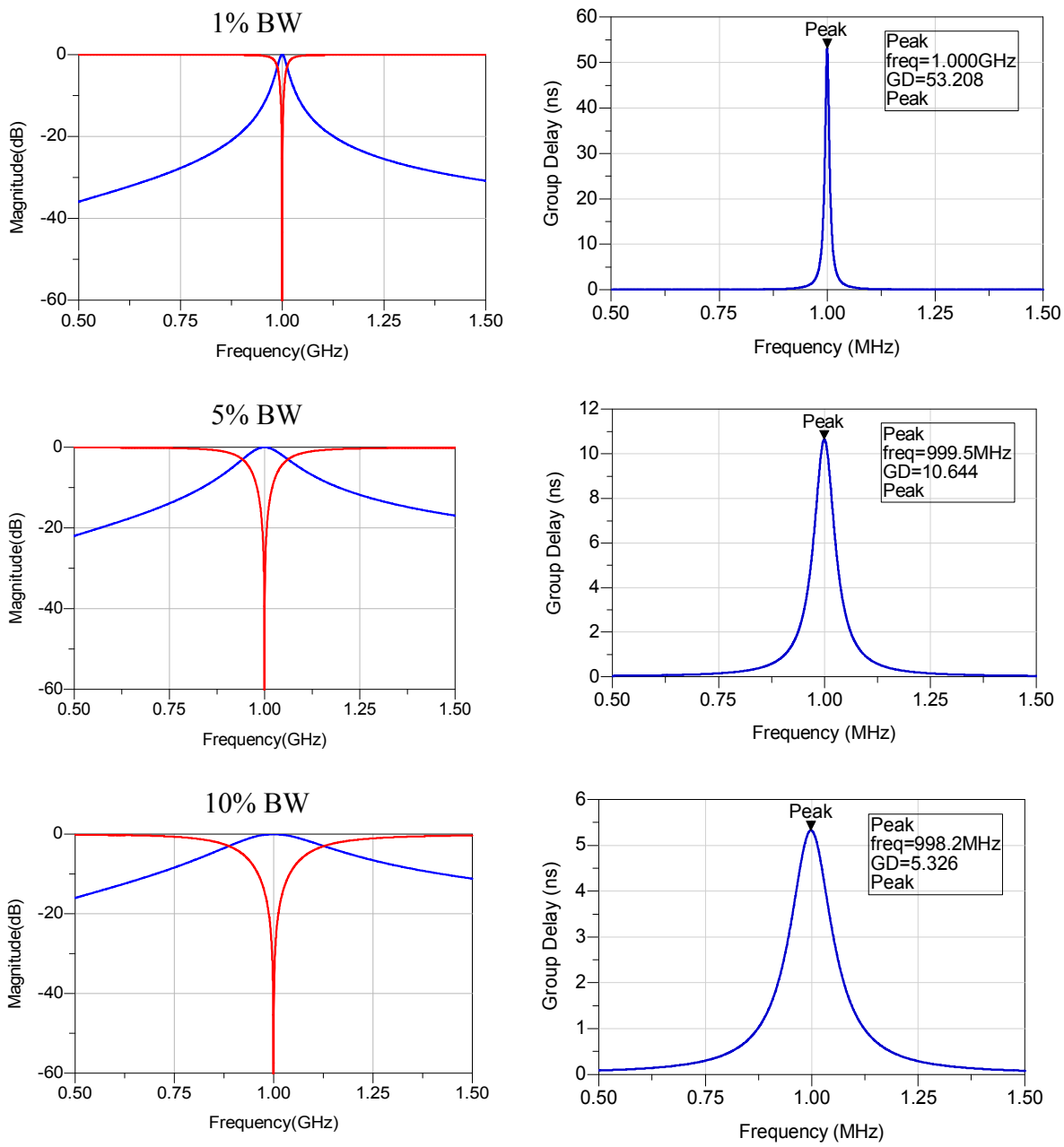

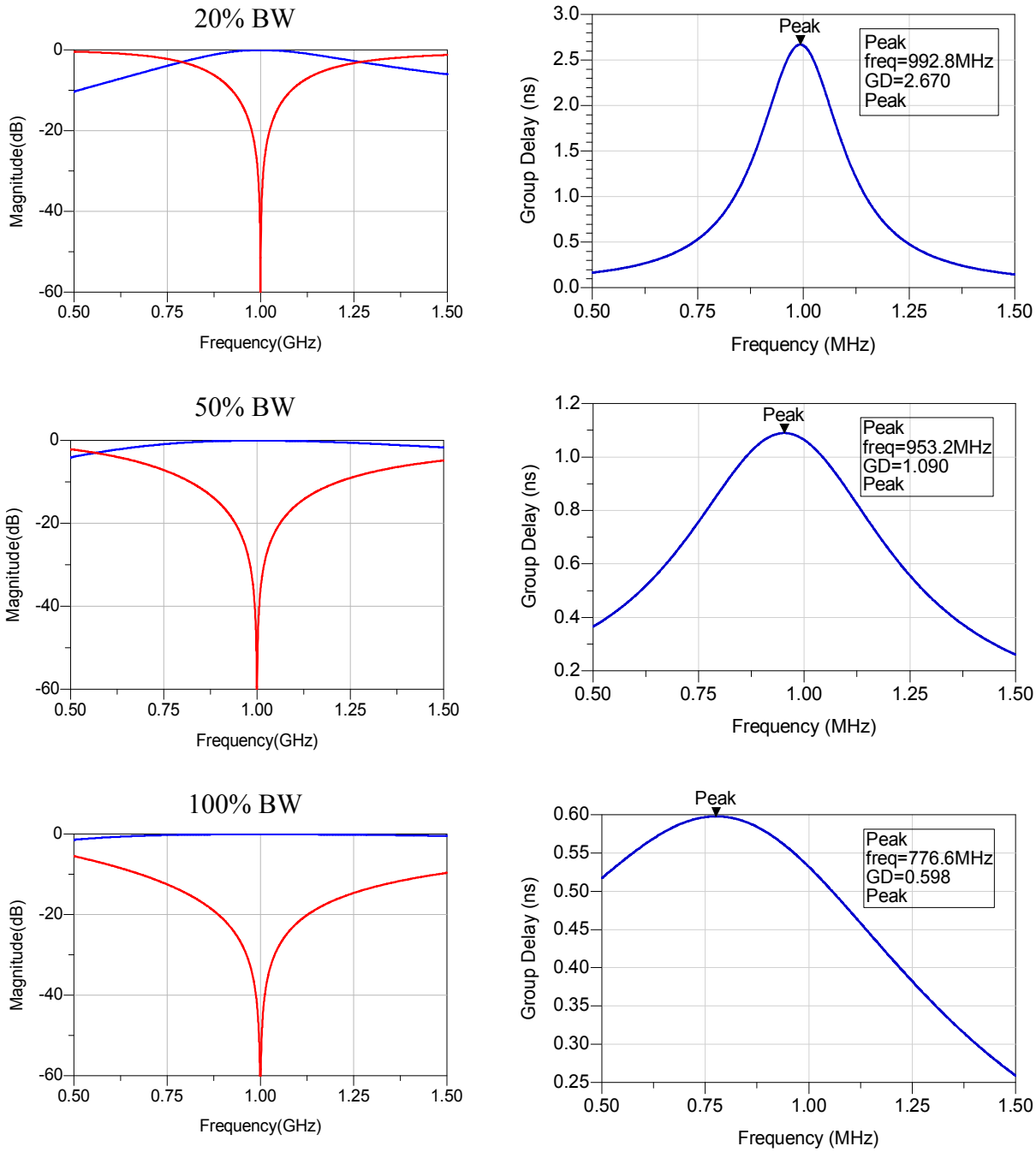

Figure A. 4 Comparison between the S-parameters and group delay curves of shunt resonators with percentage bandwidths of 1%, 5%, 10%, 20%, 50% and 100% respectively.

References

[1] www.HYPRES.com.

[2] Laforge, P.D.; Mansour, R.R.; Ming Yu; , "Highly Miniaturized Multilayer Superconducting Filter," Microwave Symposium Digest, 2006. IEEE MTT-S International , vol., no., pp.685-688, 11-16 June 2006.

[3] Weinstock, H.; Nisenoff, Martin, Microwave Superconductivity, Proceedings of the NATO Advanced Study Institute, Millau, France, 29 August -10 September, 1999, Series: NATO Science Series E: , Vol. 375, Springer (2002).

[4] Lancaster, M.J.; Huang, F.; Porch, A.; Avenhaus, B.; Jia-Sheng Hong; Hung, D.; , "Miniature superconducting filters," Microwave Theory and Techniques, IEEE Transactions on , vol.44, no.7, pp.1339-1346, Jul 1996.

[5] Hammond, R.B.; Hey-Shipton, G.L.; Matthaei, G.L.; , "Designing with superconductors," Spectrum, IEEE , vol.30, no.4, pp.34-39, Apr 1993.

[6] Swanson D. G., Forse R. and Nilsson B. J. L., “A 10GHz lumped element high temperature superconductor filter”, IEEE MTT-S Digest, pp.1191-3, 1990.

[7] Ye S. and Mansour R. R., “Design of manifold-coupled multiplexers using superconductive lumped element filters”, IEEE MTT-S Int. Symp. Digest, pp. 191-4, 1994.

[8] J. Zhou, M. J. Lancaster, and F. Huang, "Superconducting microstrip filters using compact resonators with double-spiral inductors and interdigital capacitors", IEEE MTT Symp. Dig., pp. 1889 - 1892, 2003.

[9] Ness, J.B.; , "A unified approach to the design, measurement, and tuning of coupled-resonator filters," Microwave Theory and Techniques, IEEE Transactions on , vol.46, no.4, pp.343-351, Apr 1998.

[10] http://www.home.agilent.com.

[11] http://www.sonnetsoftware.com.

[12] D. M. Pozar; Microwave Engineering, 3rd Edition; Wiley; 2005.

[13] Bandler, J.W.; Biernacki, R.M.; Shao Hua Chen; Grobelny, P.A.; Hemmers, R.H.; , "Space

mapping technique for electromagnetic optimization," Microwave Theory and Techniques, IEEE Transactions on , vol.42, no.12, pp.2536-2544, Dec 1994.

[14] Shen Ye; Mansour, R.R.; , "An innovative CAD technique for microstrip filter design," Microwave Theory and Techniques, IEEE Transactions on , vol.45, no.5, pp.780-786, May 1997.

[15] R. J. Cameron, C. Kudsia, and R. Mansour, “Microwave Filters for Communication Systems”, John Wiley & Sons, 2007.

[16] M. R. Rafique, T. Ohki, B. Banik, H. Engseth, P. Linner´, and A. Herr, “Miniaturized superconducting microwave filters,” Superconduct. Sci. Technol., vol. 21, no. 7, p. , Jul. 2008.

[17] I. Hunter, Theory and Design of Microwave Filters. London, U.K.: IEE Press, 2001.

[18] Guoyong Zhang; Lancaster, M.J.; Huang, F.; Roddis, N.; , "A superconducting microstrip bandstop filter for an L-band radio telescope receiver," Microwave Conference, 2005 European , vol.1, no., pp. 4 pp., 4-6 Oct. 2005.

[19] P. D. Laforge, R. R. Mansour, and M. Yu, “The design of miniaturized superconducting filters with the reflected group delay method,” IEEE Trans. Applied Superconductivity, vol. 20, no. 4, pp. 2265–2271, Aug. 2010.

[20] Attar, S.S.; Setoodeh, S.; Mansour, R.R.; , "Low temperature superconductive tunable bandstop resonator and filter," Microwave Symposium Digest (MTT), 2010 IEEE MTT-S International , vol., no., pp.1-1, 23-28 May 2010.

[21] J. Rosa et al., "SATCOM-on the-Move (SOTM) using Superconductor Microelectronics a quantum leap in performance", 2004 IEEE/Sarnoff Symposium on Advances in Wired and Wireless Communication, pp. 95-98, 2004.

[22] Hypres Niobium Integrated Circuit Fabrication Process-Design Rules Hypres Inc., New York, Jun. 2005 [Online]. Available: http://www.hypres.com/pages/download/designrules/rules.pdf.

[23] Mansour, R.R.; , "Microwave superconductivity," Microwave Theory and Techniques, IEEE Transactions on , vol.50, no.3, pp.750-759, Mar 2002.